

Universidade do Minho  
Escola de Engenharia

Diogo Lourenço Fernandes

**New generation of structural reinforcement  
systems for concrete structures**

Julho de 2022



Universidade do Minho  
Escola de Engenharia

Diogo Lourenço Fernandes

**New generation of structural reinforcement  
systems for concrete structures**

Dissertação de Mestrado  
Mestrado Integrado em Engenharia Civil

Trabalho efetuado sob a orientação do  
**Professor Joaquim António Oliveira de Barros**  
**Doutor Fábio Pereira Figueiredo**

Julho de 2022

## DIREITOS DE AUTOR E CONDIÇÕES DE UTILIZAÇÃO DO TRABALHO POR TERCEIROS

Este é um trabalho académico que pode ser utilizado por terceiros desde que respeitadas as regras e boas práticas internacionalmente aceites, no que concerne aos direitos de autor e direitos conexos.

Assim, o presente trabalho pode ser utilizado nos termos previstos na licença abaixo indicada.

Caso o utilizador necessite de permissão para poder fazer um uso do trabalho em condições não previstas no licenciamento indicado, deverá contactar o autor, através do RepositóriUM da Universidade do Minho.

*Licença concedida aos utilizadores deste trabalho*



Atribuição-SemDerivações  
CC BY-ND

<https://creativecommons.org/licenses/by-nd/4.0/>

## Acknowledgement

This very important chapter of my Master's life is coming to an end, therefore I would like to thank all of those who have deeply contributed to the success of my academic journey.

First of all, I would like to thank my Professor, Joaquim António Oliveira de Barros for his invaluable guidance throughout my studies and endless support to provide me with the tools needed to choose the right direction and successfully complete my dissertation and leading to a personal growth and development that helped me set goals and reach my full potential.

I would also like to thank Dr. Fábio Pereira Figueiredo from whom I have received a great deal of support, assistance and guidance throughout the writing of this dissertation.

In addition, I would like to thank my loving parents for having given me this opportunity to pursue an academic career. I could have not completed this dissertation without their endless support. You have always been there for me.

A special thank you to my girlfriend who has been through this entire journey with me by giving me support and encouraging me to become a better person and achieve my goals.

Lastly, Thank you Grandma Augusta...

## STATEMENT OF INTEGRITY

I hereby declare having conducted this academic work with integrity. I confirm that I have not used plagiarism or any form of undue use of information or falsification of results along the process leading to its elaboration.

I further declare that I have fully acknowledged the Code of Ethical Conduct of the University of Minho.

# New generation of structural reinforcement systems for concrete structures

## Abstract

Civil engineering has an important role in our society, which is constantly demanding for innovative and sustainable products. It is the civil engineer duty to design efficient infrastructures capable of promoting the sustainability and durability of works of art. Over the last few years, studies in this sector have focused on the use of fibre reinforced polymer reinforcements, which was the subject of this work.

Corrosion of steel reinforcement is a well-known weakness that can compromise the safe use of reinforced concrete (RC) structures. This leads to the need for rehabilitation and reinforcement of the built heritage, whose costs are, in many cases, so high that demolition is the only option with the consequent harmful economic, social, and environmental impacts. The preparation and assembly of conventional reinforcement has a significant impact in final cost, and these tasks are always associated with accidents involving workers. Thus, the present thesis aims to combine recent developments in the area of fabrication of fibre reinforced polymer (FRP) with those in the area of fibre reinforced concrete (FRC), to develop an alternative reinforcing system for reinforced concrete.

In this dissertation, a 12m length single span beam for an office building with BCR (braided composite rods) of glass fibre strands, and SFRSCC (steel fibre reinforced self-compacting concrete) was studied. The evaluation of the behaviour of this structural system was performed based on the finite element method (FEM). In the first phase, three series of shallow beams failing in bending were tested to evaluate the potential of the numerical analysis on capturing the experimental results. The second phase focused on the conception of the numerical I beam model and subsequent analysis of the behaviour in bending. The main conclusions are presented.

**KEYWORDS:** Fibre reinforced concrete (FRC); BCR; Service limit state; Numerical modelling; Glass fibre reinforced polymer (GFRP).

# Nova geração de sistemas de reforço estrutural para estruturas de betão

## Resumo

A Engenharia civil tem atualmente um papel muito importante na nossa sociedade, a qual exige e necessita constantemente de produtos inovadores e sustentáveis. Cabe ao Engenheiro Civil dimensionar infraestruturas eficientes capazes de promover a sustentabilidade e durabilidade do ambiente construído. Ao longo dos últimos anos têm sido efetuados notáveis desenvolvimentos na utilização de materiais compósitos de matriz polimérica para o reforço de estruturas de betão, os quais serão tema neste trabalho.

A corrosão das armaduras de aço é uma das maiores causas de patologias observadas nas estruturas de betão armado. Tal facto leva à necessidade de intervenções de reabilitação e de reforço do património construído, cujo custos são, em muitos casos, tão elevados que conduzem à opção pela demolição, com os consequentes impactos económicos, sociais e ambientais. O tempo de preparação e montagem das armaduras convencionais a aplicar em elementos estruturais de edifícios tem peso significativo no custo final destes, e a estas tarefas estão sempre associados o maior número de acidentes ocorridos com trabalhadores. Assim, na presente tese são realizados estudos combinando os recentes desenvolvimentos na área do fabrico de polímeros reforçados com fibras (FRP) com os desenvolvimentos na área do betão reforçado com fibras (FRC), de forma a constituir um sistema de reforço alternativo às soluções tradicionais em betão armado.

Na presente dissertação, uma viga de secção I com vão de 12m, projetada para um edifício de escritórios, reforçada com varões compósitos entrelaçados (BCR) de fios de fibra de vidro (GFRP) e betão autocompactável reforçado com fibras de aço (SFRSCC) foi estudada. A avaliação do comportamento deste sistema estrutural realizou-se com recurso ao método dos elementos finitos. Numa primeira fase, três séries de lajes de baixa espessura sujeitas a flexão foram estudadas de forma a avaliar o potencial da simulação numérica em capturar resultados experimentais. Numa segunda fase procedeu-se à criação do modelo numérico da viga, a simulação do ensaio á flexão da viga e posterior análise. As principais conclusões são apresentadas.

**PALAVRAS-CHAVE:** Betão reforçado com fibras (FRC); BCR; Estado Limite de Serviço; Modelação numérica; Varões de fibra de vidro (GFRP).

## Table of Contents

<b>1. Introduction.....</b>	<b>1</b>
1.1. General .....	1
1.2. Motivation and objectives.....	2
1.3. Outline of the thesis.....	2
<b>2. State of the Art on High Performance Materials for Structural Systems .....</b>	<b>5</b>
2.1 Introduction.....	5
2.2. Fibre Reinforce Polymer (FRP) .....	6
2.3. Fibre Reinforced Concrete (FRC).....	7
2.4. Three-dimensional system reinforcement textile (3D-SRT).....	9
2.5. Bond behaviour between FRC and FRP bars .....	11
2.6. Relation between fibre orientation and post-cracking behaviour in FRC.....	13
2.6.1. Influence of steel fibres on Fracture Energy .....	18
2.7. Shear capacity of FRC beams. ....	20
<b>3. Bond Behaviour Between GFRP and SFRSCC.....</b>	<b>26</b>
3.1. Experimental Program .....	26
3.1.1. Materials Properties .....	26
3.1.2. Pullout bending test procedure.....	29
3.2. Test results and discussion.....	31
<b>4. Modelling the Bond Behaviour Between GFRP Bars and SFRSCC .....</b>	<b>35</b>
4.1. Local bond stress-slip relationship.....	35
4.1.1. Analytical study of bond-slip relationships determined from inverse analysis using the FBL software.....	37
4.1.2 Numerical simulation of the pullout bending tests and predictive performance of the proposed bond model .....	46



<b>5. Numerical Modelling of Shallow beams .....</b>	<b>53</b>
5.1. Experimental program .....	53
5.2. Numerical simulations using FEMIX-GID software .....	57
5.2.1. Influence of reinforcing shallow beams with GFRP and prestressed steel wires .....	65
<b>6. Case Study of I-shaped cross-sectional beams for buildings .....</b>	<b>70</b>
6.1. Numerical Simulations.....	70
6.2.1. Results and discussion .....	77
6.2.2. Influence of the GFRP-SFRSCC bond conditions on force-deflection response of I-shaped cross-sectional beams.....	86
<b>7. Summary and Conclusions.....</b>	<b>89</b>
<b>Bibliography.....</b>	<b>91</b>
<b>APPENDIX A .....</b>	<b>94</b>
<b>APPENDIX B .....</b>	<b>106</b>

## List of Figures

FIGURE 1 - DIFFERENCE BETWEEN PLAIN AND FIBRE REINFORCED CONCRETE, ACCORDING TO MC2010 [13].....	8
FIGURE 2 - STANDARD HORIZONTAL BRAIDING MACHINE DEVELOPED BY THE FIBROUS MATERIALS RESEARCH GROUP, AT UNIVERSITY OF MINHO [17].....	10
FIGURE 3 - SAMPLES OF 3D-SRT REINFORCEMENT FOR SLABS [17].....	11
FIGURE 4 - PULLOUT BENDING TEST [8]. .....	12
FIGURE 5 – FORCE–CRACK OPENING WIDTH RELATIONSHIP OBTAINED FROM SPLITTING TENSILE TESTE FOR: (A) $\Theta = 0^\circ$ AND (B) $\Theta = 90^\circ$ [22].....	14
FIGURE 6 – NOMINAL TENSILE STRESS–CRACK OPENING WIDTH RELATIONSHIP, $\Sigma-w$ , OBTAINED FROM SPLITTING TENSILE TEST FOR: (A) $\theta = 0^\circ$ AND (B) $\theta = 90^\circ$ [22].....	14
FIGURE 7 – FORCE–AVERAGE CRACK WIDTH RELATIONSHIP, $F-w$ , OBTAINED FROM UNIAXIAL TENSILE TESTS FOR: (A) $\theta = 0^\circ$ AND (B) $\theta = 90^\circ$ [22].....	15
FIGURE 8 – CROSS SECTIONS OF AN EXEMPLARY BEAM: (A) IMAGE AFTER VOI SELECTION AND (B) AFTER STEEL FIBRES SEGMENTATION [24]. .....	16
FIGURE 9 – IMAGE PROCESSING STEPS: (A) CONVERTING A COLOURED IMAGE TO GREYSCALE, (B) ADJUSTING A THRESHOLD, (C) DEFINING MASK, NOISE AND WATERSHED FUNCTIONS, (D) FITTING THE BEST ELLIPSE TO EACH FIBRE [22]. .....	16
FIGURE 10 - “AVERAGE” FORCE-DISPLACEMENT RELATIONSHIP FOR SERIES OF 30, 60 E 90 KG/M <sup>3</sup> OF FIBRES [14]. .	19
FIGURE 11 - TEST SET-UP REQUIRED BY EN 14651 (DIMENSIONS IN MM). .....	20
FIGURE 12 - DEFINITION OF CROSS-SECTIONAL PARAMETERS, INTERNAL LOADS AND STRAIN PROFILE ACCORDING TO MC2010 [13]. .....	24
FIGURE 13 – SFRSCC SLUMP FLOW TEST. .....	27
FIGURE 14 - EXAMPLE OF TENSILE TEST ON GFRP BAR [28]. .....	28
FIGURE 15 – SPECIMEN’S PRODUCTION: A) MOULD, B) APPEARANCE OF SPECIMENS AFTER CAST.....	29
FIGURE 16 – DETAIL OF THE SPECIMEN BEFORE PULLOUT TEST.....	30
FIGURE 17 – PULLOUT BENDING TEST SETUP DETAILS.....	31
FIGURE 18 – RELATIONSHIPS BETWEEN THE APPLIED PULLOUT FORCE AND SLIP AT: A) LOADED END, B) FREE END....	33
FIGURE 19 – DETAIL OF THE SPECIMENS AFTER THE PULLOUT TEST: A) C15LB90, B) C25LB140. ....	34
FIGURE 20 – GENERAL BOND-SLIP LAW.....	36
FIGURE 21 – ILLUSTRATION OF THE INFLUENCE OF THE VALUE OF PARAMETERS $\alpha$ AND $\beta$ (REPRESENTED AS $\alpha 1$ AND $\alpha 2$ , RESPECTIVELY) IN THE SHAPE OF THE BOND-SLIP RELATIONSHIP: A) PRE-PEAK PHASE, B) POST-PEAK PHASE. ....	37

FIGURE 22 – DIFFERENT LOCAL BOND-LAWS: A) TRANSFORMATION FROM NLML102 TO NLML101, B) NLML102.	38
FIGURE 23 – FBL INTERFACE FOR THE ANALYSIS OF C15LB90 SERIES.....	41
FIGURE 24 – DATA OF THE MAIN PARAMETERS USED IN THE INVERSE ANALYSIS FOR C15LB90 SERIES: A) DATA FILE, B) FBL INTERFACE.....	42
FIGURE 25 – INTRODUCTION OF THE EXPERIMENTAL RESULTS OF $F - \delta$ IN THE INVERSE ANALYSIS FOR C15LB90 SERIES.....	42
FIGURE 26 – CALIBRATION BETWEEN THEORETICAL AND EXPERIMENTAL $F - \delta$ CURVES FOR C15LB90 SERIES IN FBL.....	43
FIGURE 27 – LOCAL BOND LAW FOR C15LB90 SERIES DETERMINED BY INVERSE ANALYSIS.....	43
FIGURE 28 – CALIBRATION BETWEEN THEORETICAL AND EXPERIMENTAL $F - \delta$ CURVES FOR SERIES: A) C15LB90, B) C25LB90, c) C15LB140, d) C25LB140, e) C15LB200, f) C25LB200.....	44
FIGURE 29 – LOCAL BOND LAW FOR SERIES: A) C15LB90, B) C25LB90, c) C15LB140, d) C25LB140, e) C15LB200, f) C25LB200.....	45
FIGURE 30 – TYPES OF FINITE ELEMENTS USED IN THE FEM MODEL: A) LAGRANGIAN 4-NODE ELEMENTS, B) LINEAR 2-NODE ELEMENTS, c) LINEAR 4-NODE ELEMENTS [8]. .....	47
FIGURE 31 – TRILINEAR STRESS-STRAIN DIAGRAM TO SIMULATE THE FRACTURE MODE I CRACK PROPAGATION [34]. ...	48
FIGURE 32 – LINEAR MATERIAL BEHAVIOUR OF GFRP BARS. ....	49
FIGURE 33 – FINITE ELEMENT MODEL ASSEMBLED TO SIMULATE PULLOUT BENDING TESTS.....	50
FIGURE 34 – BOND-SLIP RELATIONSHIPS CALIBRATED USING FEMIX FOR SERIES: A) C15LB90, B) C25LB90, c) C15LB140, d) C25LB140, e) C15LB200, f) C25LB200.....	51
FIGURE 35 – GEOMETRY, SUPPORT AND LOAD CONDITIONS OF THE TESTED SHALLOW BEAMS INCLUDING THE MONITORING SYSTEM [35]. .....	54
FIGURE 36 – AVERAGE FORCE <i>VERSUS</i> SLIP AT MIDSPAN OF SERIES: (A) A_6, (B) B_8, (C) C_10 [35]. .....	56
FIGURE 37 – GEOMETRY OF THE BEAM USED FOR THE SIMULATION OF THE A_6_0 SERIES.....	58
FIGURE 38 – SERENDIPITY 8-NODE FINITE ELEMENT [8]. .....	59
FIGURE 39 – FINITE ELEMENT MESH USED FOR THE SIMULATION OF A_6_0 SERIES (DIMENSIONS IN MM). .....	59
FIGURE 40 – SUPPORTS OF THE SHALLOW BEAMS.....	60
FIGURE 41 – LOADS OR PRESCRIBED DISPLACEMENTS. ....	60
FIGURE 42 – TENSILE-SOFTENING DIAGRAMS USED IN GID: (A) TRILINEAR, (B) QUADRILINEAR.....	61
FIGURE 43 – STEEL PROPERTIES USED IN THE SIMULATION OF THE A_6_0 SLAB STRIP SERIES.....	63

FIGURE 44 – LOAD <i>v/s.</i> DEFLECTION AT MID-SPAN OBTAINED EXPERIMENTALLY AND NUMERICALLY (ASSUMING PERFECT BOND) FOR THE SHALLOW BEAMS SERIES: (A) A_6_0, (B) B_8_0, (C) B_8_45, (D) C_10_0, (E) C_10_45. ....	64
FIGURE 45 – GID GRAPHIC VISUALIZATION OF THE ASSIGNED MATERIALS CONSTITUTIVE MODELS IN THE B_8_45_Post TENSIONING BEAM. ....	67
FIGURE 46 – GID GRAPHIC VISUALIZATION OF THE ASSIGNED MATERIALS CONSTITUTIVE MODELS IN THE C_10_45_Post TENSIONING BEAM. ....	67
FIGURE 47 – CROSS SECTION OF THE NUMERICALLY SIMULATED BEAMS: (A) B_8_45_Post TENSIONING, (B) C_10_45_Post TENSIONING. ....	67
FIGURE 48 – LOAD <i>v/s.</i> DEFLECTION AT MID-SPAN OBTAINED NUMERICALLY (ASSUMING PERFECT BOND) FOR THE BEAMS: (A) B_8_45_Post TENSIONING, (B) C_10_45_Post TENSIONING. ....	68
FIGURE 49 – COMPARISON BETWEEN FORCE DEFLECTION RESPONSE OF THE DEVELOPED NUMERICAL SIMULATIONS...	68
FIGURE 50 – PROPOSED I BEAM AND APPLICATIONS: (A) GEOMETRY OF THE BEAM, (B) EXAMPLE 1, (C) EXAMPLE 2, (D) EXAMPLE 3. ....	71
FIGURE 51 – HYPOTHETICAL CASE STUDY: (A) STRUCTURAL APPLICATION OF THE BEAM, (B) SECTION A-A'. ....	72
FIGURE 52 – UNIFORMLY DISTRIBUTED LOADS AND $\Psi$ FACTORS FOR OFFICE BUILDINGS, RESPECTIVELY, ACCORDING TO: (A) EUROCODE 1, (B) EUROCODE 0. ....	73
FIGURE 53 – NUMERICALLY SIMULATED BEAMS: (A) A_10 $\phi$ 20, (B) B1_6 $\phi$ 12_ $\phi$ 15, (C) B2_4 $\phi$ 12_ $\phi$ 15, (D) B3_5 $\phi$ 12_3 $\phi$ 10, (E) C_6 $\phi$ 12. ....	75
FIGURE 54 – GEOMETRICAL DETAILS OF THE HYBRID SFRSCC BEAM REINFORCED BY PRESTRESSED STEEL STRAND AND GFRP BARS (DIMENSIONS IN MM). ....	76
FIGURE 55 – FORCE-DEFLECTION RESPONSE OF THE DEVELOPED NUMERICAL SIMULATIONS AND DEFLECTION LIMITATION FOR SERVICEABILITY LIMIT STATES. ....	78
FIGURE 56 – DEFLECTION VISUALIZATION OF THE NUMERICALLY SIMULATED BEAMS: (A) A_10 $\phi$ 20, (B) B1_6 $\phi$ 12_ $\phi$ 15 (DISPLACEMENTS IN MM). ....	80
FIGURE 57 – CONCRETE STRESSES VISUALIZATION OF THE NUMERICALLY SIMULATED BEAMS: (A) A_10 $\phi$ 20, (B) B1_6 $\phi$ 12_ $\phi$ 15. ....	83
FIGURE 58 – EUROCODE 2, PART 1-1 DESIGN RECOMMENDATIONS: (A) EXPOSURE CLASSES, (B) RECOMMENDED VALUES OF <i>wlim</i> FOR THE EXPOSURE CLASSES. ....	84
FIGURE 59 – CRACK PATTERN VISUALIZATION OF THE NUMERICALLY SIMULATED BEAMS: (A) A_10 $\phi$ 20, (B) B1_6 $\phi$ 12_ $\phi$ 15. ....	85

FIGURE 60 – GEOMETRICAL DETAILS OF THE SFRSCC BEAM REINFORCED WITH PASSIVE GFRP BARS (DIMENSIONS IN MM). .....	86
FIGURE 61 – LOAD <i>VERSUS</i> MID-SPAN DEFLECTION ASSUMING BOND SLIP AND PERFECT BOND BETWEEN GFRP BARS AND SURROUNDING SFRSCC. ....	87
FIGURE 62 – CREATION OF POINTS, LINES, AND SURFACES FOR A_6_0 SERIES BY USING POINTS.....	94
FIGURE 63 – CREATION AND ASSOCIATION OF LAYERS TO THE MATERIALS. ....	95
FIGURE 64 – SERENDIPITY 8-NODE FINITE ELEMENT [8]. ....	95
FIGURE 65 – FINITE ELEMENT NUMBER OF INTEGRATION POINTS SELECTION. ....	96
FIGURE 66 – ATTRIBUTION OF THE NUMBER OF CELLS AND CORRESPONDING SIZE TO DEFINE THE FINITE ELEMENTS. .	96
FIGURE 67 – CREATION OF THE FINITE ELEMENT MESH: (A) GENERATE THE MESH, (B) COLLAPSE THE NODES OF THE MESH. ....	97
FIGURE 68 – FINITE ELEMENT MESH USED FOR THE SIMULATION OF A_6_0 SERIES (DIMENSIONS IN MM). ....	98
FIGURE 69 – CALCULATION SOFTWARE USED ALONG WITH GID. ....	98
FIGURE 70 – INTRODUCTION OF THE MESH ELEMENT PROPERTIES: (A) COMMAND, (B) IMPUTED ELEMENT PROPERTIES. ....	99
FIGURE 71 – GID GRAPHIC VISUALIZATION OF THE ELEMENT PROPERTIES DEFINED FOR EACH LAYER.....	99
FIGURE 72 – SUPPORTS OF THE SHALLOW BEAMS. ....	100
FIGURE 73 – LOADS OR PRESCRIBED DISPLACEMENTS. ....	101
FIGURE 74 – CONCRETE PROPERTIES USED IN THE SIMULATION OF THE A_6_0 SHALLOW BEAMS SERIES. ....	102
FIGURE 75 – STEEL PROPERTIES USED IN THE SIMULATION OF THE A_6_0 SHALLOW BEAMS SERIES. ....	102
FIGURE 76 – EXAMPLE OF GID GRAPHIC VISUALIZATION OF THE ASSIGNED MATERIALS CONSTITUTIVE MODELS IN THE C_10_0 SHALLOW BEAMS SERIES.....	103
FIGURE 77 – INTRODUCTION OF LOAD CASES AND COMBINATIONS TO THE NUMERICAL MODEL: (A) LOAD CASES, (B) COMBINATIONS. ....	104
FIGURE 78 – INTRODUCTION OF THE NEWTON-RAPHSON METHOD AND ARC-LENGTH TECHNIQUE TO THE NUMERICAL MODEL.....	104
FIGURE 79 – NUMERICAL MODEL CALCULATION PROCESS. ....	105

## List of tables

TABLE 1 – COMPOSITION OF SFRSCC .....	27
TABLE 2 – RESULTS OF SFRSCC CHARACTERIZATION.....	28
TABLE 3 – SPECIMEN FAMILIES' DETAIL. ....	30
TABLE 4 – AVERAGE MAXIMUM PULLOUT FORCE, CORRESPONDING LOADED END SLIP AND BOND STRENGTH. ....	32
TABLE 5 – PARAMETERS OF THE BOND MODEL OBTAINED FROM THE INVERSE ANALYSIS IN FBL.....	46
TABLE 6 – VALUES OF THE PARAMETERS OF SFRSCC CONSTITUTIVE MODEL USED IN PULLOUT BENDING TEST SIMULATION. ....	48
TABLE 7 – VALUES OF GFRP MATERIAL PROPERTIES.....	49
TABLE 8 – PARAMETERS OF THE BOND MODEL OBTAINED FROM THE INVERSE ANALYSIS IN FEMIX. ....	52
TABLE 9 – COMPOSITION OF SFRSCC AND SCC USED ON SLAB STRIPS (PER $m^3$ OF CONCRETE). ....	55
TABLE 10 – VALUES OF THE PARAMETERS OF THE CONCRETE CONSTITUTIVE MODEL FOR L_6_0 SERIES.....	61
TABLE 11 – VALUES OF THE PARAMETERS OF THE CONCRETE CONSTITUTIVE MODEL FOR B_8_0 AND C_10_0 SERIES. .....	62
TABLE 12 – VALUES OF THE PARAMETERS OF THE CONCRETE CONSTITUTIVE MODEL FOR B_8_45 AND C_10_45 SERIES.....	62
TABLE 13 – VALUES OF THE CONVENTIONAL STEEL CONSTITUTIVE MODEL.....	63
TABLE 14 – VALUES OF THE PARAMETERS OF THE STEEL WIRES CONSTITUTIVE MODEL.....	65
TABLE 15 – COMBINATION OF ACTIONS USED IN THE BEAM DESIGN.....	72
TABLE 16 – VALUES OF THE PARAMETERS OF THE STEEL STRAND CONSTITUTIVE MODEL. ....	76
TABLE 17 – LOAD CARRYING CAPACITY AT SERVICEABILITY LIMIT STATES.....	78
TABLE 18 – MAXIMUM STRESSES FOR SERVICEABILITY LIMIT STATES.....	82
TABLE 19 – MAXIMUM CRACK WIDTH FOR SERVICEABILITY LIMIT STATES.....	85



# Chapter 1

## 1. Introduction

### 1.1. General

Reinforced concrete (RC) structures are being challenged every day to become more innovative, and rehabilitation is becoming increasingly necessary. For RC structures to have controlled durability, it is critical to pay attention to the design phase, so that no large-scale maintenance, repair, or reinforcement efforts are required, at the very least during the lifetime of the project. This problem brought up the attention of civil engineers towards alternative construction systems.

Traditional RC systems satisfy the structural needs of design, however, nowadays these needs are growing, the building architecture is a lot much diverse, the construction locations are difficult to access and in hostile environments, the design method and construction process is different, and the biggest difficulty is the lack of manpower. The use of composite materials is the next step to build strong, long-lasting projects and achieve greatness in construction.

A composite material that has been studied to substitute conventional steel reinforcement is glass fibre reinforced polymer (GFRP). The advantages of fibre reinforced composite materials over conventional steel include excellent corrosive resistance, high strength-to-weight (10 times higher than steel), excellent fatigue resistance, nonmagnetic properties, and low thermal expansion.

Commonly used concrete mix compositions does not include steel fibres. This is one difference between traditional and advanced reinforcement for concrete structures. Steel fibre reinforced self-compacting concrete (SFRSCC) is one alternative for traditional reinforcement. The randomly distributed discrete fibres increase concrete post-cracking tensile capacity, guarantee ductility, energy absorption and impact resistance when compared to plain concrete. The fundamental reinforcement mechanisms of fibres consist in the capacity of ensuring relatively high stress transfer between the faces of the cracks, by restraining the degeneration of micro-cracks in meso and macro-cracks, which increases the load carrying capacity and stiffness of concrete structures in their cracking stage [1].

Additionally, the use of SFRSCC and GFRP could also be used to enhance the structural performance of RC elements at Serviceability and Ultimate Limit States (SLS and ULS). Furthermore, to optimize the



reinforcing capabilities and to increase the beam's ductility the addition a certain prestress level is an option.

## 1.2. Motivation and objectives

The main objective of this dissertation is to study the application of high-performance materials such as SFRSCC and GFRP bars in construction. The advantages of prestressing both GFRP and steel reinforcement for the design of structural systems is also studied. Furthermore, this dissertation emphasizes the development of numerical simulations for structural design purpose.

Throughout this dissertation the potential of numerical models was studied and a hypothetical case study with a new reinforcing system that combines the benefits provided by the application of SFRSCC and hybrid GFRP-steel reinforcements was developed. This case study is about a 12m length single span prefabricated I beam for an office building.

The composite materials used in the design of the beam are studied to be applied so that the best performance of the project is achieved. The structural behaviour is demonstrated through numerical simulations using structural analysis software's capable of simulating adequately the non-linear behaviour of the materials involved.

In summary, the present work aims to achieve the following objectives:

- ✓ Discover the advantages of using of composite materials in modern construction.
- ✓ Study the behaviour of SFRSCC and GFRP in bending.
- ✓ Perform numerical simulations for predicting the behaviour of a representative structural element made by these materials.
- ✓ Comparison between experimental and numerical results.

## 1.3. Outline of the thesis

The present thesis is divided in seven chapters and is organized as follows:





Chapter 1, introduction, is intended to present, in a brief way, the content of the dissertation, justifying the motivation of this research, and setting out the objectives to be achieved.

Chapter 2, state of the art on high performance materials for structural systems, a literature review analyses the evolution of the understanding of the performance of FRC and FRP in structural systems, highlighting the main properties and advantages of using composite materials in structures. The bond behaviour between FRC and FRP's is appraised and a description of some of the relevant material parameter's behaviour is also included.

Chapter 3, description of the experimental programme developed to characterise the behaviour of the structural elements studied in the dissertation. The bond between GFRP and surrounding Steel Fibre Reinforced Self Compacting Concrete (SFRSCC) is assessed by performing pullout bending tests. The influence of concrete cover thickness and anchorage length of the GFRP bars in bond behaviour is investigated.

Chapter 4, modelling of bond behaviour between GFRP and SFRSCC using computer programs, FBL and FEMIX, respectively. The models are validated with the experimental program results obtained in Chapter 3 and the bond-slip relationship defined.

Chapter 5, numerical simulation of shallow beams. The calibration of the numerical models is assessed and the investigation of the influence of reinforcing shallow beams with GFRP and prestressed steel wires is carried out. In the simulations GUID software was used for generating the data file of FEMIX, which was the software adopted for structural analysis. The results from FEMIX can be presented with GID visualisation facilities. The main objective of the numerical modelling is to determine the constitutive model of the intervening materials in the experimental work because it is by means essential for the numerical modelling of I beams in the next chapter.

Chapter 6, development of a Case Study with prefabricated I beams. Design, and creating a finite element model of the I beam with conventional reinforcement and new reinforcing systems. Five beam bending



test numerical simulations are carried out to study the performance of the new system and the main results, especially in terms of the serviceability limit states. Also, the influence of the GFRP-SFRSCC bond conditions on force-deflection response of I-shaped cross-sectional beams is studied, allowing the slip between the GFRP bars and the surrounding concrete and assuming perfect bond between the concrete and the reinforcement.

Chapter 7, A brief resume of conclusions and a summary of results of the present work is presented.



## Chapter 2

### 2. State of the Art on High Performance Materials for Structural Systems

#### 2.1 Introduction

The growing demand for efficient building structural system with desired levels of performance and safety led to accelerated research in sustainable materials, some of them form part of the microstructure of concretes. The use of high-performance materials and advanced structural systems provides new opportunities to meet global challenges, particularly in civil engineering.

Chloride and carbonation induced corrosion of steel is a well-known weakness that can compromise safe use of reinforced concrete (RC) structures specially in construction close to the coast or in other harsh environment [2]. When steel corrodes, the resulting rust increases the steel bar volume and this expansion creates tensile stresses in the concrete, which can eventually cause cracking, delamination, and spalling. This leads to the need for interventions and rehabilitation, whose costs are, in many cases so high that demolition is the only option with the consequent harmful economic, social, and environmental impacts. There has been an increasing demand for alternative materials and reinforcement to replace usual steel utilizations. Carbon-fibre reinforced polymer (CFRP), aramid fibre-reinforced polymer (AFRP) and glass fibre polymers (GFRP) have recently been studied and received a great deal of interest in these subjects. The nonmagnetic properties, high strength-to-weight, low expansion, and excellent corrosive resistance are some of the characteristics and advantages of this type of materials. Corrosion resistance is particularly attractive for designers. The use of FRP as structural reinforcement may offer life-cycle cost benefits for certain structures as maintenance to repair corroded reinforcement is not necessary.

Among the fibre reinforcements, Glass fibre-reinforced polymer have received increasing attention due to the low cost compared to carbon fibre reinforcements with good high-cost efficiency [3]. GFRP bars show high tensile strength, superior corrosion resistance than steel bars, high strength-to-weight ratio (10 times higher than steel), nonmagnetic properties and low thermal expansion. GFRP bars are currently a cost-competitive alternative to stainless steel bars that are also used in structures where corrosion of reinforcement is a concern and offers many advantages to the designer [4].

The developments on combining FRP's and fibre reinforce concrete (FRC) holds major benefits, because the additional strain capacity allows an increase in flexural strength over the equivalent conventionally



reinforced structures, with beneficial consequences in terms of SLS and ULS design verifications. Also, a more rational use of FRP bars in the tension zone can be reached. There are different types of FRC, that can be classified in the main two classes, tensile strain-softening and tensile strain-hardening fibre reinforced concrete (SSFRC and SHFRC, respectively), whose main difference is the capacity to develop an increase of its tensile capacity after crack initiation, up to a relatively high level of tensile strain [5].

SHFRC contributes significantly to improve the durability of concrete structures due to its quite high post-cracking tensile strength and energy absorption capacity. This performance of SHFRC can also be used for increasing the shear resistance, limit the crack width, and assure ductile failure modes [6]. The materials used in SHFRC depend on the desired characteristics and the availability of suitable economic materials. Conventional fibre reinforced concretes (SSFRC) have coarse aggregate particles and large steel fibres, and on the other hand the modern types of high-performance fibre concrete have small aggregate particles and fillers, reinforced by fine, short fibres. Relatively high content of discrete fibres are used in the production of SHFRC, sometimes with more than one type of fibres [7], in order to assure its strain hardening character and high level of deformability, which promotes the formation of diffuse crack patterns, with benefits on the durability of a RC structure since corrosion is limited.

## 2.2. Fibre Reinforce Polymer (FRP)

The need of finding an attractive competitor to the conventional civil engineering materials for the creation of new structures and strengthening/rehabilitation of existing ones led to a growing awareness amongst civil/structural engineers on the importance of the unique mechanical and in-service properties of fibre reinforced polymer (FRP). This versatile engineered material, valued for its ability to resist corrosion and weather effects and incur very little maintainers costs over time, performs very well in a wide range of applications. FRP composites are nowadays used in aircraft, spacecraft, satellites, ships, submarines, automobiles, chemical processing equipment, sporting goods and civil infrastructure, and there is the potential for common use in medical prosthesis and microelectronic devices.

Fibre reinforced polymers consist mainly in synthetic-based materials, mostly polyester or epoxy resins, as well as non-metallic reinforcing fibres embedded in them like glass, aramid or carbon fibres. Wet lay-up (sheets and fabrics) and prefabricated strips (designed by laminates) and bars are the main types of FRP strengthening systems available in the market [8]. The most common strengthening technique is



based on the application of the FRP on the surface of the elements to be strengthen and is designated as externally bonded reinforcement (EBR) technique. Another technique where FRP's are used is the near surface mounted (NSM), which consists of installing the FRP reinforcement in a groove cut into the concrete surface. One solution to the corrosion problems of steel reinforcement is the use of FRP rods [9], thus the investigation of the bond behaviour of FRP bars to concrete is an important aspect of this alternative reinforcing system.

The applicability of FRP reinforcements to concrete structures offers several advantages, however, these materials generally have a linear elastic response in tension up to failure (described as a brittle failure) and a relatively poor transverse or shear resistance. They also have poor resistance to high temperatures [10]. Moreover, their cost, whether considered per unit weight or on the basis of force carrying capacity, is high in comparison to conventional steel reinforcing bars or prestressing tendons. It is expected that the costs in future years will decrease with increased demand and market share.

FRP can be applied to strengthen beams, columns, and slabs in buildings and infrastructures. One important factor to consider is that with this material is possible to increase strength of structural members even after they have been severely damaged due to loading conditions. Moisture, thermal effects and ultraviolet (UV) radiation play a primary role among the environmental conditions identified as being of primary importance in terms of durability of FRP composites in infrastructural applications. GFRP profiles, for example, are likely to be exposed to rain, humidity or moisture and in some applications, such as bridge columns or in harbours, the material may even be immersed [11].

### 2.3. Fibre Reinforced Concrete (FRC)

Concrete is a composite material comprising of fine and coarse aggregates bonded together into a cement matrix that cures over time. When the aggregate is mixed with dry Portland cement and water, the mixture forms a slurry that is easily poured and shaped into mould. Fibre reinforced concrete (FRC) is a composite material consisting of fibrous material which increases its structural integrity. It includes mixtures of cement, aggregates and discontinuous (short) fibres, whose distribution and orientation depend on the geometry of the structural element, casting technology and rheological properties of the FRC. This type of concrete is particularly attractive for statically indeterminate structures, since cracking control through fibre reinforcement mechanisms provide high levels of stress distribution, improving the load carrying

capacity and deformability levels that are higher than the cracking load and its corresponding deformation [12].

The potentialities of using fibres for an increase in the performance of concrete structures and its extensive research is always evolving. Repairing bridge decks, roads, tunnels, marine and aerospace structures are examples of the application of this high-performance material. The use of this type of materials can potentially decrease the construction time and maintenance costs. Concrete with high levels of compressive strength have a proportional increase of the tensile strength and the Young's modulus obtaining better response in tension, especially in the post cracking regime.

Figure 1 shows the main differences between plain and fibre reinforced concrete having both normal and high strength under uniaxial compression. The compressive relations valid for plain concrete apply for the FRC as well.

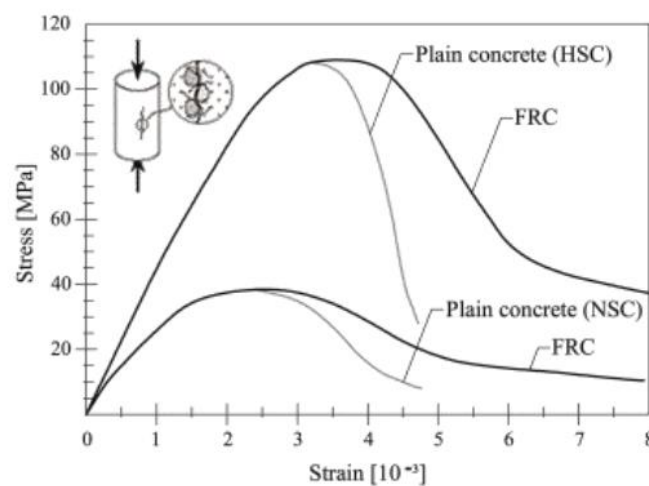


Figure 1 - Difference between plain and fibre reinforced concrete, according to MC2010 [13].

Tensile strength ( $f_{ct}$ ), flexural strength, stress-strain behaviour, modulus of elasticity ( $E_c$ ), crack formation and propagation and compressive strength ( $f_c$ ) of the FRC are the principal mechanical properties studied to verify the qualities of this concrete.

Steel fibre reinforced self-compacting concrete (SFRSCC) has been widely used in civil engineering applications. Optimizing the construction process is one of the main advantages of this composite material, as the discrete fibres can promote the partial or total replacement of the conventional reinforcement. Self-compacting concrete (SCC) is fresh concrete that compacts on its own without the

use of vibrations, promoting faster replacement and less labour, as well as surface finish and durability. The influence in the mechanical properties of the concrete, especially in terms of the design application is due to a good distribution/orientation of the steel fibres in the mix.

Among the aforementioned parameters of SFRSCC, the concrete property most benefited by fibre reinforcement is the energy absorption capacity. Structures with redundant supports, such as slabs on soil and tunnelling lines are protected and more secure because of the increment on the material energy absorption capacity, provided by fibre reinforcement. This enhances the cracking behaviour and increases the load bearing capacity of these structures [14].

## 2.4. Three-dimensional system reinforcement textile (3D-SRT)

The idea of interlacing fibres to make fabric has been around for many years. The common right-angle weaving technique, known as biaxial weaving or flat weaving, is the model used to develop the principles of modern weaving. [15].

3D braided assemblies are textile architectures that have fibres oriented so that both the in-plane and transverse tows are interlocked to form an integrated structure that might have a similar unit cell in all three orthogonal directions [16]. The braiding technique is probably the most ancient production process for textile structures and due to the developments in civil engineering, the production of a wide range of preforms for composite reinforcements with structural function is possible.

The advances in the textile industry allowed the manufacturing of relatively sophisticated 3D reinforcements, herein designated by 3D-SRT, using textile fibres and can be credited largely to the continuous growth of composite materials. Recent automated manufacturing techniques used in sophisticated controlled machines have substantially reduced costs and significantly improved the high-speed and large-volume textile production. A standard horizontal braiding machine used to produce braided composite rods (BCR) for production of 3D-SRT reinforcement is presented in Figure 2.



Figure 2 - Standard horizontal braiding machine developed by the Fibrous Materials Research Group, at University of Minho [17].

The two dimensional planar or conventional (2D) fabrics composite are reinforced in directions parallel, but not orthogonal, to the fabric plane. In this type of reinforcement, the laminated composites should be prepared using several fabric layers because the laminated composites are sensitive to failure by delamination and have poor shear capacity.

Reinforcement in the plane normal to the fabric (three orthogonal directions), provided by three-dimensional (3D) fabrics, enhance composite shear strength, tensile strength and toughness, reduces the chance of composite failure and markedly improve the mechanical properties when incorporated in cement-based composites [18].

3D-SRT (3-Dimensional System Reinforcement Textile) are produced connecting two sets of independent 2D-SRT mesh together with a third set of rods along the thickness, Z direction, of the fabric, referred as spacer rods. These rods provide shear reinforcement and stabilization. Figure 3 shows a manufactured 3D-SRT reinforcement with Glass fibre spacer rods developed at the University of Minho.



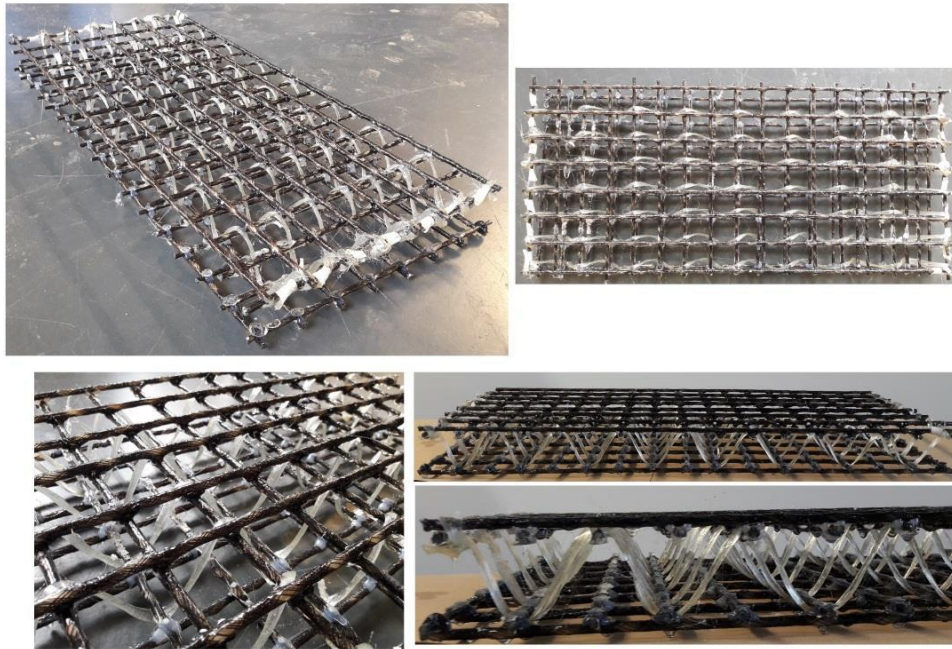


Figure 3 - Samples of 3D-SRT reinforcement for slabs [17].

This information is particularly important because BCR rods (may also be called GFRP bars) will be used as reinforcement in experimental and numerical studies during this dissertation.

## 2.5. Bond behaviour between FRC and FRP bars

Bond performance influences the ultimate load carrying capacity of a reinforced element and typically, the bond of a rebar embedded in concrete is assured by the adhesion and friction between concrete and rebar. The bond means the transfer of stress between the concrete and the reinforcement, such as steel bars, or rods and many other materials, developed at the vicinity of the interface between both materials during the load process of reinforced concrete elements.

Direct pullout test (with centric or eccentric position of bar), splice test, beam test and ring pullout test are the most used tests to evaluate bond mechanisms and behaviour. However, the pullout bending test is widely used. Concrete cover thickness that refers to the depth of the reinforcement inside the element is a parameter analysed in pullout tests. Other parameters used to compare the effectiveness of bond are the bar diameter, bar surface treatment and concrete strength.

Bond is improved with the confinement applied to the surrounding concrete during the pullout process [19].

Figure 4 shows the setup for a beam pullout test.

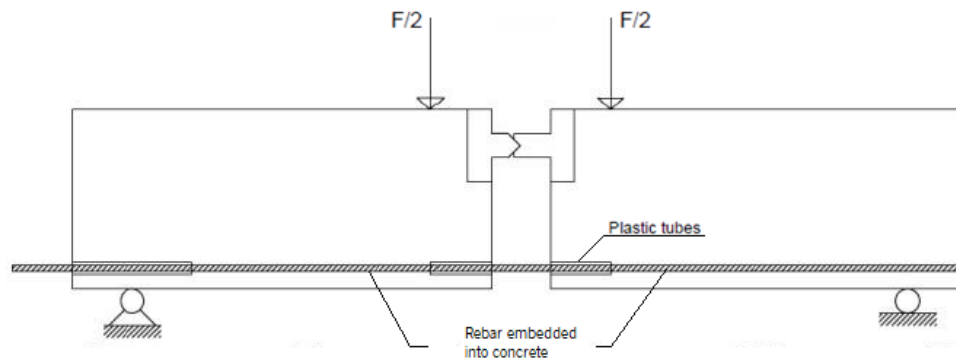


Figure 4 - Pullout bending test [8].

Usually, pullout bending tests have two prismatic concrete blocks connected by a rebar as a flexural reinforcement at bottom part, and a steel hinge at top zone, Figure 4. In the front part of each block, in a small length the bar is unbonded to avoid premature fracture of the concrete in these zones. During the tests, the embedded length is only changed in one block, but a constant embedment length is used in the other. It is important to mention that the rebar is covered by approximately 50 mm long plastic tubes with low elastic modulus in order to create an unbonded length at the edge. The test is performed under displacement control using two LVDT's. LVDT 1 is supported on the bar close to the loaded end section and measures the relative displacement between this section and the concrete front surface of the left block. LVDT 2 is fixed to the free extremity of the bar and measures the relative displacement between the free end part of the bar and the concrete rear surface. [6].

FRP bars have a different behaviour compared to usual steel bars. The most important difference is that FRP reinforcement behaves linearly elastic till failure occurs, whereas conventional steel reinforcement shows a plastic stage with large deformation after yielding. Another difference is the material property and surface texture, that leads to different surface toughness and force transfer mechanism between the reinforcement and concrete.

When the bond behaviour is being evaluated by pullout bending tests, it is fundamental to consider the “*loaded end slip*” that refers to the cross-section of the bar at the beginning of the embedded length where the pullout load is applied and also the “*free end slip*” located at the cross-section of the bar in the extremity of the embedded length. These two locations give the best results recording the applied pullout

force against the relative slip between the bar and concrete. Results of the embedded bar,  $\tau$ - $\delta$  curve where  $\tau$  is the bond shear stress typically must be presented. This value is calculated by Eq. (1), where  $\tau$  can be defined as an average bond stress [28]:

$$\tau_m = \frac{F}{L_e \cdot P_r} \quad (1)$$

where,  $F$  represents the pullout force,  $L_e$  the embedded length and  $P_r$  the perimeter of reinforcing bar.

## 2.6. Relation between fibre orientation and post-cracking behaviour in FRC.

In the last decades, fibres of different shapes and geometries are being used as a discrete reinforcement to control the crack propagation in the concrete matrix and to improve the post-cracking residual strength without extra costs on the propagation and installation of the reinforcement [20]. The fibres prevent that micro-crack join forming meso-cracks, and consequently prevents the opening of these cracks towards macro-cracks. The energy dissipated on the concrete fracture propagation is the property that takes the most benefits from including fibres to the concrete mix, not forgetting that dissipated energy is quite dependent on the fibre orientation and distribution [21].

To optimize the fibre contribution to the post-cracking behaviour, it is important to enhance the distribution and orientation of the fibres at the crack plane [14].

Splitting Tensile Tests executed on SFRSCC specimens extracted from panels have demonstrated the influence of fibre distribution/orientation on the tensile post cracking parameters and the stress crack opening width ( $\sigma$ - $\omega$ ) relationship [22]. Figure 5 shows both the envelope and average force-crack mouth opening response ( $F$ - $\omega$ ) obtained from the splitting tensile tests, when the notch was parallel ( $\Theta = 0^\circ$ ) and perpendicular ( $\Theta = 90^\circ$ ) to the concrete flow direction:

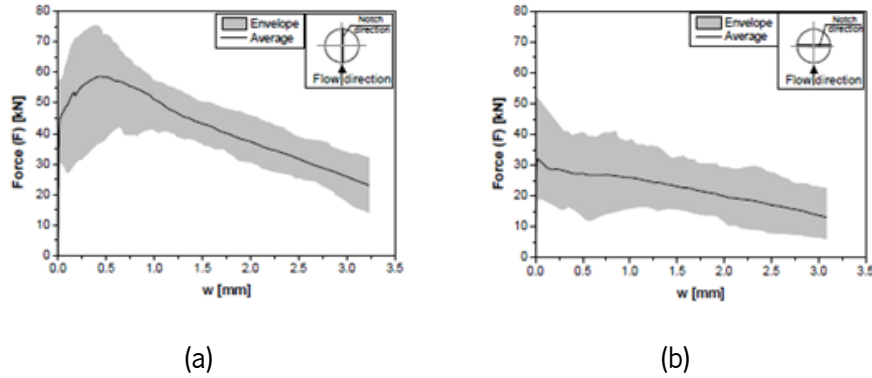


Figure 5 – Force–crack opening width relationship obtained from splitting tensile tests for: (a)  $\theta = 0^\circ$  and (b)  $\theta = 90^\circ$  [22].

When the notch is parallel ( $\theta = 0^\circ$ ) to the concrete flow direction exhibits a non-linear hardening behaviour until the peak load is attained and then follows a softening phase. Contrary to this behaviour, for ( $\theta = 90^\circ$ ) is only observed a softening phase immediately after the crack onset. The preferential fibre alignment is perpendicular to the concrete flow direction and is credited by the rather distinct number of fibres intersecting the crack plane at the specimen's notch.

Figure 6 shows three ( $F-w$ ) relationships (on top, average, and bottom) obtained from splitting tensile tests for SFRSCC panels for ( $\theta = 0^\circ$ ) and ( $\theta = 90^\circ$ ) oriented fibres.

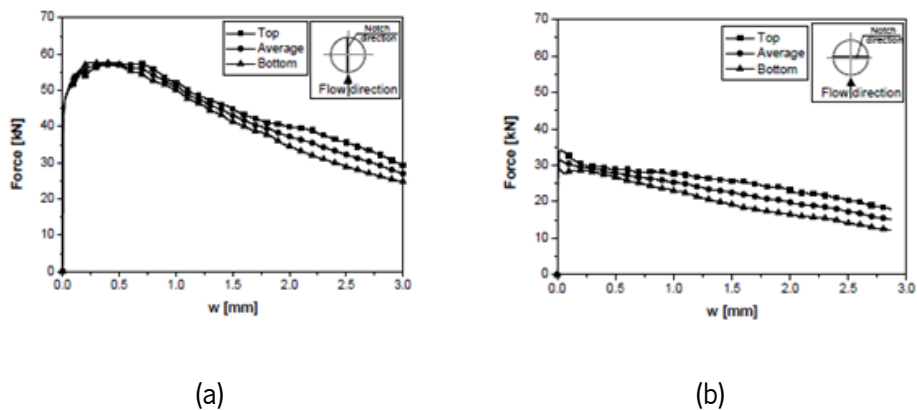


Figure 6 – Nominal tensile stress–crack opening width relationship,  $\sigma-w$ , obtained from splitting tensile test for: (a)  $\theta = 0^\circ$  and (b)  $\theta = 90^\circ$  [22].

The readouts of the LVDT's mounted on the upper surface of the concrete panels shows higher crack opening width compared to the one recorded by the LVDT's mounted at the lower panel surface, see

Figure 6. It is important to note that cracks open asymmetrically, this phenomenon can be ascribed to the variation of the effective fibres along the depth of the panel due to segregation.

The stress–crack opening width ( $\sigma$ – $\omega$ ) relationship is evaluated by uniaxial tensile tests. Figure 7 presents the average and envelope force – crack opening width relationship determined by averaging the readouts of four LVDT's for ( $\theta = 0^\circ$ ) and ( $\theta = 90^\circ$ ).

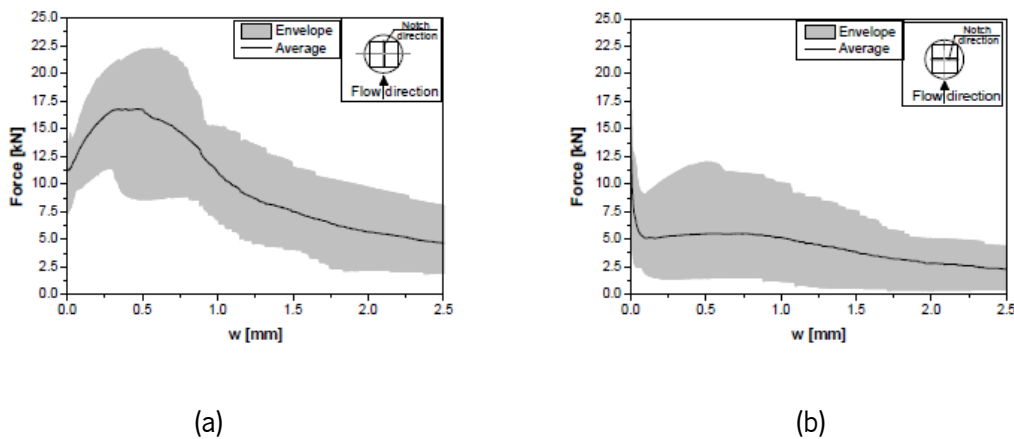
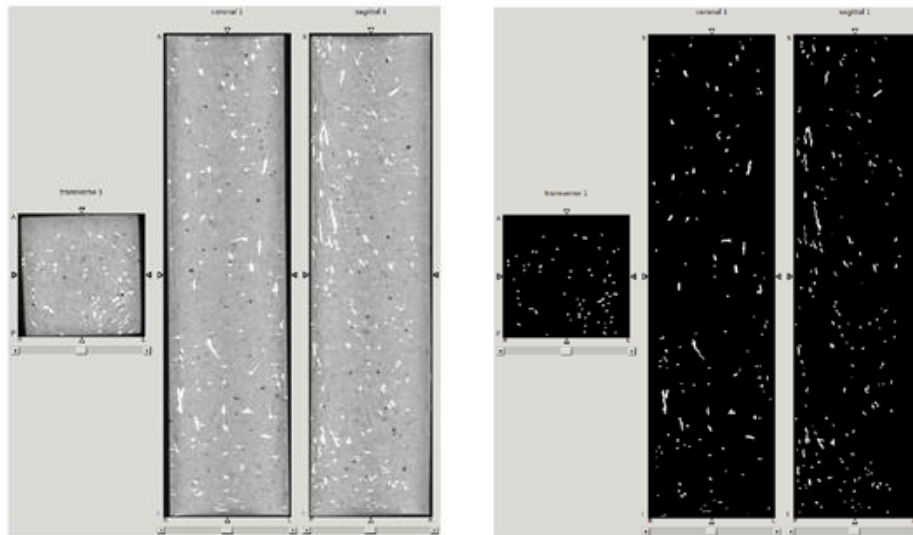


Figure 7 – Force–average crack width relationship,  $F$ – $w$ , obtained from uniaxial tensile tests for: (a)  $\theta = 0^\circ$  and (b)  $\theta = 90^\circ$  [22].

From the analysis of the results, it is possible to conclude that the  $F$ – $\omega$  curve is almost linear up to the crack initiation and when the crack onset the results are similar to what is observed and described in the splitting tensile test, for both ( $\theta = 0^\circ$ ) and ( $\theta = 90^\circ$ ) oriented fibres. The distinct number of fibres at the crack plane is again confirmed to be the cause for the two different behaviours in ( $\theta = 0^\circ$ ) and ( $\theta = 90^\circ$ ).

In order to characterize the distribution and orientation of fibres parameters it is important to assess a suitable experimental procedure [23]. This procedure can be carried out by image processing, where the beam is cut into several pieces and the cross-section of the fibres is used to determine their orientation and distribution [24].

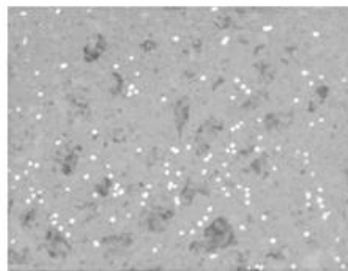
Figure 8 shows the cross section of an exemplary beam used in image processing with the determination of the volume of interest (VOI) and image cropping and Figure 9 shows the image analysis procedure of a beam specimen using “ImageJ” software to recognize steel fibres.



(a)

(b)

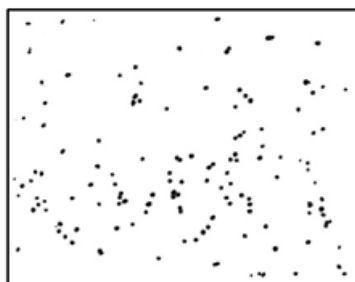
Figure 8 – Cross sections of an exemplary beam: (a) image after VOI selection and (b) after steel fibres segmentation [24].



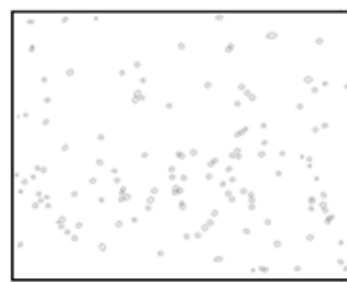
(a)



(b)



(c)



(d)

Figure 9 – Image processing steps: (a) converting a coloured image to greyscale, (b) adjusting a threshold, (c) defining mask, noise and watershed functions, (d) fitting the best ellipse to each fibre [22].



The following equations derive from the image analysis technique that due to its simplicity and relatively low cost is used in these matters [22]:

$$N^f = \frac{N_T^f}{A} \quad (2)$$

The number of fibres per unit area,  $N^f$ , is the ratio between the total number of fibres counted in the image,  $N_T^f$ , and the total area of the image,  $A$ .

The fibre orientation factor,  $\eta_\theta$ , is determined as the average orientation towards a certain plane surface by Eq. (3):

$$\eta_\theta = \frac{1}{N_T^f} \cdot \sum_{i=1}^{N_T^f} \cos \theta_i \quad (3)$$

$N_T^f$  is the total number of fibres that can be determined by counting all the visible ellipses and circles at the cross section,  $\theta$  is the the out-plane angle that is defined as the angle between the fibre's longitudinal axis and a vector orthogonal to the plane.

The fibre segregation parameter,  $\xi_{seg}$  is used to calculate the location of the steel fibres gravity centre, an average value of the coordinates in the Y axis of entire fibres should be determined in the analysed cross-section.

$$\xi_{seg} = \frac{1}{h \cdot N_T^f} \cdot \sum_{i=1}^{N_T^f} \bar{y} \quad (4)$$

where,  $\bar{y}$  is the coordinate in the Y axis of the fibre's gravity centre, and  $h$  is the height (or depth) of the analysed cross-section.

### 2.6.1. Influence of steel fibres on Fracture Energy

The energy absorption capacity is the main material property benefited by fibre reinforcement [25]. Fracture energy of SFRSCC is used in constitutive models for characterizing the post cracking behaviour [26]. The most appropriate test to evaluate the material fracture energy  $G_f$  is the uniaxial tensile test. It requires very high precision measuring devices and a refined control unit.  $G_f$  is defined as the area under the load-deflection curve per unit fractured surface area. Three-point notched bending tests are more usual than the uniaxial tensile test and give suitable results on the material fracture energy [14].

In many studies, it is pointed out that fibres during the crack propagation after matrix cracking, are broken or pulled-out of the matrix due to the bond strength between fibres and matrix [14, 27].

In the absence of experimental data, the fracture energy  $G_F$  for ordinary normal weight concrete may be estimated by Eq. (5), given by the Model Code 2010:

$$G_F = 73 \cdot f_{cm}^{0.18} \quad (5)$$

where,  $f_{cm} = f_{ck} + \Delta_f$  is the mean compressive strength and  $f_{ck}$  is the characteristic compressive strength.

For normal weight concrete the fracture energy depends essentially on the water-cement ratio, the age of the concrete and the maximum aggregate size. Curing conditions and the size of a structural member also have an important effect on experimentally determined  $G_f$  values. It is important to mention that the aggregate type and content seem to affect the fracture energy of concrete much more than the size of aggregates.

The force–deflection relationship is used to evaluate the energy absorption capacity of concrete. Figure 10 shows an example of average force–displacement relationship for 800x100x100 mm beam specimens carried out by three-point bending tests [14].



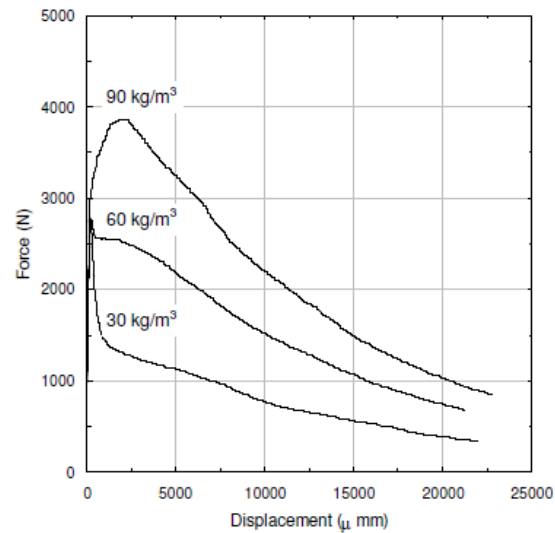


Figure 10 - "Average" force-displacement relationship for series of 30, 60 e 90 kg/m<sup>3</sup> of fibres [14].

The Eq. (6) is used to calculate the maximum stress at notched cross section of beams presented in Figure 10:

$$f_{net} = \frac{3 \cdot F_{max} \cdot L}{2 \cdot b \cdot (h - a)^2} \quad (6)$$

where,  $F_{max}$  is the maximum load,  $L=800$  mm is the specimen span,  $b=100$  mm and  $h=100$  mm is the width and height of the specimen, respectively, and  $a=25$  mm is the depth of the notch.

The results presented in Figure 10 were obtained from tests that considered the specimen dimensions for evaluating the fracture energy of plain concrete. For beams reinforced with FRC, tests should be performed on beams with a span of 500 mm, a width of 150 mm, a height of 150 mm, and a notch depth of 25 mm.

It is possible to conclude in Figure 10 that the maximum load in series reinforced with 30 and 60 kg/m<sup>3</sup> of fibres is almost the same and significant increase in the maximum stress at the notched cross section is only observed on specimens reinforced with 90 kg/m<sup>3</sup> of fibres. There is a decline of force after peak load with the increment of fibre content. In specimens with 90 kg/m<sup>3</sup> of fibres a hardening branch occurs due to the high percentage of fibres bridging the crack surfaces. One of the most important results points is that the energy absorption capacity increases almost linearly with the fibre content.

The nominal values of the material properties can be determined by performing a 3-point bending test on a notched beam according to EN 14651, Figure 11. Parameters,  $f_{R,j}$ , representing the residual flexural tensile strength, are evaluated from the force–crack mouth opening displacement (CMOD), as follows:

$$f_{R,j} = \frac{3 \cdot F_j \cdot l}{2 \cdot b \cdot h_{sp}^2} \quad (7)$$

where,  $f_{R,j}$  is the residual flexural tensile strength corresponding to  $CMOD=CMOD_j$ ,  $F_j$  is the load corresponding to  $CMOD=CMOD_j$ ,  $l$  is the span length,  $b$  is the specimen width and  $h_{sp}$  is the distance between the notch tip and the top of the specimen (125 mm).

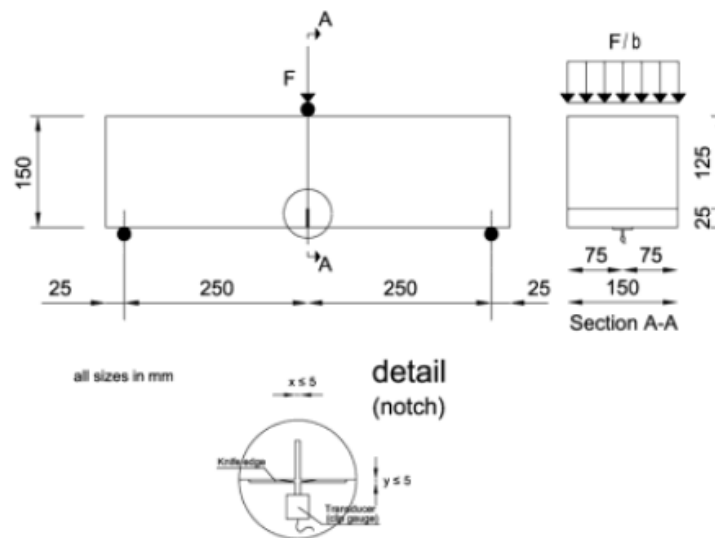


Figure 11 - Test set-up required by EN 14651 (dimensions in mm).

## 2.7. Shear capacity of FRC beams.

Fibre reinforcements increase the shear capacity of concrete, allows a partial or total replacement of steel stirrups without occurring shear failure when suitable level of prestress is applied to the flexural reinforcement and is regarded as an extra flexural reinforcement, whose favourable mechanism for the shear capacity derives from the dowel effect [28]. Conventional shear reinforcements can be partially or totally replaced by steel fibres in concrete depending on the concrete strength class and dosage of steel

fibres in the mix. In structures governed by shear, fibre reinforcement increases the strength and stiffness of the shear stress across cracks.

In a traditionally reinforced beam, the main shear strength contributing mechanisms are:

- Shear strength of compression zone
- Friction in the crack interface (i.e. aggregate interlock)
- Dowel action of longitudinal reinforcement
- Tensile force in stirrups

To measure shear strength of concrete beams reinforced with FRP's is necessary to discuss the effect of the low modulus of elasticity and the non-yielding characteristics of the FRP.

The fib Model Code 2010 presents two approaches for determining the shear strength of fibre reinforced concrete beams. One is based on the concept of residual flexural strength of FRC and the other is based on the modified compression field theory (MCFT) [29].

In this section is presented the first approach based on a modification to the Eurocode model [30] and the MCFT approach.

$$V_{Rd} = V_{Rd,F} + V_{Rd,S} \quad (8)$$

$V_{Rd,F}$  is the component of shear carried by fibres and  $V_{Rd,S}$  is the component of shear due to stirrups.

In MC2010 (chapter 7.7, section 7.7.3), the design value of the shear resistance in structural members with longitudinal bars and without shear reinforcement is evaluated by Eq. (9).

$$V_{Rd,F} = \left\{ \frac{0.18}{\gamma_c} \cdot k \cdot \left[ 100 \cdot \rho_{sl} \cdot \left( 1 + 7.5 \cdot \frac{f_{Ftuk}}{f_{ctk}} \right) \cdot f_{ck} \right]^{\frac{1}{3}} + 0.15 \cdot \sigma_{cp} \right\} \cdot b_w \cdot d \quad (9)$$

where,  $\gamma_c = 1.5$  is the partial safety factor for concrete without fibres,  $k = 1 + \sqrt{\frac{200}{d}} \leq 2.0$  is a factor that takes into account the size effect,  $d$  (mm) is the effective depth of the cross section,  $\rho_{sl} = \frac{A_{sl}}{b_w \cdot d}$  is

the longitudinal reinforcement ratio,  $A_{sl}$  is the cross-sectional area of the longitudinal reinforcement,  $f_{Ftuk}$  is the characteristic post-cracking residual tensile strength of the FRC for shear determined at a crack opening displacement (COD) of  $w_u = 1.5 \text{ mm}$ ,  $f_{ctk}$  is the characteristic value of cylindrical compressive strength,  $f_{ck}$  is the characteristic compressive strength,  $\sigma_{cp} = \frac{N_{ed}}{A_c} < 0.2 \cdot f_{cd}$  is the average axial stress acting in the cross-section (considered positive in compression), for an axial force, due to loading or prestressing actions and  $b_w(\text{mm})$  is the smallest width of the tensile zone of the cross-section.

The design shear resistance of structural members with transverse reinforcements is determined by:

$$V_{Rd} = V_{Rd,F} + V_{Rd,S} \leq V_{Rd,max} \quad (10)$$

$V_{Rd,max}$  is the maximum shear strength without concrete crushing.

$V_{Rd,S}$  is determined according to Eq. (11):

$$V_{Rd,S} = \frac{A_{sw}}{S_w} \cdot z \cdot f_{ywd} \cdot (\cot \theta + \cot \alpha) \cdot \sin \alpha \quad (11)$$

where,  $A_{sw}$  is the shear reinforcement area,  $S_w$  is the longitudinal spacing shear reinforcing bars and  $f_{ywd}$  is the design value of the yield strength of the shear reinforcement.

The shear strength of FRC can be obtained by a recent model, the MCFT model, also implemented in MC2010, shown in Eq. (12):

$$V_{Rd,F} = \frac{1}{\gamma_F} \cdot [k_v \cdot f_{cm} + k_f \cdot f_{Ftuk} \cdot \cot \theta] \cdot b_w \cdot z \quad (12)$$

$f_{Ftuk}$  is the characteristic post-cracking residual tensile strength of FRC determined from axial tensile tests or indirectly from standard three-point bending test results,  $k_f = 0.8$  is a reduction factor taking into account the variation of fibre dispersion and inherent post-cracking performance between three-point bending test specimen and the actual elements for which the shear design is conducted,  $k_v$  is function of the parameter that considers the aggregate size influence,  $k_{dg}$ , and  $\theta$  is the inclination of the critical diagonal crack.

For reinforced concrete (RC) and prestressed concrete (PC), the longitudinal strain (see Figure 12) is calculated at mid depth of the effective shear depth,  $\varepsilon_x$ , as presented in Eq. (13):

$$\varepsilon_x = \begin{cases} \frac{1}{2 \cdot E_s \cdot A_s} \cdot \left( \frac{M_{Ed}}{z} + \frac{V_{Ed} \cdot \cot \theta}{2} + N_{Ed} \cdot \left( \frac{1}{2} \pm \frac{\Delta e}{z} \right) \right) & \text{for RC beams} \\ \frac{\left( \frac{M_{Ed}}{z} + V_{Ed} + N_{Ed} \cdot \frac{(z_p - e_p)}{z} \right)}{2 \cdot \left( \frac{z_s}{z} \cdot E_s \cdot A_s + \frac{z_p}{z} \cdot E_p \cdot A_p \right)} & \text{for PC beams} \end{cases} \quad (13)$$

Within the limits  $0 \leq \varepsilon_x \leq 0.003$

In Eq. (13)  $M_{Ed}$ ,  $V_{Ed}$  and  $N_{Ed}$  are the design values of bending moment, shear and axial forces acting on the cross section, respectively. The bending moment and shear force are taken as positive quantities and the axial force is positive for tension and negative for compression. If the strain  $\varepsilon_x$  is negative (compression), it must be taken as zero.

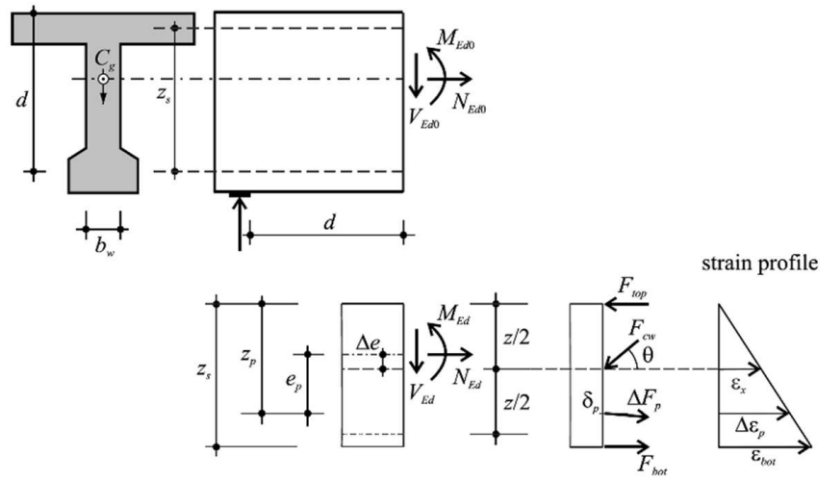


Figure 12 - Definition of cross-sectional parameters, internal loads and strain profile according to MC2010 [13].

The factor  $k_v$  considers both the strain and size effect:

$$k_v = \begin{cases} \frac{0.4}{1 + 1500 \cdot \varepsilon_x} \cdot \frac{1300}{1000 + k_{dg} \cdot z} & \text{for } \rho_w < 0.08 \cdot \sqrt{\frac{f_{ck}}{f_{yk}}} \\ \frac{0.4}{1 + 1500 \cdot \varepsilon_x} & \text{for } \rho_w \geq 0.08 \cdot \sqrt{\frac{f_{ck}}{f_{yk}}} \end{cases} \quad (14)$$

$\rho_w$  represents the transverse reinforcement ratio of the cross section.

The aggregate size parameter in Eq. (15),  $k_{dg}$ , is given by:

$$k_{dg} = \frac{32}{16 + d_g} \geq 0.75 \quad (15)$$

where,  $d_g$  (mm) is the maximum aggregate dimension in the concrete matrix. If the particle size is less than 16 mm, it is suggested to take the value of  $k_{dg}$  equal to 1.

The design shear resistance cannot exceed the crushing capacity of concrete in the web:

$$V_{Rd,max} = k_c \cdot \frac{f_{ck}}{\gamma_c} \cdot b_w \cdot z \cdot \frac{\cot \theta \cdot \cot \alpha}{1 + \cot \theta^2} \quad (16)$$

$k_c = k_\varepsilon \cdot \eta_{fc}$  is a strength reduction factor,  $\alpha$  is the inclination of the transverse reinforcements with the longitudinal axis,  $k_\varepsilon$  is a factor that considers the strain in the web of the structural element and is determined according to the level of approximation defined in MC2010 and  $\eta_{fc}$  considers the effect of more brittle failure for high strength concrete compositions, determined from Eq. (19).

Level of approximation I,  $k_\varepsilon = 0.55$ , Level of approximation II and II, Eq. (17):

$$k_\varepsilon = \frac{1}{1.2 + 55 \cdot \varepsilon_1} \cdot b_w \leq 0.65 \quad (17)$$

$$\varepsilon_1 = \varepsilon_x * (\varepsilon_x + 0.002) * \cot^2 \theta \quad (18)$$

where,  $\varepsilon_x$  is the longitudinal strain level in the mid-depth of the cross section and  $\theta$  is inclination of the principal compressive stress in the web, relative to the longitudinal axis of the member.

$$\eta_{fc} = \left( \frac{30}{f_{ck}} \right)^{\frac{1}{3}} \leq 1.0 \quad (f_{ck} \text{ in MPa}) \quad (19)$$

The angle of compressive stress field ( $\theta$ ) for FRC is calculated by:

$$29^\circ + 7000 \cdot \varepsilon_x \leq \theta \leq 45^\circ \quad (20)$$

## Chapter 3

### 3. Bond Behaviour Between GFRP and SFRSCC

The evaluation of structural components should be conducted through experimental programs that give relevant information about the main material properties of the intervening materials in the tests. An important consideration when evaluating a structural system in this field of study is the flexural behaviour of concrete (or FRC). One important key issue to better understand the flexural behaviour is the bond mechanism of reinforcing bars as internal reinforcements for concrete members. For this reason, this chapter presents an experimental programme on bond behaviour between GFRP bars and steel fibre reinforced self-compacting concrete (SFRSCC) by carrying out pullout bending tests. The influence of anchorage length and SFRSCC cover thickness in the bond behaviour was investigated. Furthermore, the recorded response of the series evaluated on the tests is presented and discussed.

#### 3.1. Experimental Program

In the present experimental program, a total of 18 pullout bending tests were carried out to study the bond behaviour of GFRP bars embedded in SFRSCC. The tests were conducted at the laboratory of the company CiviTest (Research of New Materials for Civil Engineering) where a report was elaborated and supplied by the company.

##### 3.1.1. Materials Properties

The pullout bending specimens were produced from self-compacting concrete reinforced with 60 kg/m<sup>3</sup> of hooked-end steel fibres. The SFRSCC mix is presented in Table 1. Ordinary Portland cement labelled as CEM I 42.5 R, fine and coarse river sand and crushed granite gravel aggregate of 4.76 to 12.7 mm size were used. The production of the specimen also contained hooked end steel fibres with configuration length ( $l_{fr}$ ) equal to 33mm, aspect ratio (*i.e.*  $l_{fr} / \phi_{fr}$ ) equal to 60, and a tensile strength around 1100 MPa and polymeric fibres of 12mm length. The concrete mixture showed good homogeneity and cohesion, and the average spread measured about 750 mm (SF2 Class), Figure 13.



Table 1 – Composition of SFRSCC

<b>Components</b>	<b>Quantity (<math>\frac{kg}{m^3}</math>)</b>
Cement (CEM I 42.5 R)	376.00
Water	196.20
Superplasticiser (BASF SK617)	11.516
Fly ash	200.00
Fine river sand (0-2.38 mm)	156.21
Coarse river sand (0-4.76 mm)	782.07
Crushed granite (4.76-12.70 mm)	625.86
Hooked end steel fibers	60.00
Polymeric fibers	2.00

Four specimens of 600 x 150 x 150 mm and six cubes of 150 x 150 x 150 mm were prepared to evaluate the flexural and compressive strength of SFRSCC, respectively. Prior to those tests, four cylinders of Ø150 x 300 mm were used to determine the Young's modulus of the self-compacting concrete. The compressive strength and the flexural behaviour were assessed after 28 days of concrete casting operations. The average values of concrete compressive strength and Young's modulus were 50.23 MPa and 26.74 GPa, respectively. Table 2 summarises the results of the characterization of the concrete used to manufacture the test specimens.



Figure 13 – SFRSCC slump flow test.

Table 2 – Results of SFRSCC characterization.

	<i>ffct,L</i> (MPa)	<i>fR,1</i> (MPa)	<i>fR,2</i> (MPa)	<i>fR,3</i> (MPa)	<i>fR,4</i> (MPa)	$\sigma$	<i>fcc</i> (MPa)
Cylinder 1	5.70	9.85	9.83	7.93	6.63	–	–
Cylinder 2	5.48	9.61	9.21	7.50	5.96	–	–
Cylinder 3	5.63	10.94	10.05	8.92	7.66	–	–
Cylinder 4	5.52	8.11	7.79	6.43	4.94	–	–
Average values	5.60	10.14	9.70	8.11	6.75	26,74	50.53
Standard deviation	0.11	0.71	0.43	0.73	0.85	0.71	1.16
Percentage standard deviation	2%	12%	11%	13%	18%	2.46%	2.30%

GFRP bars of Ø5mm were subjected to tensile tests to determine their mechanical properties, as shown in Figure 14. The tensile test determined the strength, elasticity, and deformability of the composite reinforcement.

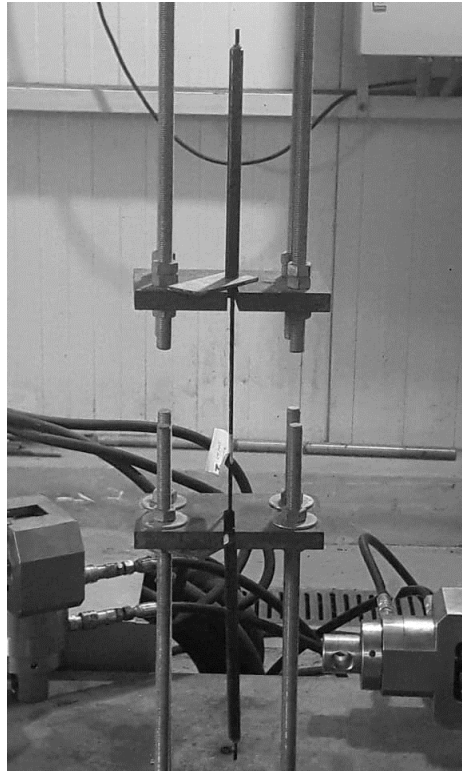


Figure 14 - Example of tensile test on GFRP bar [28].

The obtained values for the Young's modulus of the GFRP bar were 44.81 GPa and tensile strength of 945.56 MPa was achieved. As previous mentioned in the State of Art section, the GFRP bars have lower modulus of elasticity and inferior bond strength comparing to conventional steel bars.  $\sigma$

### 3.1.2. Pullout bending test procedure

In this experimental program, the test layout adopted for evaluating the bond between GFRP and SFRSCC is similar to that proposed by RILEM [31]. The specimen comprises two SFRSCC blocks measuring 350 mm in length and a transversal section (measuring 75 x 150 mm) connected by a steel hinge at the top zone and a  $\varnothing 5$  mm GFRP bar as flexural reinforcement at the bottom part. Two different series of concrete cover thickness, 15 and 25 mm, with different anchorage length ( $L_b$ ), 90 mm, 140 mm and 200 mm were examined to evaluate their influence on the bond behaviour. The anchorage length of the GFRP bars was only changed in on side of the specimen, on the other side the bar was embedded almost in the entire length. Figure 15 and Figure 16 shows the process of specimen's production and the detail of the specimen moments before the pullout test, respectively.



(a)



(b)

Figure 15 – Specimen's production: a) mould, b) appearance of specimens after cast.

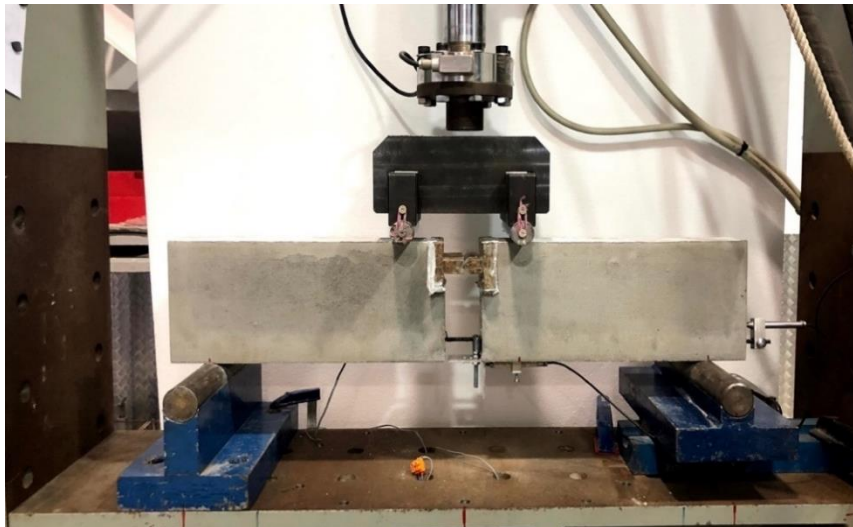


Figure 16 – Detail of the specimen before pullout test.

Specimens were identified by assuming labels shown in the first column of Table 3. The first set of symbols of the labels denoted as C15 (15 mm) or C25 (25 mm) represents the concrete cover thickness, and the second set of symbols refers to the anchorage length. For example, the label C15LB140 corresponds to the specimen with a concrete cover thickness of 15 mm (C15) and anchorage length of 140 mm (LB140).

Table 3 – Specimen families' detail.

<b>Families</b>	<b>Specimen's quantities [un]</b>	<b>Anchorage Length [mm]</b>
C15LB90	03	90 (Lb90)
C15LB140	03	140 (Lb140)
C15LB200	03	200 (Lb200)
C25LB90	03	90 (Lb90)
C25LB140	03	140 (Lb140)
C25LB200	03	200 (Lb200)

Figure 17 depicts the experimental test setup configuration used to evaluate the bond behaviour between GFRP and surrounding SFRSCC. Two linear transducers (LVDT) were used to measure the displacements and the slip at the loaded and free ends of GFRP bars. LVDT1 is used to control the slip at the loaded end, while LVDT2 is adopted to control the slip at the free end, both with a displacement range of  $\pm 5$  mm and precision of 25  $\mu\text{m}$ . Also, a strain gauge with a length of 5 mm was installed to the cross section of the bar to record the strains in the bar during the test. Pullout bending tests directly correlate the pullout

force applied to the GFRP bar and the corresponding values of loaded end slip (using the records from LVDT1 and subtracting the elastic deformation of the GFRP between the section of the GFRP bar where LVDT1 is mounted and the loaded end section) and free end slip (using the records from LVDT2) [32].

At the loaded end, a PVC tube with 50 mm length was placed surrounding the GFRP bar to prevent the bond between concrete and the bar and, consequently, avoid premature fracture of the SFRSCC in these zones.

The specimens were subjected to bending on an EMM-04 machine. A load was applied using a load cell with a maximum load carrying capacity of 50 kN and the tests was displacement controlled at a speed of 5  $\mu\text{m/s}$ . The pullout force was calculated by the strain recorded in the strain gauge and considering the measured cross section area of the bar.

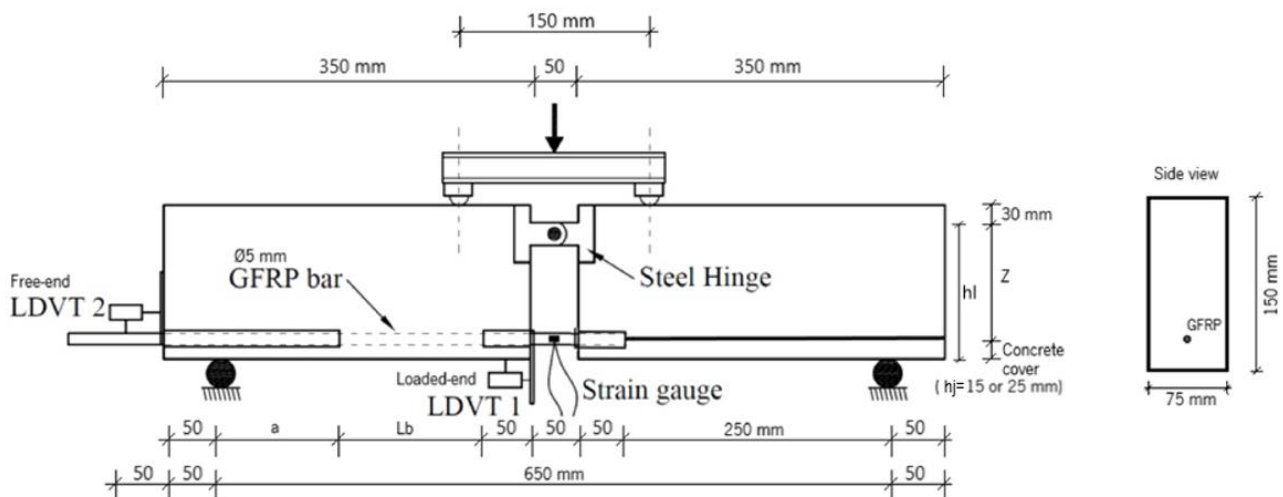


Figure 17 – Pullout bending test setup details.

For all specimens, the pullout force was observed and registered. The discussion of the results is presented in the next section.

### 3.2. Test results and discussion

The test results include the bond stress-slip relationship obtained for the series of the evaluated specimens. It was determined the average bond stress ( $\bar{\tau}_m$ ), as the pullout load divided by the bonded

area, therefore assumed constant along the anchorage length ( $L_b$ ), and for each load it was recorded the loaded and free end slip, ( $S_{lp}$ ) and ( $S_{fp}$ ) respectively.

The maximum average pullout force ( $F_{max}$ ), the corresponding loaded end slip ( $S_{lp}$ ) and average bond strength ( $\bar{\tau}_{max}$ ) for each specimen family is presented in Table 4. It is noted that, as expected, the  $\bar{\tau}_{max}$  has decreased with the increase of bond length. The pullout force and bond strength of the GFRP bar were calculated by Eq. (21) and (22), respectively.

$$F_{max} = \frac{Fa}{2 * (hl - hj)} \quad (21)$$

where,  $Fa$  (kN) is the vertical force induced by the servo actuator,  $hl$  (mm) is the height from the centre of the steel hinge to the lower limit of the specimen and  $hj$  (mm) refers to the height from the centre of the GFRP bar to the limit of the specimen.

$$\bar{\tau}_{max} = \frac{\bar{F}_{max}}{\pi * \emptyset * L_b} \quad (22)$$

where,  $\bar{F}_{max}$  (kN) is the maximum average applied pullout force,  $\emptyset$  is the diameter of the GFRP bar (mm) and  $L_b$  is the anchorage length (mm).

Table 4 – Average maximum pullout force, corresponding loaded end slip and bond strength.

	C15LB90	C15LB140	C15LB200	C25LB90	C25LB140	C25LB200
$\bar{F}_{max}$ (kN)	16.00	16.70	16.00	14.90	15.30	16.00
$S_{lp}$ (mm)	1.71	1.71	1.90	2.23	2.22	2.00
$\bar{\tau}_{max}$ (MPa)	11.32	7.59	5.09	10.54	6.96	5.09

Figure 18 show the relationships between the pullout force and slip at loaded and free ends for all specimens.

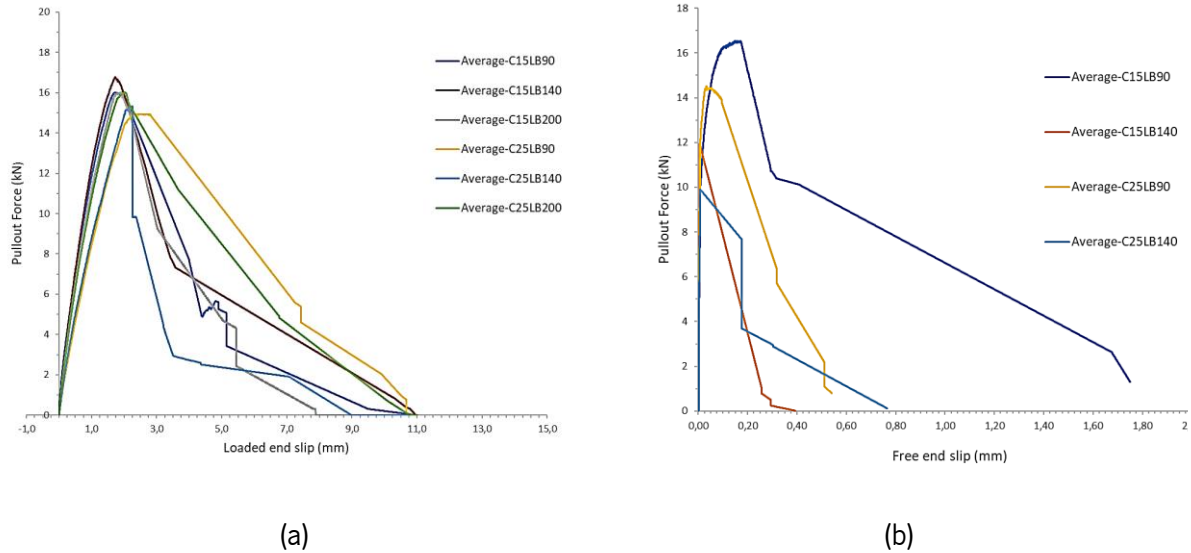


Figure 18 – Relationships between the applied pullout force and slip at: a) Loaded end, b) Free end.

Pullout force *versus* loaded end slip response is characterized by a short linear branch, followed by a nonlinear response up to peak due to the increase of damage, well represented in previous figures. The peak load occurred for a loaded end slip in a range of 1.7 mm and 2.2 mm. It is noted that in C25LB90 and C25LB200 series the decrease of the pullout force with the increase of the slip is much smaller, a residual pullout force due to the friction of resistance between the GFRP and SFRSCC is shown.

In C15LB90 series, the GFRP bars did not fail, but there was the greatest slip compared to all other series, as shown in Figure 19a. In contrary to what happened to the C15LB90 specimen, Figure 19b depicts a GFRP rupture in C25LB140, which is repeated in all other specimen except in C15LB90 and C25LB90.

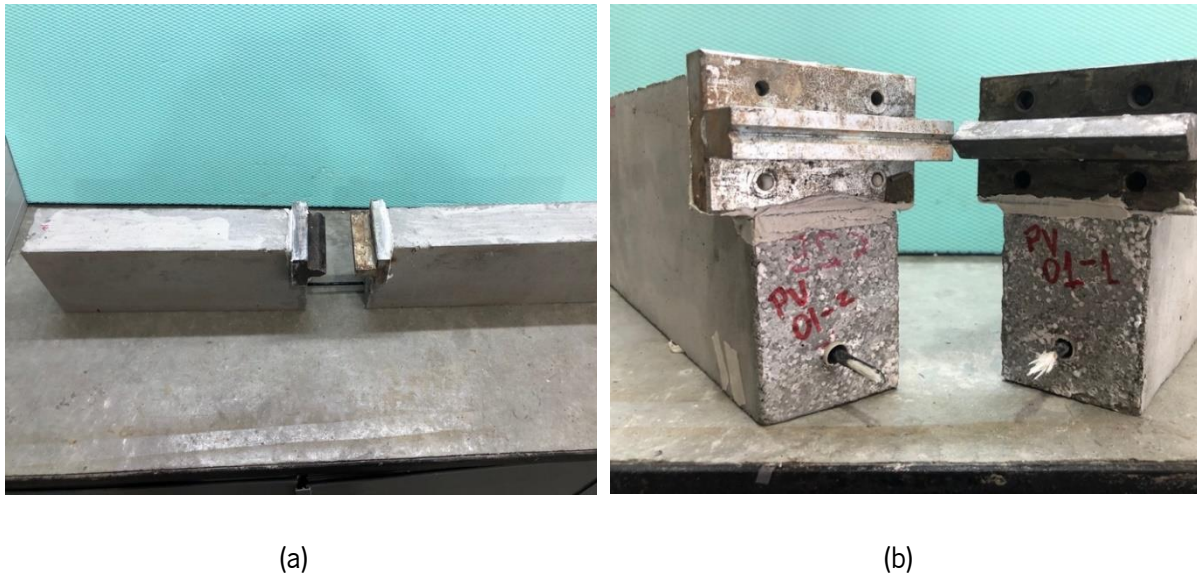


Figure 19 – Detail of the specimens after the pullout test: a) C15LB90, b) C25LB140.

The bond performance of GFRP bars embedded in SFRSCC was assessed by investigating the influence of anchorage length ( $L_b$ ) and concrete cover thickness. From the obtained results it is possible to conclude that pullout force increased with the increase of the anchorage length in all series, however in the C15 series this linearity wasn't perfect, probably some experimental error has occurred. As expected, the values of the average bond stress ( $\bar{\tau}_{max}$ ) decreased with the increase of anchorage length, also in all series. According to the relationship between different anchorage lengths, the smallest anchorage should be around 90 mm, this conclusion is based on the fact that the maximum average bonding stress reached the highest values until the slip, showing that in some specimens of this series the GFRP bar failure occurs. The maximum pullout force values were achieved when the anchorage length is twenty-eight times its diameter (140 mm).

Presented results and information of the experimental program showed no relationship between the applied force to the GFRP bar and the two concrete cover thickness analysed (15 mm and 25 mm).



## Chapter 4

### 4. Modelling the Bond Behaviour Between GFRP Bars and SFRSCC

In the previous chapter it was presented the bond behaviour of GFRP bars embedded in SFRSCC. The main objective of this section is to calibrate the parameters of the local bond-slip relationship using the experimental results of pullout tests assessed previously. The parameters of the bond-slip relationship were determined, so that results of pullout tests could be particularly predicted in terms of applied pullout force *versus* slip at the loaded end of the specimens.

For this purpose, analytical modelling was conducted using the FBL software that solves the differential equations that govern the bond behaviour along the bond length of the reinforcing bar (GFRP in this case) and determines the pullout force ( $F$ ) and the respective slip ( $\delta$ ) at loaded or free ends [33]. The analytical model developed in this section calibrated the  $F - \delta$  curves at the loaded end of each series. The parameters of local bond-slip law for each experimentally tested specimen series were determined from inverse analysis using this software and the proposed method.

Apart from the analytical modelling, the bond tests were simulated numerically by using FEMIX computer program, which is based on the finite element method (FEM). To simulate the bond between GFRP bar and SFRSCC, an interface finite element with a non-linear constitutive law was used, whose constitutive law was defined from the FBL inverse analysis. The finite element model was calibrated so that the non-linear interface finite element presented an acceptable capability to predict the bond behaviour between GFRP and SFRSCC in the context of bending behaviour.

Both the analytical and numerical approaches were compared and validated with the experimental results presented in Chapter 3.

#### 4.1. Local bond stress-slip relationship

The bond of the reinforcement in concrete is intrinsically a three-dimensional problem. As a result of its complexity, the bond behaviour is typically analysed as a uniaxial problem, and the local bond stress-slip relationship ( $\tau - \delta$ ) between the reinforcement and the concrete must be determined in order to solve

the differential equation governing that behaviour [8]. Based on the experimental results of pullout force *versus* slip from the experimental program presented in the previous chapter, the developed model was calibrated, and the constitutive bond-slip laws were attained.

An interface finite element with a non-linear constitutive law was used to simulate the bond between the GFRP bar and the SFRSCC. The bond-slip relationship that defines the sliding behaviour of such interface elements is illustrated in Figure 20.

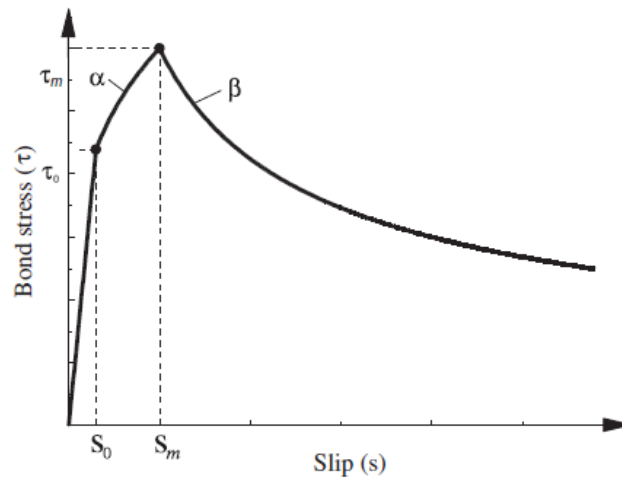


Figure 20 – General bond-slip law

Equation (23) characterizes the non-linear behaviour of the interface element:

$$\tau(s) = \begin{cases} \left(\frac{\tau_0}{S_0}\right) S & S < S_0 \\ \left(\frac{S}{S_m}\right)^\alpha \tau_m & S_0 \leq S < S_m \\ \left(\frac{S}{S_m}\right)^\beta \tau_m & S \geq S_m \end{cases} \quad (23)$$

where  $\tau_0$  and  $S_0$  are, respectively, the bond stress and the slip at the end of the first branch,  $\tau_m$  defines the bond strength and  $S_m$  the corresponding slip. Parameter  $\alpha$  defines the shape of the pre-peak branch (bond behaviour up to peak stress) and  $\beta$  defines the post-peak branch (bond behaviour in descending branch).

The values for  $\alpha$  range between 0 and 1. For  $\alpha = 1$  a pre-peak linear branch is assumed, while for  $\alpha = 0$  a constant bond stress of  $\tau_m$  is considered in the interval  $S_0 \leq S < S_m$ . The decay of bond stress transference is simulated by increasing the value of  $\beta$  from 0 to infinity. The bond stress equal to the bond strength is assumed for  $S \geq S_m$  when  $\beta = 0$  [32].

Figure 21 shows how parameters  $\alpha$  and  $\beta$  influence the shape of the pre-peak and post-peak nonlinear branches, here represented as  $\alpha_1$  and  $\alpha_2$ , respectively.

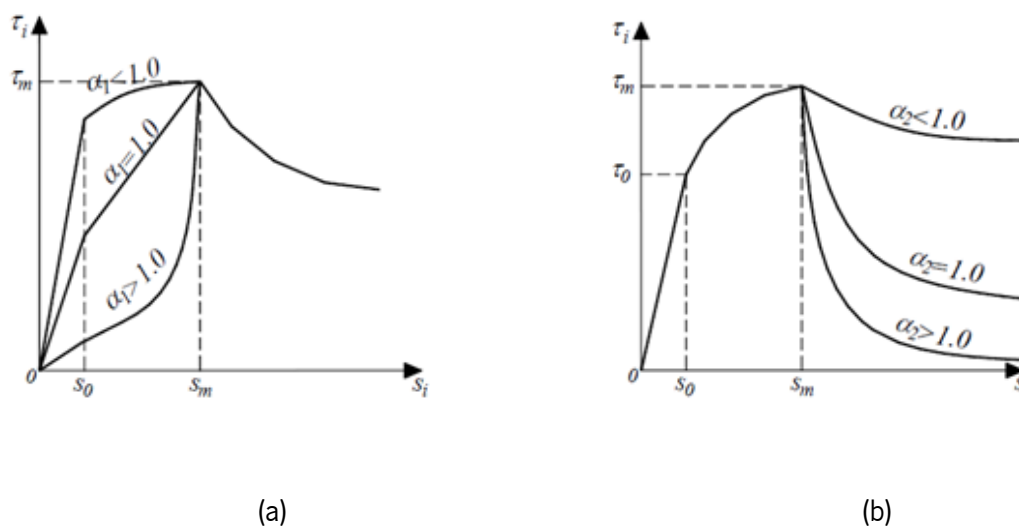


Figure 21 – Illustration of the influence of the value of parameters  $\alpha$  and  $\beta$  (represented as  $\alpha_1$  and  $\alpha_2$ , respectively) in the shape of the bond-slip relationship: a) pre-peak phase, b) post-peak phase.

#### 4.1.1. Analytical study of bond-slip relationships determined from inverse analysis using the FBL software

As mentioned before, an inverse analysis using FBL software was carried out to determine the local bond-slip law for GFRP bars embedded into SFRSCC for each experimentally tested series. The FBL software solves the differential equations that governs the bond behaviour along the bond length of the GFRP bar and determines the pullout force ( $F$ ), the respective slip ( $\delta$ ) at loaded or free ends and the parameters of local-bond slip laws that fit the differential equations as accurately as possible.

The local bond-slip laws available on FBL are the NLML101, NLML102 and NLML103 which define different bond slip-stress relationship. The non-linear material law 101 is defined only by parameters  $S_m$  (slip corresponding to bond strength),  $\tau_m$  (bond strength) and factors  $\alpha$  and  $\beta$  (shape of pre-peak and post peak branch), Figure 22a. The NLML102 is described by four points where the slip and bond strength parameters are defined ( $S_1, \tau_1; S_2, \tau_2; S_m, \tau_m; S_4, \tau_4$ ), Figure 22b. The NLML103 was the law used in the inverse analysis in FBL and is defined by parameters  $S_0, \tau_m, S_m, \alpha$  and  $\beta$ , described on the previous section and illustrated in Figure 20.

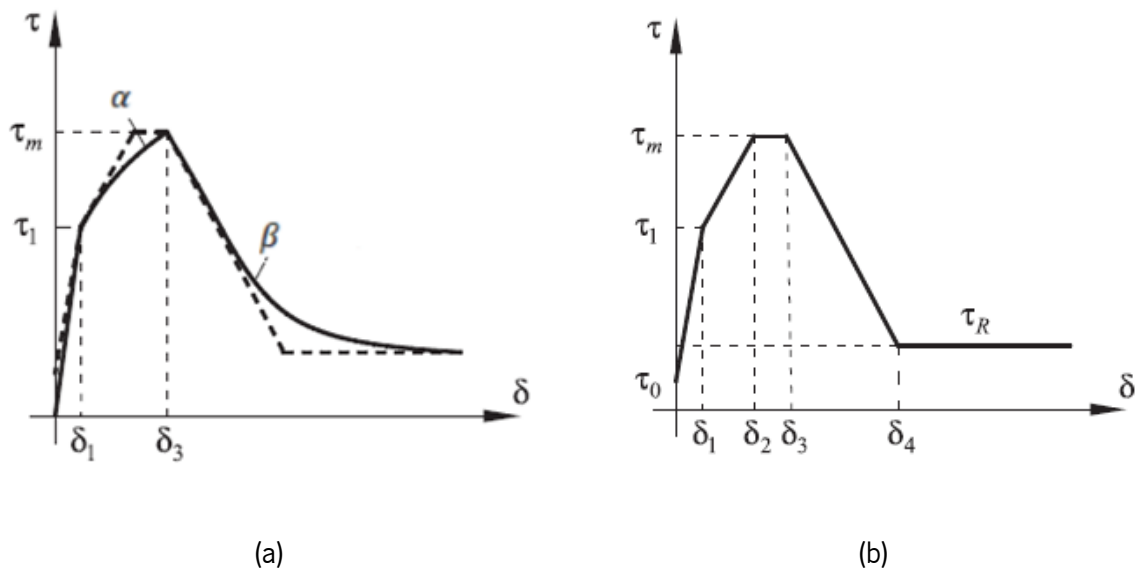


Figure 22 – Different local bond-laws: a) transformation from NLML102 to NLML101, b) NLML102.

The second-order differential equation that governs the slip of GFRP bonded into concrete is derived as follows:

$$\frac{d^2 \delta(x)}{dx^2} - J\tau(\delta(x)) = 0 \quad (24)$$

where  $J$  is the ratio between the perimeter ( $\pi d_f$ ) and the axial stiffness ( $E_f A_f$ ) of the reinforcing bar, being  $d_f$ ,  $E_f$  and  $A_f$ , respectively, the diameter, the longitudinal modulus of elasticity and the cross-sectional area of the bar.  $\delta(x)$  represents the slip between GFRP and the surrounding concrete at a section  $x$  from the free end of the specimen.

Assuming that the GFRP has a linear elastic behaviour, based on Hook's law, Eq.(25) can be deduced:

$$\sigma_f(x) = E_f \frac{d\delta(x)}{d_x} \quad (25)$$

where  $\sigma_f$  is the axial tensile stress of the GFRP bar.

The distribution of bond shear stress  $\tau(x)$  along the bond length is given by Eq.(26), based on Eq.(25).

$$\tau(x) = \frac{1}{J} \frac{d^2\delta(x)}{d_x^2} \quad (26)$$

Using the experimental results obtained in Chapter 3, the main purpose of FBL is to obtain the parameters  $S_0$ ,  $\tau_m$ ,  $S_m$ ,  $\alpha$  and  $\beta$  of equation (23), that fit the differential equation (25) with as much accuracy as possible.

FBL software is based on the theoretical condition of pullout force for Finite Bond Length. The debonding process for embedded bars (GFRP for example) into concrete can be analysed by solving the equation (24) imposing appropriate boundary conditions for a slip at the extremity of the bond transfer length ( $L_{tr}$ ), which cannot exceed the available finite bond length ( $L_f$ ), [6]. The main steps of the algorithm used in the FBL software to determine the  $F - \delta$  curves at the loaded end and the local bond-law of each series are stated below, based on [8]:

- In the first step is necessary to impose values for the parameters  $S_0$ ,  $\tau_m$ ,  $S_m$ ,  $\alpha$  and  $\beta$  defining the bond-slip ( $\tau - \delta$ ) relationship in the equation (23). The process to determine the error,  $e$ , defined as the area between the experimental and numerical curves is initialized.
- When the free end slip is onset, the loaded end slip is calculated.

- For the experimental  $i$ th scan reading, the free end slip, the loaded end slip and the pullout force are read.
- Taking the free end slip and solving Eq.(24), the numerical pullout force at the loaded end is calculated.
- The error,  $e$ , associated with the pullout force at the loaded end is calculated. This error is characterized as  $\frac{|A_{F-\delta}^{model} - A_{F-\delta}^{exp}|}{A_{F-\delta}^{exp}} * 100$ , where  $A_{F-\delta}^{model}$  is the area of the obtained theoretical  $F - \delta$  curves and  $A_{F-\delta}^{exp}$  is the area under the average  $F - \delta$  of the experimental curves.
- The process is updated until finding the minimum error.

The tolerance introduced in the analysis is smaller than 1% which means that the validation of the bond-slip parameters is conditioned by the restriction of ensuring similar values for the numerical and experimental peak pullout force and its corresponding slip. The independent parameters are searched exhaustively based on a predefined range and a predefined step.

The FBL interface relative to the analysis carried out to C15LB90 series is illustrated in Figure 23. This figure shows that FLB presents the main imputed properties of the materials and the parameters used in the inverse analysis that define the bond-slip relationship, the graphically  $F - \delta$  response of the analysis, the error,  $e$ , and also the determined local bond slip law. One more useful feature of this software is the available “Plot” interface that clearly displays the local bond law for the evaluated series. This interface represents the curves obtained by the imputed values in the bond slip-stress relationship.

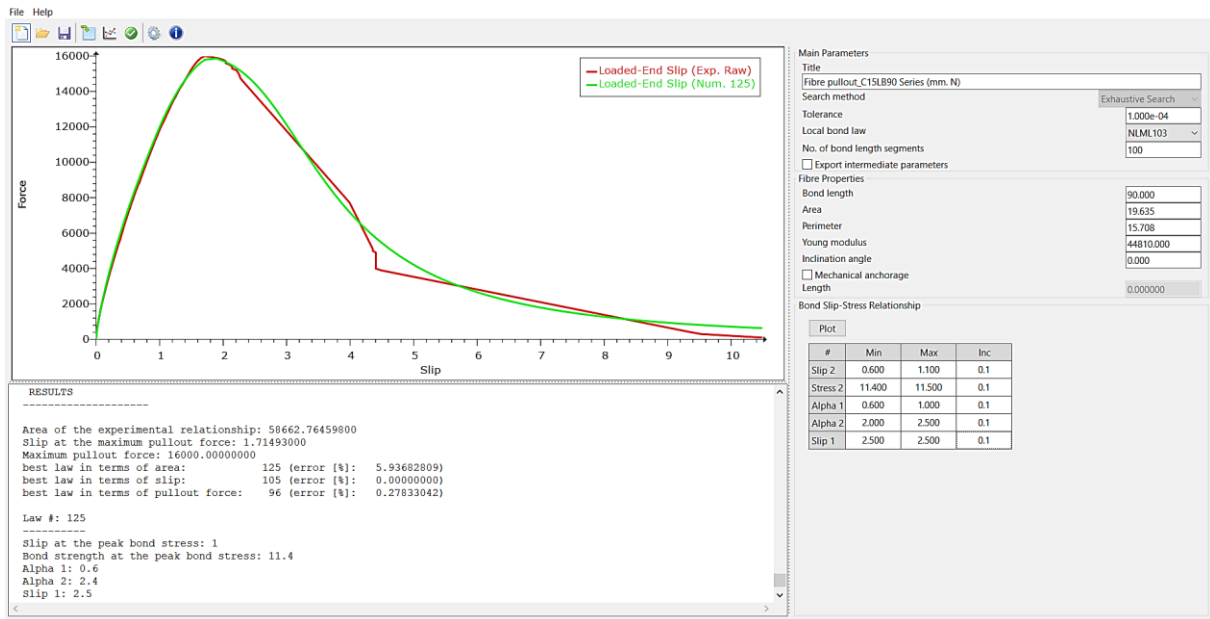


Figure 23 – FBL interface for the analysis of C15LB90 series.

To carry out the analytical study in FBL, firstly is necessary to introduce the data relating to the local bond law and the fibre properties of the series that will be studied, see Figure 24a. FBL reads the data file where the parameters were introduced and then displays those parameters on his interface, Figure 24b. When the parameters are directly modified in FBL, the data file is updated.

```

<LBSSR_DATA_FILE>

<MAIN_PARAMETERS>
MAIN_TITLE = Fibre pullout_C15LB90 Series (mm. N) ;
SEARCH_METHOD = _EXHAUSTIVE_SEARCH ;
TOLERANCE = 0.0001 ;
LOCAL_BOND_STRESS_SLIP_RELATIONSHIP = _NLML103 ;
NUMBER_OF_BOND_LENGTH_SEGMENTS = 100 ;
EXPORT_INTERMEDIATE_PARAMETERS = _NO ;
</MAIN_PARAMETERS>

<NLML103>
SLIP_AT_PEAK_BOND_STRESS_RANGE = [ 0.6 - 1.1 ] ;
SLIP_AT_PEAK_BOND_STRESS_STEP = 0.1 ;

BOND_STRENGTH_RANGE = [ 11.4 - 11.5 ] ;
BOND_STRENGTH_STEP = 0.1 ;

ALPHA1_RANGE = [ 0.6 - 1 ] ;
ALPHA1_STEP = 0.1 ;

ALPHA2_RANGE = [ 2 - 2.5 ] ;
ALPHA2_STEP = 0.1 ;

S1_RANGE = [ 2.5 - 2.5 ] ;
S1_STEP = 0.1 ;
</NLML103>

<FIBER_PROPERTIES>
90 19.635 15.708 44810 0 _NO 0 ;
</FIBER_PROPERTIES>

</LBSSR_DATA_FILE>
    
```

(a)

The screenshot shows the 'Main Parameters' panel with the following values:

- Title: Fibre pullout\_C15LB90 Series (mm. N)
- Search method: Exhaustive Search
- Tolerance: 1.000e-04
- Local bond law: NLML103
- No. of bond length segments: 100
- Export intermediate parameters:
- Fibre Properties: Bond length (90.000), Area (19.635), Perimeter (15.708), Young modulus (44810.000), Inclination angle (0.000)
- Mechanical anchorage:
- Length: 0.000000

The 'Bond Slip-Stress Relationship' table is updated as follows:

#	Min	Max	Inc
Slip 2	0.600	1.100	0.100
Stress 2	11.400	11.500	0.100
Alpha 1	0.600	1.000	0.100
Alpha 2	2.000	2.500	0.100
Slip 1	2.500	2.500	0.100

(b)

Figure 24 – Data of the main parameters used in the inverse analysis for C15LB90 series: a) Data file, b) FBL interface.

It is important to note that the results determined from the experimental program relative to the evaluated specimen series must be introduced into the software for comparison with the numerical results, as shown in Figure 25. The software cannot run without this data.

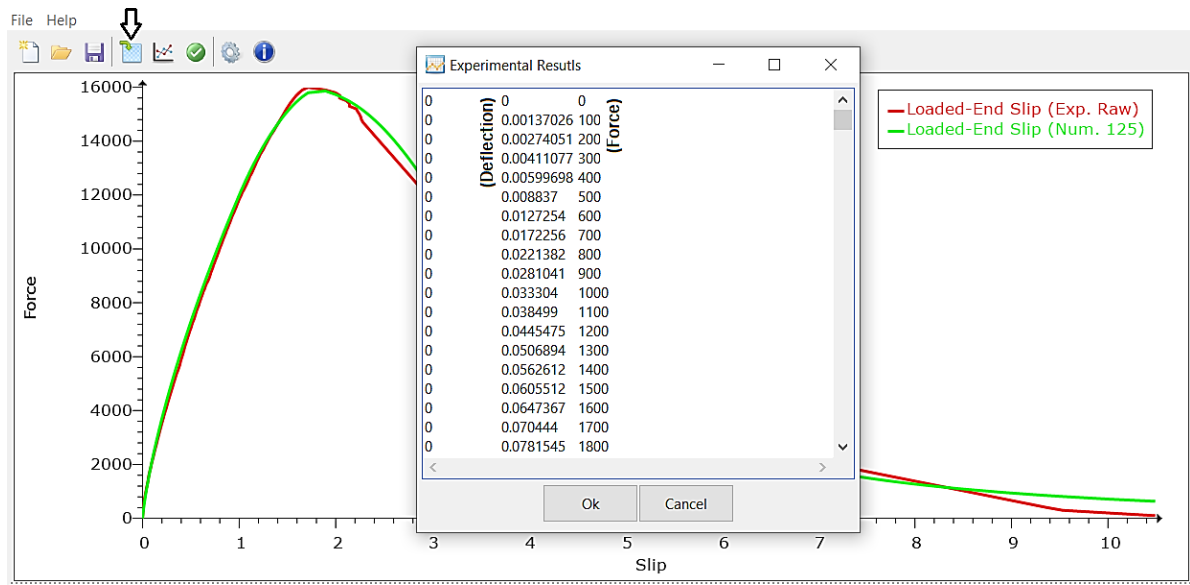


Figure 25 – Introduction of the experimental results of  $F - \delta$  in the inverse analysis for C15LB90 series.

The final step for the inverse analysis in FBL is to run the analysis considering that the introduced parameters of the Bond-slip relationship will generate  $F - \delta$  curves at the loaded or free ends of the specimen's series and the respective local bond-slip law. With the visualization of those curves the values of the imputed parameters need to be adjusted in order to fit the numerical curves (illustrated in green) with the experimental curves (illustrated in red).

Figure 26 shows the comparison between numerical and experimental results in the context of pullout force-slip at the loaded end for C15LB90 series displayed in the FBL software window after running the analysis. It is possible to directly analyse the above-mentioned comparison, the error,  $e$ , and the determined local bond slip law. For the visualization of the local bond law of the evaluated series in FBL the user must press "Plot", see Figure 27.



Note that Figure 26 presents both numerical (NUM) and experimental (EXP) results in relation to  $F - \delta$  at the loaded end.

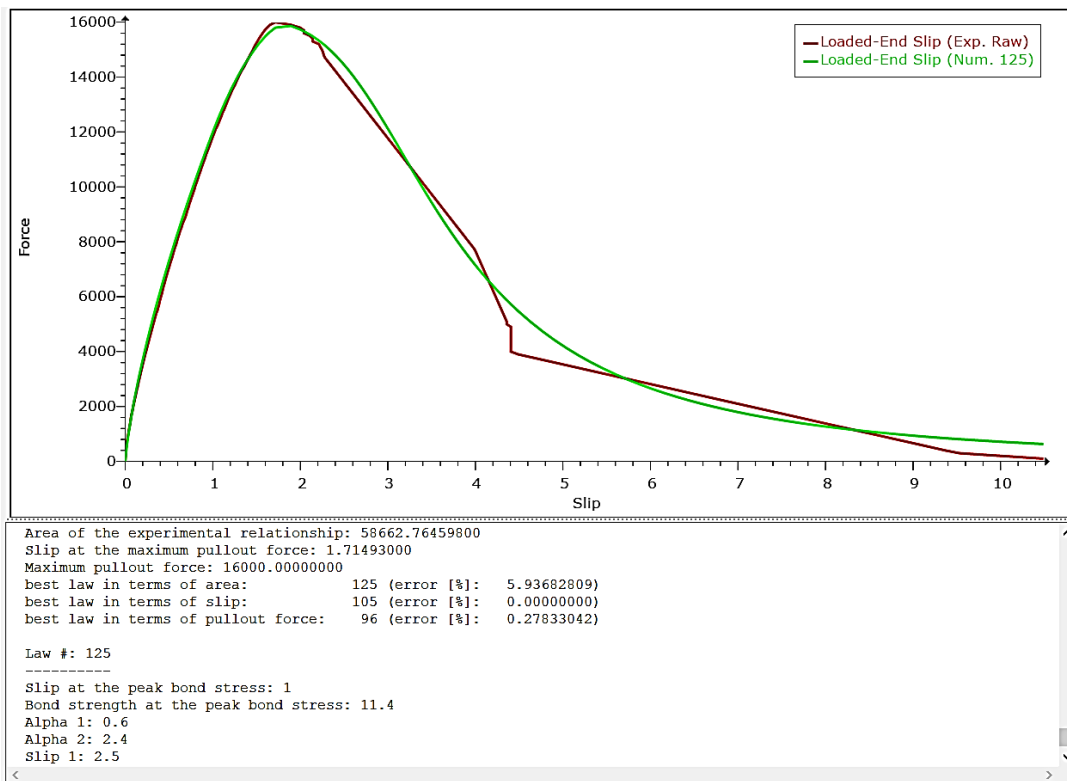


Figure 26 – Calibration between theoretical and experimental  $F - \delta$  curves for C15LB90 series in FBL.

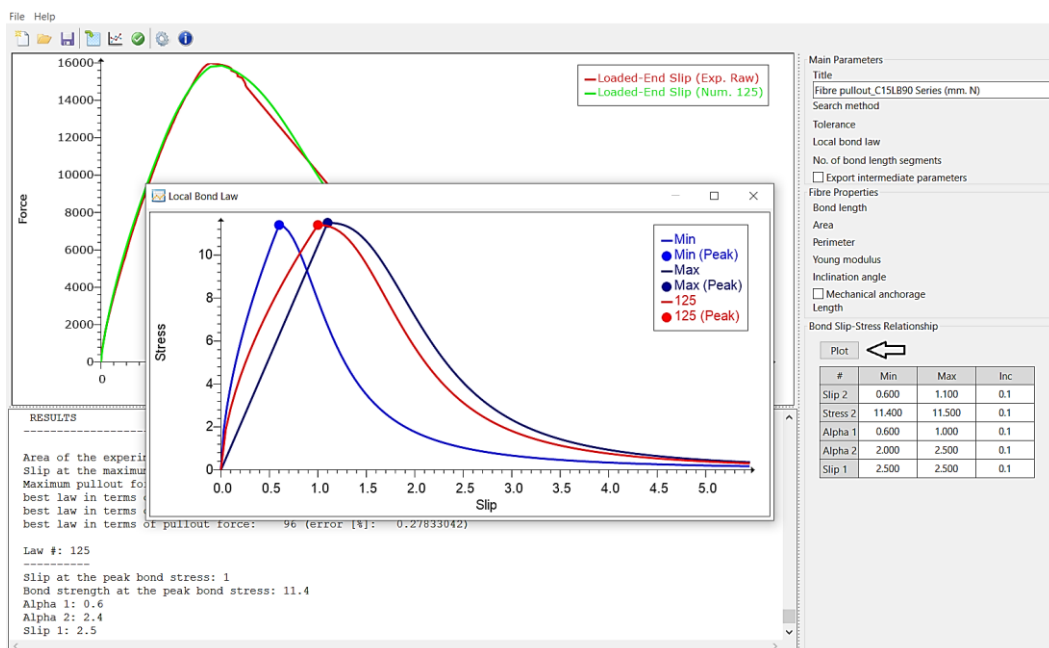


Figure 27 – Local Bond Law for C15LB90 series determined by inverse analysis.

The same inverse analysis strategy was conducted for all series of the experimental programme. Figure 28 show the comparison between numerical and experimental results of pullout force *versus* loaded end slip.

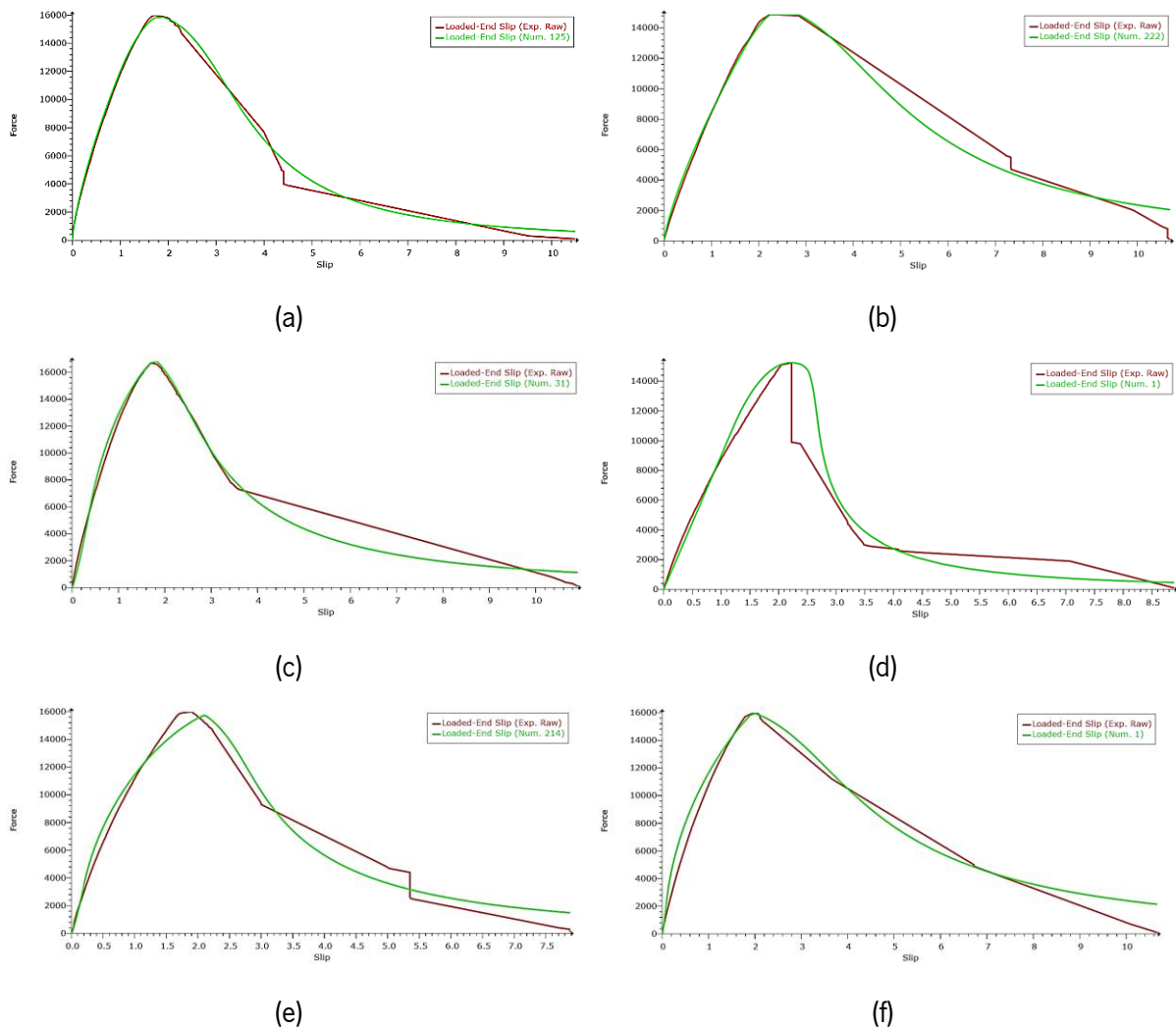


Figure 28 – Calibration between theoretical and experimental  $F - \delta$  curves for series: a) C15LB90, b) C25LB90, c) C15LB140, d) C25LB140, e) C15LB200, f) C25LB200.

Through the analysis of the graphs presented in Figure 28 it is evident that the proposed method is capable of simulating with good accuracy the pullout force *versus* loaded end slip for all specimen series tested. Only the slip corresponding to the maximum bond stress of C25LB90 series is higher comparing to the  $S_m$  obtained experimentally.

The respective bond-law of each series captured from FBL is depicted in Figure 29.

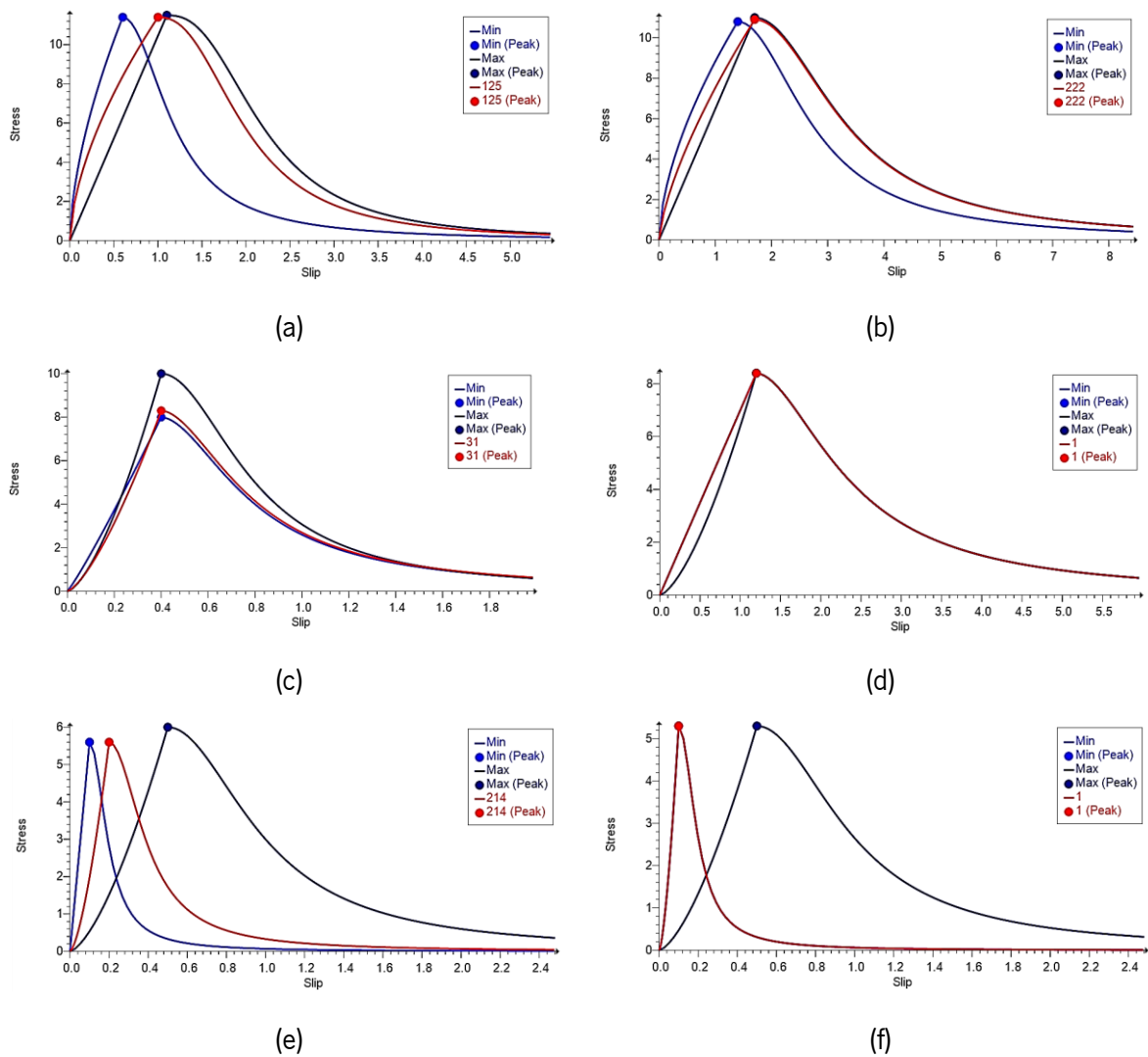


Figure 29 – Local bond law for series: a) C15LB90, b) C25LB90, c) C15LB140, d) C25LB140, e) C15LB200, f) C25LB200.

The curves representing the stress-slip relationship are presented in 3 different colour, light blue, red and dark blue. The parameters defining the bond stress-slip relationship were imposed using FBL in a range of values from minimum to maximum with an increment so that the local-bond law could be determined. The light blue and dark blue curves represent the minimum and maximum parameter values set in the software, and the red curve represents the bond-slip law determined between those values. Figure 24 presented previously shows the range of parameters values imposed in FBL for C15LB90 series, which lead to the respective local-bond law curves in Figure 29.

In the above presented curves, the bond strength for each series is represented with a number that relates to the best numerical law obtained from the exhaustive search that best fits the numerical and experimental envelop of pullout force vs slip at loaded end (minimum error,  $e$ ).

Table 5 shows the parameters determined from the inverse analysis for each series in relation to the bond-slip law and the error obtained in each exhaustive search.

Table 5 – Parameters of the bond model obtained from the inverse analysis in FBL

Series configuration				Results of Bond Law from FBL					
Series	Bar diameter (mm)	Concrete cover (mm)	Anchorage length (mm)	$\tau_m$ (Mpa)	$S_m$ (mm)	$S_0$ (mm)	$\alpha$	$\beta$	error (%)
C15LB90	5	15	90	11,4	1	2,5	0,6	2,4	5,9
C15LB140		15	140	8,3	0,4	2,3	1,4	1,8	12,7
C15LB200		15	200	5,6	0,2	2,3	1,5	2	12,7
C25LB90		25	90	10,9	1,7	3,5	0,7	2	7,4
C25LB140		25	140	8,4	1,2	1	1	1,8	20,6
C25LB200		25	200	5,3	0,1	4	1,5	2	9,3

From Table 5 can be pointed that the error in each series is acceptable, only in C25LB140 series the error is higher than desired because the decay of bond stress transference in the post-peak phase was accentuated and the calibration of parameter  $\beta$  was difficult to achieve.

As expected, the peak bond stress  $\tau_m$  decreased with the increase of anchorage length  $L_b$ , the slip at bond strength decreased with the increase of anchorage length and the different concrete cover thicknesses does not influence the maximum bond shear stress.

#### 4.1.2 Numerical simulation of the pullout bending tests and predictive performance of the proposed bond model

The main goal of this section was to simulate numerically the pullout bending tests of the experimental program described in Chapter 3 and calibrate the FEM model based on the average experimental pullout load-slip curves. Similar to the previous section the parameters of the defined local bond-slip relationships were determined by inverse analysis. Also, the predictive performance of the proposed method is assessed.

The first step to simulate numerically the pullout bending test was the creation of a finite element mesh adapted to the geometry of the specimen analysed in the experimental program. Only one block (the one with variable bond length) was considered in the FE model, due to the test setup symmetry.

The SFRSCC block was modelled using 4-node plain stress finite elements, Figure 30a, with a Gauss-Legendre integration scheme of 2x2. The steel hinge was modelled using 4-node plain stress finite elements, Figure 30a with 2x2 Gauss-Legendre integration scheme. To simulate the GFRP bar embedded in the concrete a linear elastic stress-strain relationship was assumed and the reinforcement was discretized by 2 node Frame 2D elements, Figure 30b. The interface finite elements used to simulate the bond behaviour between GFRP bars and surrounding SFRSCC were modelled by 4-nodes-2D-interface elements (two from the GFRP bar and two from the surrounding concrete) with 2 Gauss-Legendre integration points, as shown in Figure 30c.

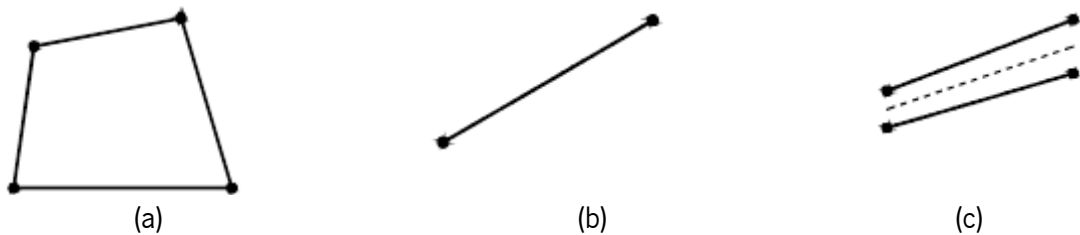


Figure 30 – Types of finite elements used in the FEM model: a) Lagrangian 4-node elements, b) Linear 2-node elements, c) Linear 4-node elements [8].

A tri-linear tensile-softening diagram was used to simulate the nonlinear material behaviour of SFRSCC in FEMIX, see Figure 31. This behaviour is implemented in FEMIX as NLMM\_104 constitutive model. The values of the parameters of the constitutive model for SFRSCC are summarized in Table 6.

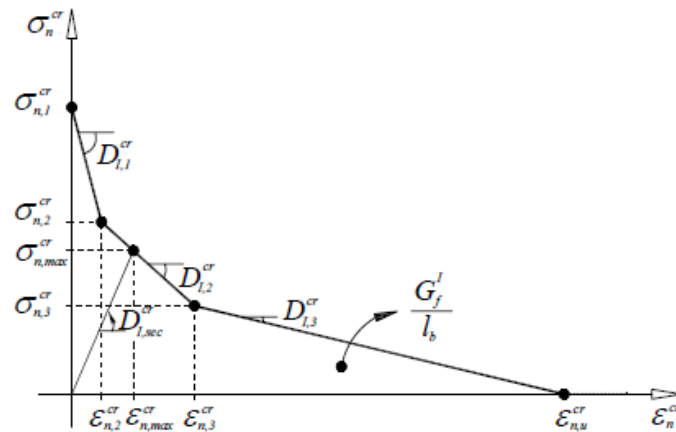


Figure 31 – Trilinear stress-strain diagram to simulate the fracture mode I crack propagation [34].

Table 6 – Values of the parameters of SFRSCC constitutive model used in pullout bending test simulation.

Parameter	Values (SFRSCC)
Poisson's ratio	$\nu = 0,2$
Young's modulus	$E_f = 27000 \text{ MPa}$
Compressive strength	$f_c = 50 \text{ MPa}$
Average tensile strength	$f_{ctm} = 2,9 \text{ MPa}$
Trilinear stress-strain diagram	$G_f^l = 4,187 \text{ N/mm}$
	$\xi_1 = 0,09 \quad \alpha_1 = 1,293$
	$\xi_2 = 0,393 \quad \alpha_2 = 0,579$
Maximum number of cracks per integration point	$p=2$
Crack bandwidth	<i>Square root of the area of the finite element</i>
Threshold angle	$\alpha_{th} = 30^\circ$

$$\sigma_{n,1}^{cr} = f_{ct} \quad \alpha_1 = \sigma_{n,2}^{cr} / \sigma_{n,1}^{cr} \quad \alpha_2 = \sigma_{n,3}^{cr} / \sigma_{n,1}^{cr} \quad \xi_1 = \xi_{n,2}^{cr} / \xi_{n,u}^{cr} \quad \xi_2 = \xi_{n,3}^{cr} / \xi_{n,u}^{cr}$$

Regarding the Glass Fibre Reinforced Polymer, the linear elastic stress-strain relationship assumed in the FEM model is presented in Figure 32 and the material properties are summarized in Table 7.

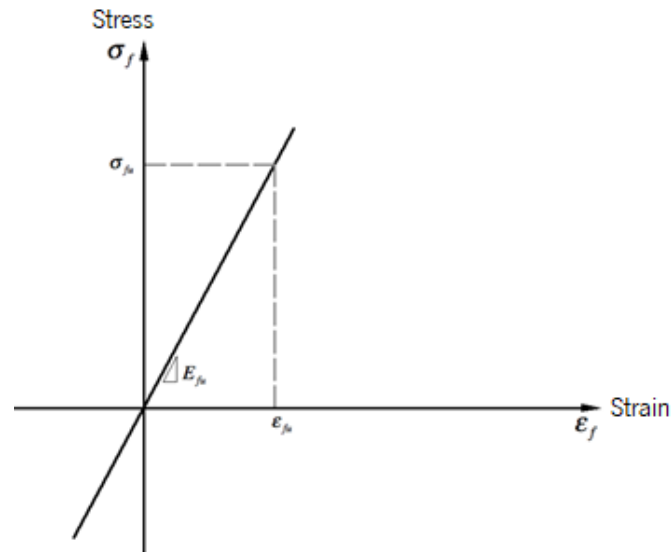


Figure 32 – Linear material behaviour of GFRP bars.

Table 7 – Values of GFRP material properties.

Mass per unit volume ( $\gamma$ ) ( $kN/m^3$ )	Young's modulus ( $E_f$ ) ( $MPa$ )	Poisson's ratio ( $\nu$ )	Ultimate tensile strength ( $\sigma_{fu}$ ) ( $MPa$ )
22,3	45000	0,15	945,56

The interface finite elements were numerically simulated with the NLMM301 constitutive model. This numerical model defines the bond-slip laws for each evaluated series in the pullout tests. The properties of this constitutive model are similar to those of the analytical model (NLML103) used in the previous section, see Figure 20. Since a 2D simulation was performed in this study, the interface was applied with a constant thickness equal to the perimeter of the GFRP bar.

In the finite element mesh was placed a pinned support (restrained in x and y) 50 mm from the left side of the block and two roller supports (restrained in x and z) in the symmetry axle of the block. Figure 33 shows the finite element mesh employed to simulate the behaviour between GFRP and SFRSCC in relation to pullout force *versus* slip at loaded end.

An incremental loading procedure with the arc length technique was used to improve the performance of the numerical simulation and avoid the instability in the convergence of the incremental/iterative process. For that, one-point vertical load was placed 50 mm from the symmetry axle of the specimen.

All the geometric and mechanical parameters presented were determined from the experimental program carried out on materials employed in the pullout bending tests reported in Chapter 3.

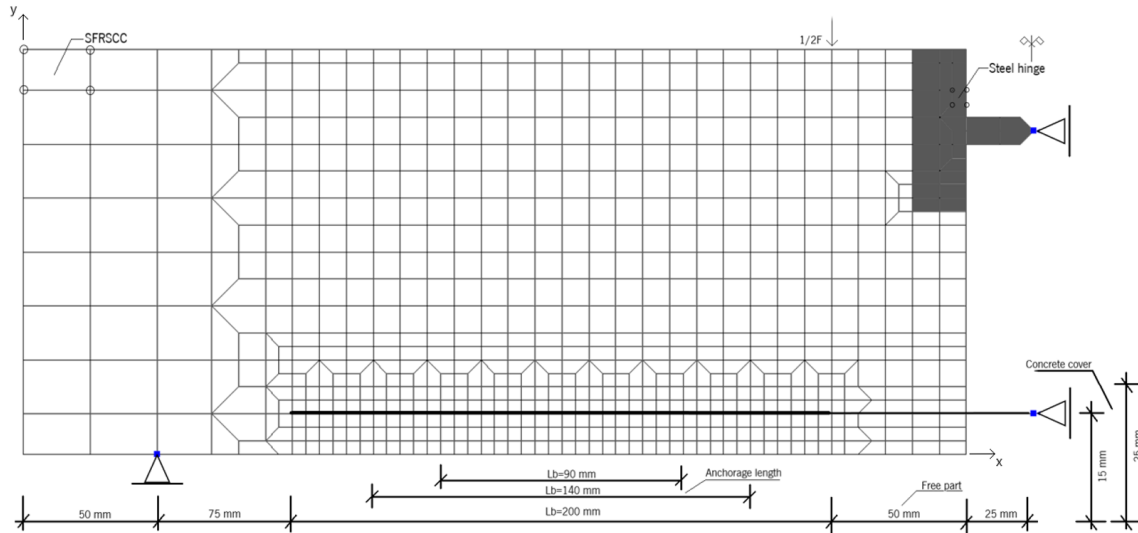


Figure 33 – Finite element model assembled to simulate pullout bending tests.

After creating the finite element mesh the parameters of bond-slip law for each numerical simulation were determined. Those values were found by applying the parameters of the bond-slip law obtained in section 4.1.1 and then performing the exhaustive search that led to the best fit of the numerical curves with the experimental envelop in terms of pullout force and the corresponding slip at the loaded end section of the tested specimen

The Newton-Raphson method was used to solve the nonlinear system of equations with an incremental/iterative procedure of displacement control with the arc-length technique. This iterative process uses a constant load increment ( $\Delta F$ ) and a predefined displacement increment ( $\Delta a$ ) up to a certain combination is reached, leading to the solution of the numerical simulation.

Figure 34 exhibits the bond-slip relationships between numerical and experimental results determined from FEMIX inverse analysis for each series.



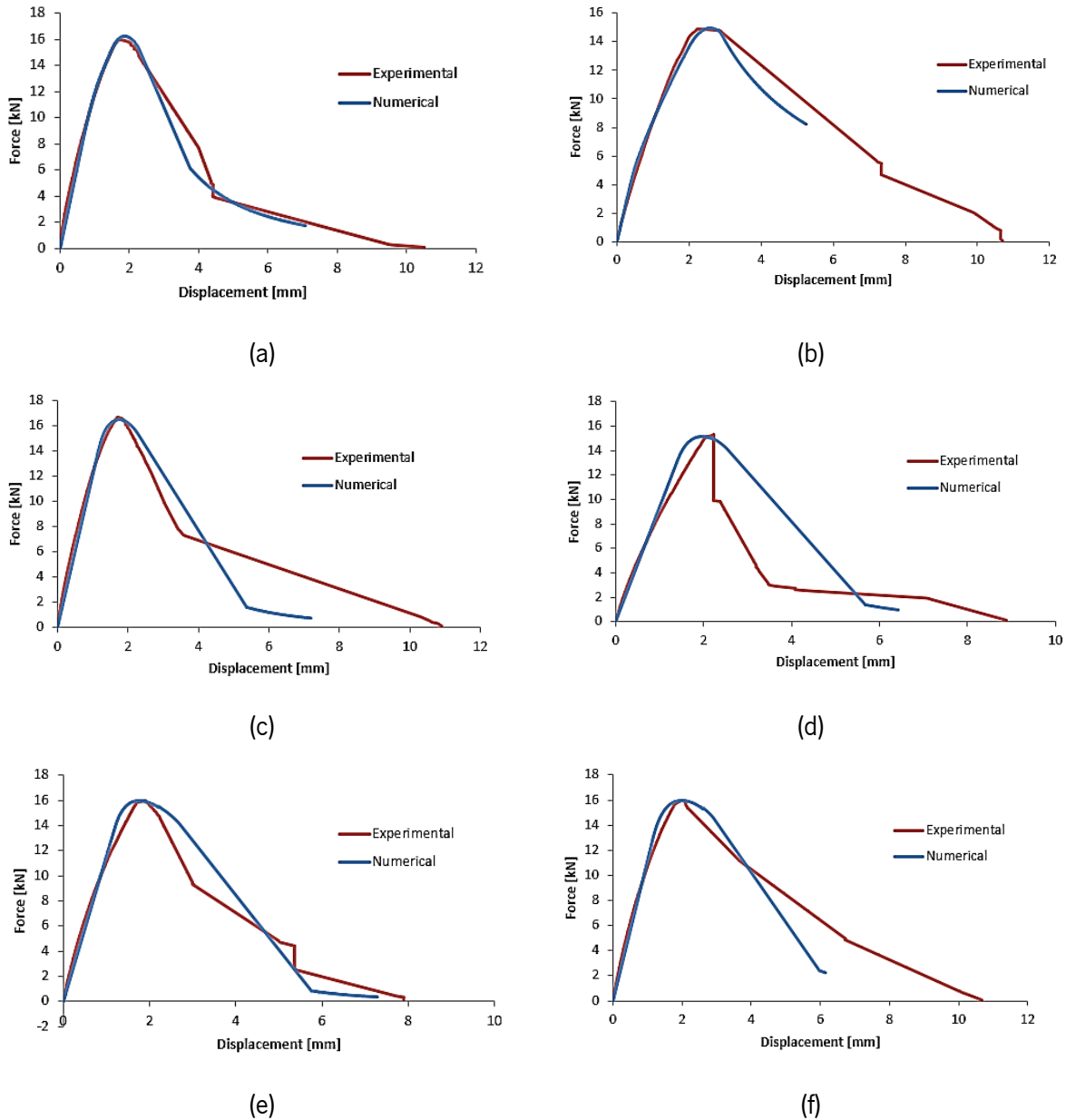


Figure 34 – Bond-slip relationships calibrated using FEMIX for series: a) C15LB90, b) C25LB90, c) C15LB140, d) C25LB140, e) C15LB200, f) C25LB200.

From the analysis of Figure 34 is evident that the FE model predicts fairly in an acceptable way the experimental  $F - \delta$  curves at loaded end registered numerically, especially the solutions in the pre-peak linear branch.

Table 8 shows the calibrated parameters of bond law for pullout bending tests determined in FEMIX inverse analysis.

Table 8 – Parameters of the bond model obtained from the inverse analysis in FEMIX.

Series configuration				Results of Bond Law from FEMIX				
Series	Bar diameter (mm)	Concrete cover (mm)	Anchorage length (mm)	$\tau_m$ (Mpa)	$S_m$ (mm)	$S_0$ (mm)	$\alpha$	$\beta$
C15LB90	5	15	90	15,5	2,2	1	0,6	2
C15LB140		15	140	12,4	2	1	1	2,7
C15LB200		15	200	9,4	2,4	0,5	1	3,9
C25LB90		25	90	15,1	2,7	0,5	0,7	1
C25LB140		25	140	12,3	2,3	0,5	1	3
C25LB200		25	200	10	2,4	0,5	1	2,5

As concluded in the experimental program and the previous section, the numerical analysis shows that different SFRSCC cover thickness (15 mm or 25 mm) does not influence the maximum bond shear stress in the tested series.

The parameter  $S_0$  represents the slip corresponding to the end of the linear phase of the local bond relationship and is only a small component of all the pullout force-slip relationship. Table 5 shows some variation in the values of  $S_0$ , but in Table 8 the values for this parameter are almost unaffected by the two variable properties considered in this study (SFRSCC cover thickness and anchorage length).

As expected, the peak bond stress  $\tau_m$  decreased with the increase of anchorage length  $L_b$ , which was a consequence of the nonlinear distribution of the bond stress along  $L_b$  [6].

The maximum slip  $S_m$  corresponding to the bond strength defines the limit between the hardening and the softening phases of the bond-slip law which significantly influences the bond-slip relationship. In the inverse analysis where FBL was used,  $S_m$  values were smaller for series with bigger GFRP anchorage length and higher for series with a bigger concrete cover. The same conclusion on  $S_m$  the parameter was confirmed in the inverse analysis using the finite element model.

Parameter  $\alpha$  defines the shape of the pre-peak branch and according to the above presented results the value was around 1 (pre-peak linear branch).

The values of  $\beta$  controlled the bond behaviour in the descending branch and ranged from 1 to 3.9 depending on the decay of bond stress transference.

Both the analytical and numerical methods predicted the experimental results quite accurately.



## Chapter 5

### 5. Numerical Modelling of Shallow beams

The present chapter is dedicated to the numerical modelling of shallow beams based on previous experimental work carried out by Fonseca, [35], which investigated the bending and shear behaviour of laminar structures in high-performance steel fibre reinforced concrete (HPSFRC). The main objective of the numerical modelling was to determine the constitutive model of the intervening materials in the tests (concrete, steel and Glass fibre reinforced polymer (GFRP)) in order to assure accurate numerical simulations of the bending tests.

The importance of assessing the numerical model in this section is by means essential for further use throughout this dissertation, especially in the numerical modelling of I beams in next chapter, where the same constitutive laws of the materials determined in this chapter were adopted.

The chapter begins with the presentation of the experimental program described in the reference work, [35], as well as an analysis of the main results. The constitutive model of the intervening materials is then described, and the methodology that leads to the validation of the numerical simulations is presented.

Additionally to the numerical simulations related to the experimental tests, another two simulations using glass fibre reinforced polymer (GFRP) and post-tension steel wires were carried out for comparing different reinforcement solutions.

Is important to point out that for the numerical modelling and the Finite Element analysis the software GID and FEMIX were used, respectively.

#### 5.1. Experimental program

Fonseca [35] performed a series of tests to assess the steel fibre reinforcement effectiveness for shallow structural elements failing in bending and shear. In this section only the behaviour of reinforced concrete elements failing in bending is presented and studied.

The experimental program consisted of carrying out a four-point notched beam bending test (4PNBBT) on three series of slab strips. Each one had a shear span equal to 450 mm, a total length of 1600 mm, a distance between supports of 1350 mm and a cross-section of 350 x 150 mm, see Figure 35. Each series of shallow beams were reinforced differently, the series with the designation A were reinforced longitudinally with  $3\Phi 6$  ( $\rho=0.2$ ), series with the designation B with  $3\Phi 8$  ( $\rho=0.36$ ) and series C with  $3\Phi 10$  ( $\rho=0.56$ ). In the top part of the cross-section of all tested slab strips, three steel bars of 6 mm diameter were used. Twelve slabs were tested for comparison purposes regarding the effectiveness of steel fibre reinforcement: six reinforced with steel fibres and the other six without steel fibres.



Figure 35 – Geometry, support and load conditions of the tested shallow beams including the monitoring system [35].

The mix composition used to manufacture the SFRSCC included  $45 \text{ kg/m}^3$  of hooked-end steel fibres. The materials used in the mix composition were cement (C) labelled as CEM I 52.5 R (rapid hardening and high strength cement, according to EN197-1:2000), limestone filler MICRO 100 AB (LF), a superplasticizer (SP) with the trade name SIKA 3002 HE, water (W), four types of aggregates (fine and coarse river sand, FS and CS; crushed calcareous of 6 to 14 mm size, CG\_1; crushed calcareous of 14 to 20 mm, CG\_2), and hooked ends steel fibres (SF) with a length ( $l_f$ ) of 60 mm, a diameter ( $\phi_f$ ) of 0.75 mm, aspect ratio ( $l_f/\phi_f$ ) of 80 and yield stress of 1100 MPa, see Table 9.

For the slab strips reinforced with conventional steel bars, the self-compacting concrete mix (SCC) was similar to the mix composition used for the SFRC slab strips except that the former ones did not include fibres. The SCC mix composition is also presented in Table 9.

Both concrete compositions showed good homogeneity and cohesion, no sign of segregation was detected, and the self-compacting requirements were assured. The total spread ( $d_f$ ), the time to reach

a spread diameter of 500 mm ( $T_{50}$ ), and the blocking ratio parameter ( $H_2/H_1$ ) of the L Box test (EFNARC 2002) were measured, see Table 9.

Table 9 – Composition of SFRSCC and SCC used on slab strips (per  $m^3$  of concrete).

Composition	SCC	SFRSCC
Cement (CEM I 52.5 R) ( $kg$ )	380.5	380.5
Water ( $dm^3$ )	102.7	102.7
Limestone filler (MICRO 100 AB) ( $kg$ )	360.0	360.0
Superplasticiser (SIKA 3002 HE) ( $dm^3$ )	12.5	12.5
Fine river sand ( $kg$ )	391.4	391.4
Coarse river sand ( $kg$ )	429.1	429.1
Crushed calcareous CG_1 (6 – 14 mm)	336.9	336.9
Crushed calcareous CG_2 (14 – 20 mm)	298.2	298.2
Hooked end steel fibres ( $kg$ )	0	45.0
$d_f$ (mm)	700	710
$T_{50}$ (s)	12	16
$H_2/H_1$	0.80	0.77

The slab strips were subjected to four-line loading points distributed in the width of the slab section, as shown in Figure 35, and the load was registered by a load cell of 300 kN maximum capacity, while the deflections were measured using five LVDT's. The tests were performed with servo-controlled equipment, imposing a deflection ratio of  $30 \mu m/s$  in the central LVDT for test control purposes.

To differentiate and identify the tested slab strips the label “Li\_j\_k” was used. The first symbol of the label denoted as “L” represented the series that the slab strips pertain to and can be replaced by A, B or C. The second symbol “i” identified the number of the slab strip test in each series (note that two slab strips were tested per each series). The symbol “j” represented the diameter of the steel bars used as tensile longitudinal reinforcement and “k” identified the number of applied fibres in the concrete mix (value in  $kg/m^3$ ).

For example, the label B1\_8\_45 corresponded to the first slab strip of “B” series reinforced with 8 mm diameter longitudinal steel bars and included 45  $kg$  of steel fibres per  $m^3$  of concrete.

The relationship between the measured deflection at the midspan and the applied force of the tested slab strips is depicted in Figure 36. Each curve represents the average load values at each deflection level, obtained from the two shallow beams of the corresponding series (A, B or C).

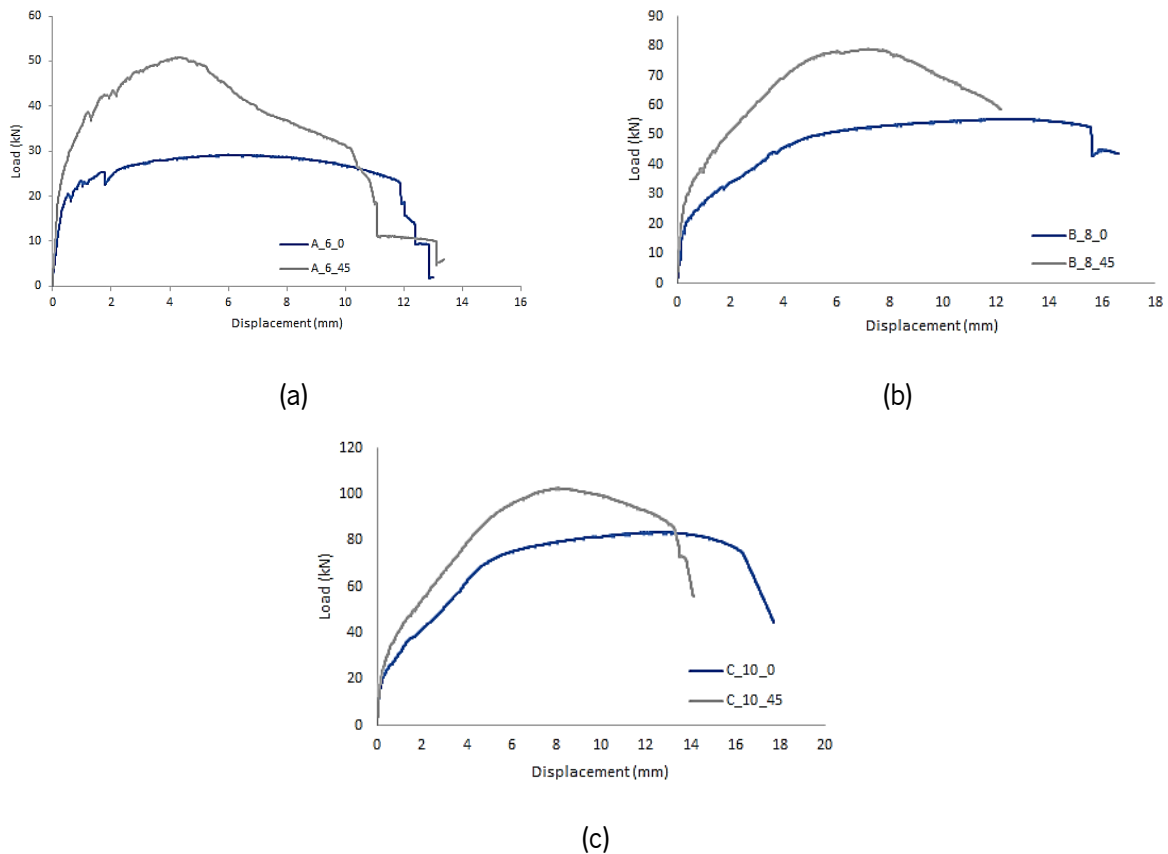


Figure 36 – Average force *versus* slip at midspan of series: (a) A\_6, (b) B\_8, (c) C\_10 [35].

From the analysis of Load-central deflection curves of the tested slab strips was observed that the load carrying capacity of the SFRSCC slab strips was higher than the corresponding SCC ones. The difference of the load carrying capacity between slabs reinforced with fibres and without fibres increased from the crack initiation up to the maximum load of the SFRSCC slab, however, that difference decreased with the increase of the percentage of longitudinal reinforcement.

Based on the analysis from the experimental study the contribution of the fibres for the slab load carrying capacity started from the very early stages of the slab deformation, shortly after the formation of incipient cracks and the resulting  $F - \delta$  curves showed that fibre reinforcement is highly effective for the design requirements imposed by the serviceability limit states, owing to its greater effectiveness the lower the percentage of longitudinal reinforcement ( $\rho$ ).

## 5.2. Numerical simulations using FEMIX-GID software

Through a numerical simulation of an experimental program, subsequent studies can be conducted, for example, the beam bending tests that determine the relationship between the applied force and the deflection at midspan. Thus, based on the experimental behaviour of a certain set of models, it is possible, in a faster and more economical way, to predict the behaviour of similar models by carrying out parametric studies that were not considered in the original experimental program.

For each series of shallow beams tested in the experimental program carried out by [35], finite element simulations were performed. The performance of the numerical model was appraised by tuning the parameters that define the Mode I crack constitutive law of the concrete used in the tests (SFRSCC and SCC) and the constitutive model of the steel.

In addition to the numerical simulation of all series of shallow beams using conventional steel reinforcement, another numerical simulation was performed by maintaining the same properties of the SFRSCC of the experimental program and reinforcing the slab with Glass fibre reinforced polymer (GFRP) defined Table 7 and two prestressing steel wires. This section also compares the results obtained by using this different approach to slab reinforcement with those obtained by conventional reinforcements, and a conclusion is drawn.

Gid software is a pre and postprocessor computer program for numerical simulations commonly used in science and engineering. This software allows the creation of the geometry of the numerical model, mesh generation and visualization of the analysis. When using FEMIX and GID, the last one creates the data file with the extension `_gl.dat` if the structure attributes and their finite element mesh are introduced, and then reads the results obtained in the post-processing carried out by Posfemix (FEMIX is divided in three software's: Prefemix, Femix and Posfemix), allowing the visualization of numerical results in a very straightforward and intuitive way.

In Figure 35 is depicted the geometry, support and load conditions of the tested shallow beams used in the numerical simulation. Is important to mention that three steel bars of 6 mm diameter were used in the top part of the cross section of all tested beams. Based on the symmetry of the structure, only half of the beam was considered in the modelling.

The numerical modelling started with the series flexural reinforced with 6 mm diameter longitudinal steel bars and without steel fibres in the self-compacting concrete (A\_6\_0). Firstly, was necessary to introduce

the data related to the shallow beams that define its geometry, such as the vertices of the beam and the intersection points between the faces of the beam and the longitudinal reinforcement.

The concrete and steel surfaces were created after the main points of the beam geometry had been defined, see Figure 37.

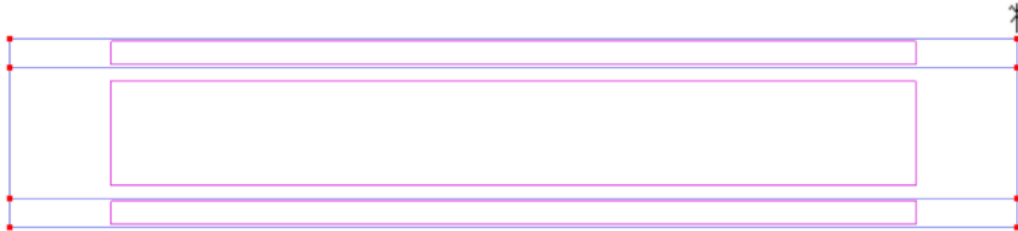


Figure 37 – Geometry of the beam used for the simulation of the A\_6\_0 series.

A poorly defined geometry of the structure or the information about the intervening materials around it will cause issues when creating the numerical mesh and the future analysis. This first phase is probably the most important for the numerical modelling.

After defining all the geometry of the beam and the layers that characterize each material, the next step was to create the finite element mesh with an intermediate level of refinement that thought to be acceptable based on a sensitivity analysis. From previous research is known that with an intermediate level of refinement of the mesh is achieved more effective results [36].

The concrete used in the beams was simulated by 8-node Serendipity plain stress finite elements with 2x2 Gauss-Legendre integration scheme, Figure 38, and quadratic 3-node Embedded cable 2D with 2 points Gauss-Legendre integration scheme was used to simulate the longitudinal reinforcements. Is important to note that the steel bars were assumed to be perfectly bonded and embedded into the surrounding concrete.



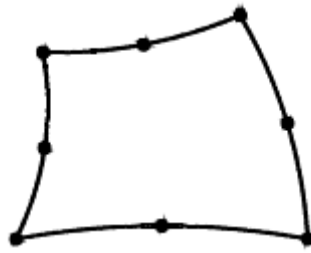


Figure 38 – Serendipity 8-node finite element [8].

The example of the created finite element mesh for shallow beams reinforced with 6 mm diameter longitudinal steel bars and without steel fibres in the self-compacting concrete (A\_6\_0) is depicted in Figure 39. After the creation of the mesh was necessary to introduce the information concerning the characteristics of the materials and the boundary conditions.

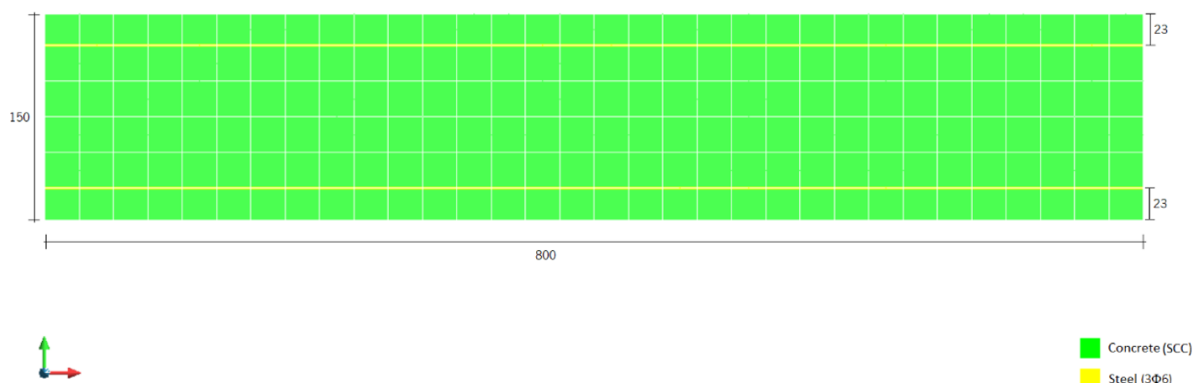


Figure 39 – Finite element mesh used for the simulation of A\_6\_0 series (dimensions in mm).

In this simulation was considered a roller support at the symmetry axle (restrained in x and z) of the beam and a pinned support (restrained in x and y) at 125 mm from the lateral side of the beam, as shown in Figure 40. Also, at 225 mm from the symmetry axle of the beam was placed a point load as indicated in the experimental test, Figure 41.

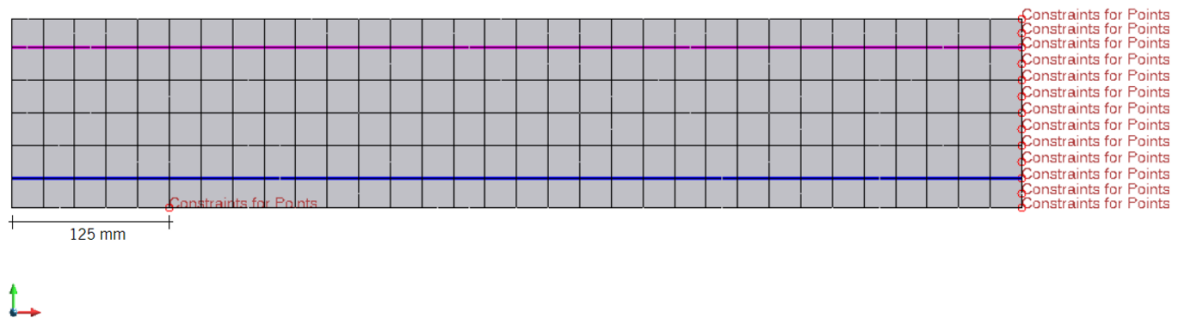


Figure 40 – Supports of the shallow beams.

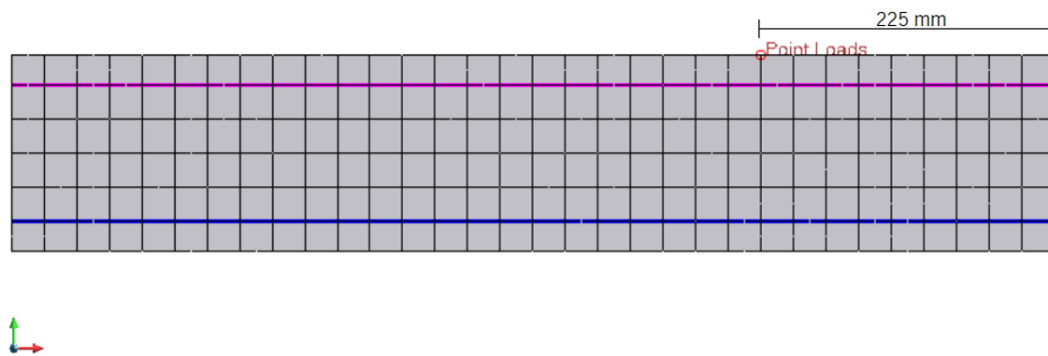


Figure 41 – Loads or prescribed displacements.

It was also necessary to characterize the concrete and the reinforcement in the tests. To simulate the post-cracking behaviour of the concrete, a quadrilinear tensile-softening diagram available in the software was used and the Fracture Mode I parameters were defined.

Table 10 presents the concrete properties used for the A\_6\_0 series numerical simulation. The constitutive model used for the simulation of the concrete behaviour was the NLMM104 which allowed enough flexibility to model the most significant aspects of the tension-softening effect.

Is important to note that only the Quadrilinear tensile-softening diagram was used for the A\_6\_0 series numerical simulation. In this case, it was difficult to assess the concrete model parameters by fitting the force vs deflection numerical and experimental curves. For all other simulations the trilinear tensile-softening diagram was used and the values of  $f_{ct}$ ,  $\xi_1$ ,  $\alpha_1$ ,  $\xi_2$ ,  $\alpha_2$  defined the fracture mode I properties.

Table 10 – Values of the parameters of the concrete constitutive model for L\_6\_0 series.

Parameter	Values (SCC)
Poisson's ratio	$\nu=0,2$
Young's modulus	$E_f = 37490,95 \text{ MPa}$
Compressive strength	$f_c = 86,34 \text{ MPa}$
Average tensile strength	$f_{ctm} = 3,4 \text{ MPa}$
	$G_f^I = 0,05 \text{ N/mm}$
Quadrilinear Tensile-softening diagram	$\xi_1 = 0,025$ $\alpha_1 = 0,3$
	$\xi_2 = 0,5$ $\alpha_2 = 0,3$
	$\xi_3 = 0,6$ $\alpha_3 = 0,3$
Maximum number of cracks per integration point	$p=2$
Parameter defining the mode I fracture energy available to the new crack	$p_1 = 1$
Crack band-width	<i>Square root of the area of the finite element</i>
Threshold angle	$\alpha_{th} = 30^\circ$

The graphical difference between the trilinear and quadrilinear tensile-softening diagrams is depicted in Figure 42.

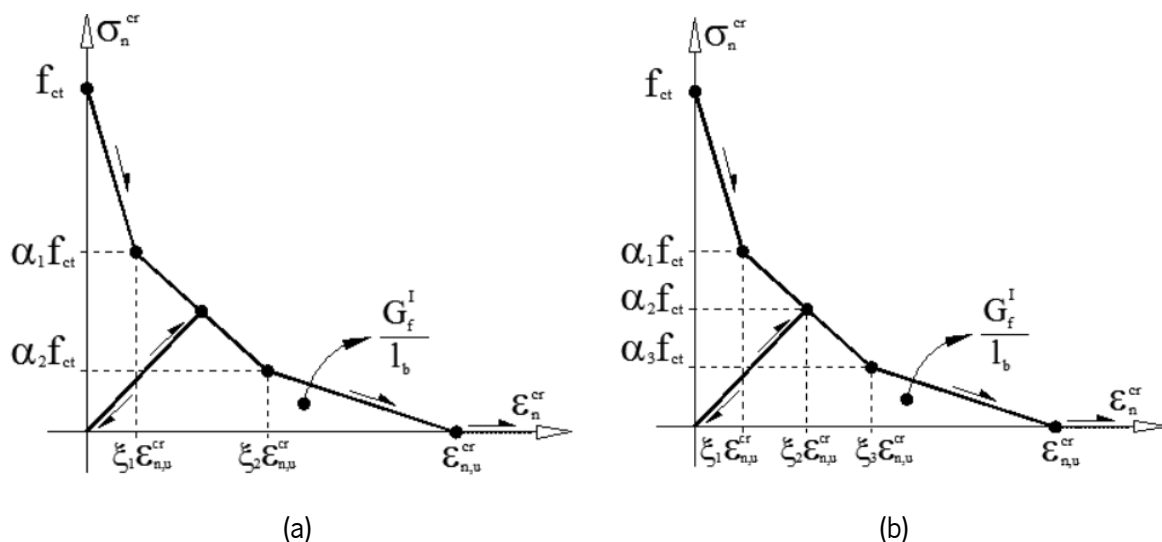


Figure 42 – Tensile-Softening diagrams used in GID: (a) Trilinear, (b) Quadrilinear.

The Concrete properties used in the numerical simulation of the B\_8\_0 and C\_10\_0 shallow beams series is presented in Table 11.

Table 11 – Values of the parameters of the concrete constitutive model for B\_8\_0 and C\_10\_0 series.

Parameter	Values (SCC)
Poisson's ratio	$\nu=0,2$
Young's modulus	$E_f = 37490,95 \text{ MPa}$
Compressive strength	$f_c = 86,34 \text{ MPa}$
Average tensile strength	$f_{ctm} = 3,4 \text{ MPa}$
	$G_f^I = 0,162 \text{ N/mm}$
Trilinear Tensile-softening diagram	$\xi_1 = 0,005$ $\alpha_1 = 0,2$ $\xi_2 = 0,3$ $\alpha_2 = 0,05$
Maximum number of cracks per integration point	$p=2$
Parameter defining the mode	$p_1 = 1$
Crack band-width	<i>Square root of the area of the finite element</i>
Threshold angle	$\alpha_{th} = 30^\circ$

Table 12 shows the concrete properties used in the numerical simulation of the B\_8\_45 and C\_10\_45 shallow beams series and Table 13 presents the values of the parameters used to define the constitutive model of conventional steel reinforcement. The constitutive model used for the simulation of the steel behaviour was the NLMM201, see Figure 43.

Table 12 – Values of the parameters of the concrete constitutive model for B\_8\_45 and C\_10\_45 series.

Parameter	Values (SFRSCC)
Poisson's ratio	$\nu=0,2$
Young's modulus	$E_f = 38184,5 \text{ MPa}$
Compressive strength	$f_c = 91,22 \text{ MPa}$
Average tensile strength	$f_{ctm} = 3,44 \text{ MPa}$
	$G_f^I = 1,0 \text{ N/mm}$
Trilinear Tensile-softening diagram	$\xi_1 = 0,005$ $\alpha_1 = 0,75$ $\xi_2 = 0,3$ $\alpha_2 = 0,085$
Maximum number of cracks per integration point	$p=2$
Parameter defining the mode	$p_1 = 1$
Crack band-width	<i>Square root of the area of the finite element</i>
Threshold angle	$\alpha_{th} = 30^\circ$

Table 13 – Values of the conventional steel constitutive model.

Diameter (mm)	$\xi_{sy}$	$\sigma_{sy}(MPa)$	$\xi_{sh}$	$\sigma_{sh}(MPa)$	$\xi_{su}$	$\sigma_{su}(MPa)$	Third branch exponent	Young's modulus (GPa)
6	0,00235	471,5	0,01	562,5	0,15	520		
8	0,0028	500	0,014	635	0,02	635	1	200
10	0,00275	550	0,008	600	0,012	625		

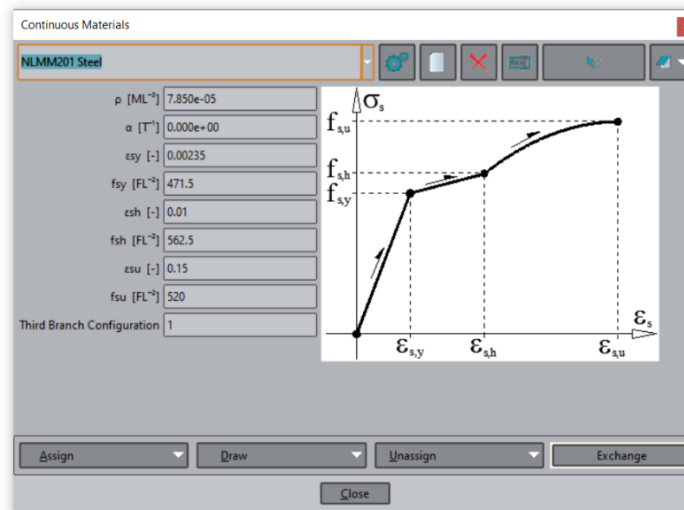


Figure 43 – Steel properties used in the simulation of the A\_6\_0 slab strip series.

The final step before performing the numerical simulation was the definition of the load cases and the combinations that better suited the experimental program. In all the numerical simulations the load was applied by direct displacement–control at the loaded point (Node number 653, degree of freedom Y) and the Newton-Raphson algorithm was used.

After going through all the steps described previously, the calculation of the structure behaviour was conducted through FEMIX. More detailed information about the steps of modelling using the software GID can be found in the APPENDIX.

The relationship between the applied force and the deflection at the mid-span obtained from the numerical simulations for all beam series are gathered in Figure 44, revealing that this model is validated and can assess, with enough accuracy, the behaviour of elements failing in bending. Furthermore, the proposed concrete and steel constitutive models are able to define the post-cracking behaviour of the tested beams.

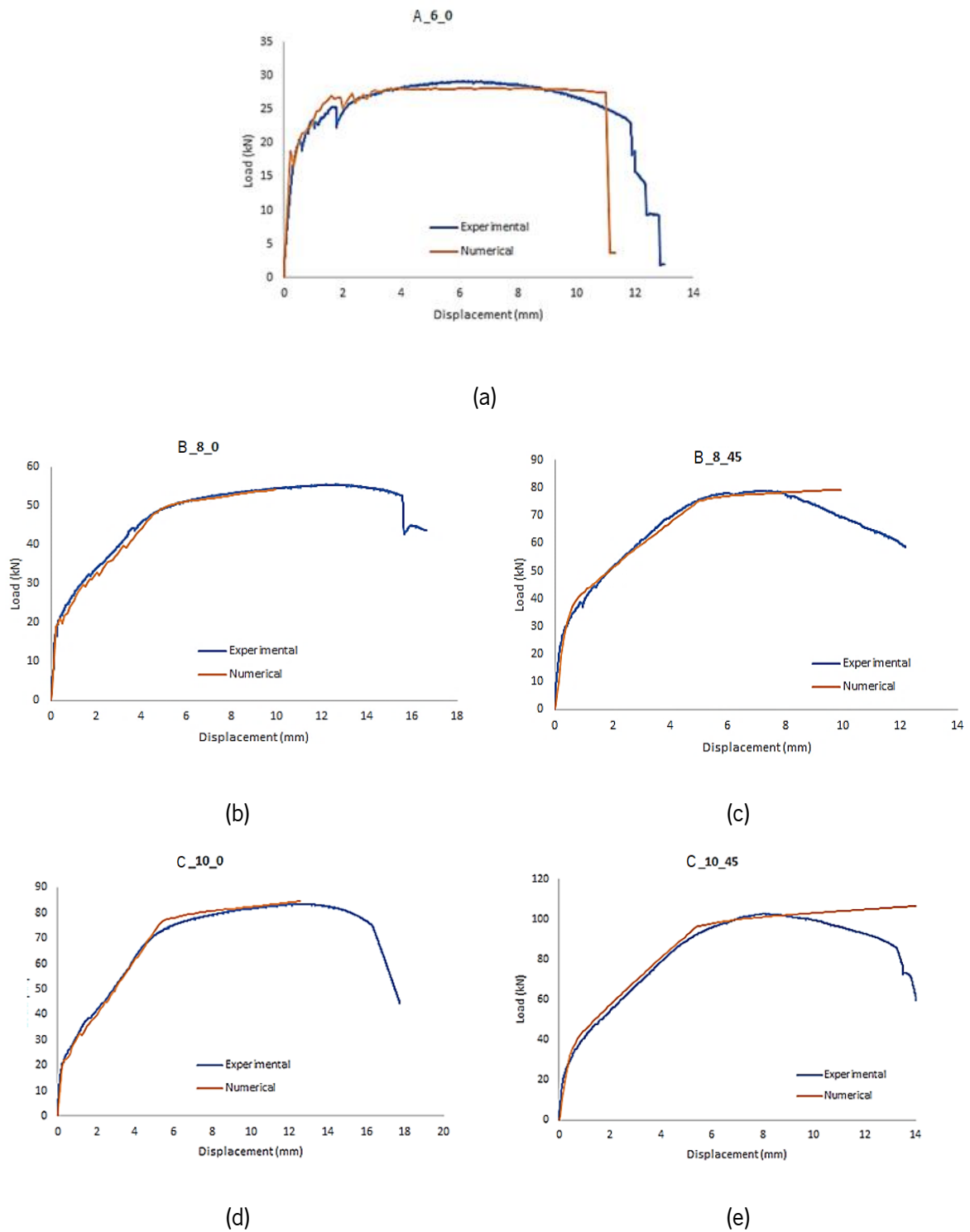


Figure 44 – Load vs. Deflection at mid-span obtained experimentally and numerically (assuming perfect bond) for the shallow beams series: (a) A\_6\_0, (b) B\_8\_0, (c) B\_8\_45, (d) C\_10\_0, (e) C\_10\_45.

### 5.2.1. Influence of reinforcing shallow beams with GFRP and prestressed steel wires

As mentioned before, the main aim of simulating the previous described shallow beams with different longitudinal reinforcement (GFRP and Prestressed steel wires) was to analyse the performance of this shallow beams failing in bending and compare the results of force vs deflection at mid-span of each simulation.

The beams were identified as B\_8\_45 \_Post Tensioning and C\_10\_45 \_Post Tensioning and were simulated numerically by using the same concrete constitutive model adopted for the simulation of B\_8\_45 and C\_10\_45 series, respectively, and using the fracture mode I tuned parameters, presented in Table 12. The values used for simulating the conventional steel behaviour is presented in Table 13.

In relation to the reinforcement in the FE mesh the prestressed steel wires and GFRP bars were simulated by 3-node Cable 2D elements with 2 Gauss-Legendre integration points.

The properties of the constitutive model used for simulating the behaviour of GFRP bars in the present analysis were the same obtained from the experimental program presented in Chapter 3, Table 7 provides detailed information.

In addition, for better comparison purposes the cross-section area of the GFRP bars ( $\Phi 5$ ) was approximated equal to the cross-section area of the flexural conventional steel reinforcement used in B\_8\_45 ( $3\Phi 8$ ) and C\_10\_45 ( $3\Phi 10$ ) series for each numerical simulation, respectively.

Regarding the prestressing purposes, two steel wires were used as flexural reinforcement of the beams along with the GFRP bars. The constitutive model used to simulate the behaviour of the steel wires is presented in Table 14.

Table 14 – Values of the parameters of the steel wires constitutive model.

Diameter (mm)	$\xi_{sy}$	$\sigma_{sy}(MPa)$	$\xi_{sh}$	$\sigma_{sh}(MPa)$	$\xi_{su}$	$\sigma_{su}(MPa)$	Third branch exponent	Young's modulus (GPa)
6	0,007991	1558,3	0,029	1664,15	0,05	1770	1	195

The prestress level of 75% of the steel wires yielding stress ( $f_{sy} = 1558.3 \text{ MPa}$ ) was adopted for the numerical simulation. Therefore, was necessary to estimate the correspondent temperature to the intended prestress. This logic is demonstrated by the following equations:

$$\sigma = E * \varepsilon \quad (27)$$

where E (MPa) is the Young's modulus and  $\varepsilon$  is the tensile strain.

The strain can also be written as:

$$\varepsilon = \frac{\Delta L}{L} = \frac{\alpha * \Delta T_u * L}{L} \quad (28)$$

Thus, replacing the Eq.(28) in Eq.(27) comes:

$$\sigma = E * \alpha * \Delta T_u \quad (29)$$

The uniform thermal load correspondent to the intended prestress was  $-600^\circ\text{C}$ . This negative thermal load applied to the steel wires implemented an upward deflection to the beams, meaning that the reinforcement is being contracted.

To better understand how the beams were simulated, Figure 45 and Figure 46 shows the GID graphic visualization of this elements and Figure 47 the respective beams cross section.





Figure 45 – GID graphic visualization of the assigned materials constitutive models in the B\_8\_45\_Post Tensioning beam.

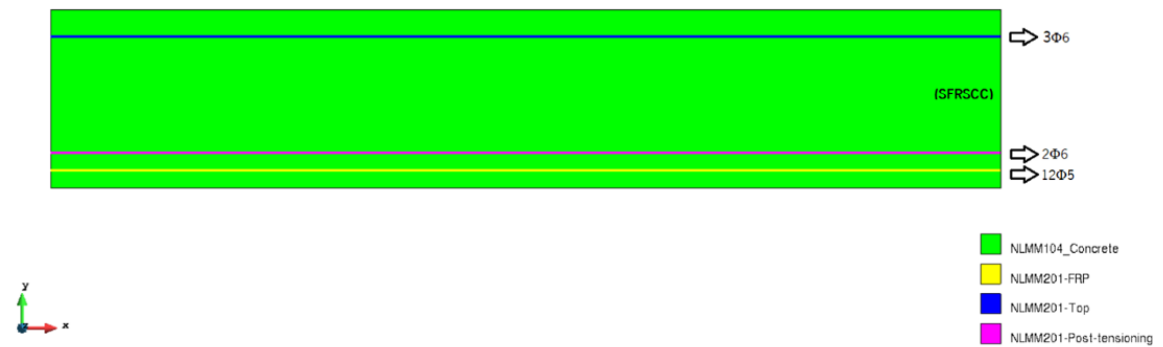


Figure 46 – GID graphic visualization of the assigned materials constitutive models in the C\_10\_45\_Post Tensioning beam.

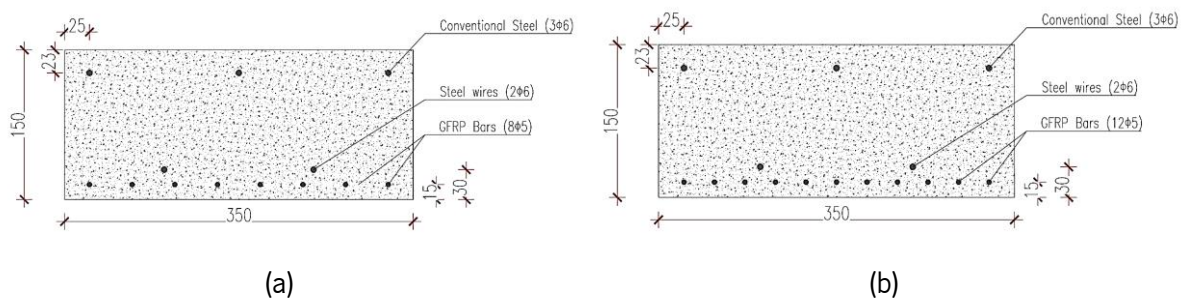


Figure 47 – Cross section of the numerically simulated beams: (a) B\_8\_45\_Post Tensioning, (b) C\_10\_45\_Post Tensioning.

The results of the numerical simulations performed with the B\_8\_45\_Post Tensioning and C\_10\_45\_Post Tensioning shallow beams, assuming perfect bond at the GFRP, steel wires and Conventional Steel-concrete interface, in relation to the applied load and the deflection at the mid-span is depicted in Figure 48.

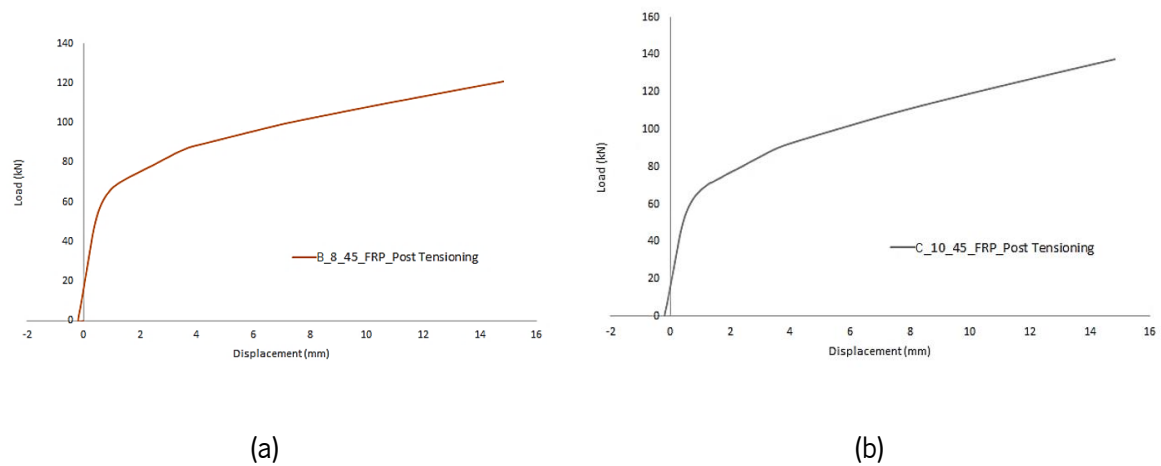


Figure 48 – Load *vs.* Deflection at mid-span obtained numerically (assuming perfect bond) for the beams: (a) B\_8\_45\_Post Tensioning, (b) C\_10\_45\_Post Tensioning.

Figure 49 shows the comparison of the numerical relationship between the  $F$  *vs*  $\delta$  at mid-span of the numerically simulated beams presented in the previous section with this hybrid system.

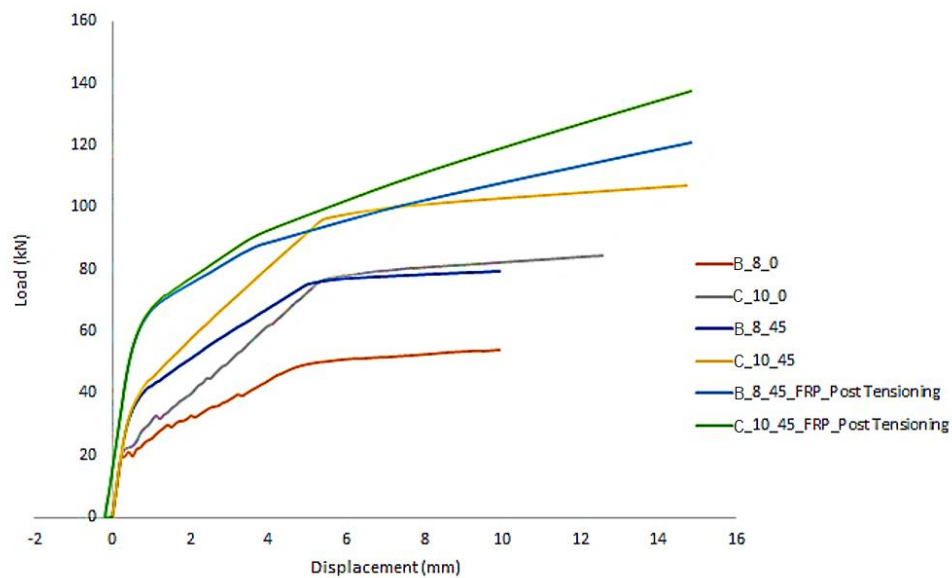


Figure 49 – Comparison between force deflection response of the developed numerical simulations.



The analysis of Figure 49 evidence that in the beams without steel fibres, after the peak, a constant or barely noticeable hardening phase follows, which is the typical behaviour of elements with only ordinary reinforcement since the failure mode depends on the steel. On the other hand, the beams reinforced with steel fibres show a softening phase after peak load because after the concrete cracks open, the ordinary reinforcement and steel fibres start working together with the steel fibres bridging the cracks. As a result, fibre reinforced beams show higher load carrying capacity and the energy dissipation decreases slowly.

The application of the GFRP bars and the two prestressed steel wires in the slab strips provided significant increase in the load carrying capacity (ultimate flexural capacity) at serviceability limit state conditions and at steel yield initiation. Greater benefits would be achieved if the prestress level was applied both to the GFRP bars and the steel wires, increasing the shear capacity of the beams.

This simple numerical strategy showed that the model was validated and the behaviour of shallow beams failing in bending was assessed.

## Chapter 6

### 6. Case Study of I-shaped cross-sectional beams for buildings

This chapter explores the potentialities of a new generation of structural systems through a hypothetical case study. This study is based on the design and numerical simulation using FEMIX program, of a 12 m long beam with I-shaped-cross-sectional and using the materials investigated in the previous chapters.

The proposed I beam is flexurally reinforced by prestressed glass fibre reinforced polymer (GFRP) and steel strand and made of Steel Fibre Reinforced Self-Compacting Concrete (SFRSCC) to suppress the steel stirrups. One characteristic of GFRP is its linear elastic behaviour which can lead to brittle failure of beams. In general, the opposite behaviour is expected by prestressing these elements which increases the beam's ductility. Moreover, aids to increase the shear capacity of the members and control the crack width.

The GFRP bars are immune to corrosion and can be positioned with a small concrete cover in the structure whereas the steel strand needs higher concrete cover to avoid corrosion. In case of fire occurrence, the steel strand assures the necessary flexural strengthening of the beams if GFRP bars become ineffective.

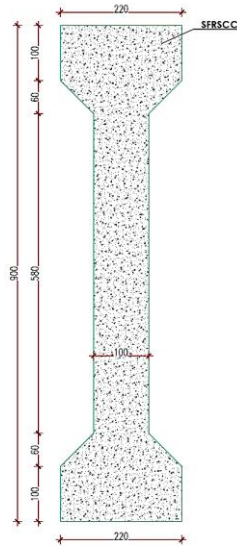
The numerical results obtained using the hybrid model will be compared to the results of two other developed models using different longitudinal reinforcements: the traditional steel reinforcement and only using GFRP reinforcement. For this purpose, the finite element mesh, load, support conditions and material properties used in the numerical simulation are described in detail.

Additionally, the influence of the GFRP-SFRSCC bond conditions on the force *versus* deflection at mid-span of SFRSCC I shaped cross-sectional beams reinforced only with GFRP is assessed by carrying out two simulations: assuming the bond-slip equation (23) with the parameters indicated in Table 8 for series C25LB200 and assuming perfect bond between the GFRP and the surrounding concrete.

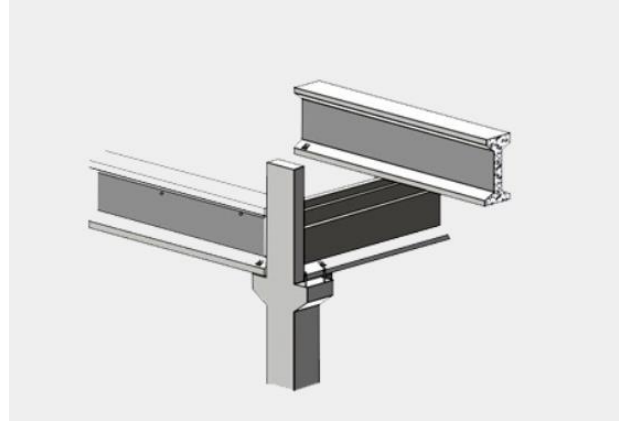
#### 6.1. Numerical Simulations

The hypothetical developed case study concerns the potential use of I-shaped-cross-sectional in different structures, but in this dissertation, the study focuses on the application in office buildings. Figure 50 and

Figure 51 shows the case study, the proposed structural application of the beam and its geometry, and few examples of its use in buildings.



(a)



(b)



(c)



(d)

Figure 50 – Proposed I beam and applications: (a) Geometry of the beam, (b) Example 1, (c) Example 2, (d) Example 3.

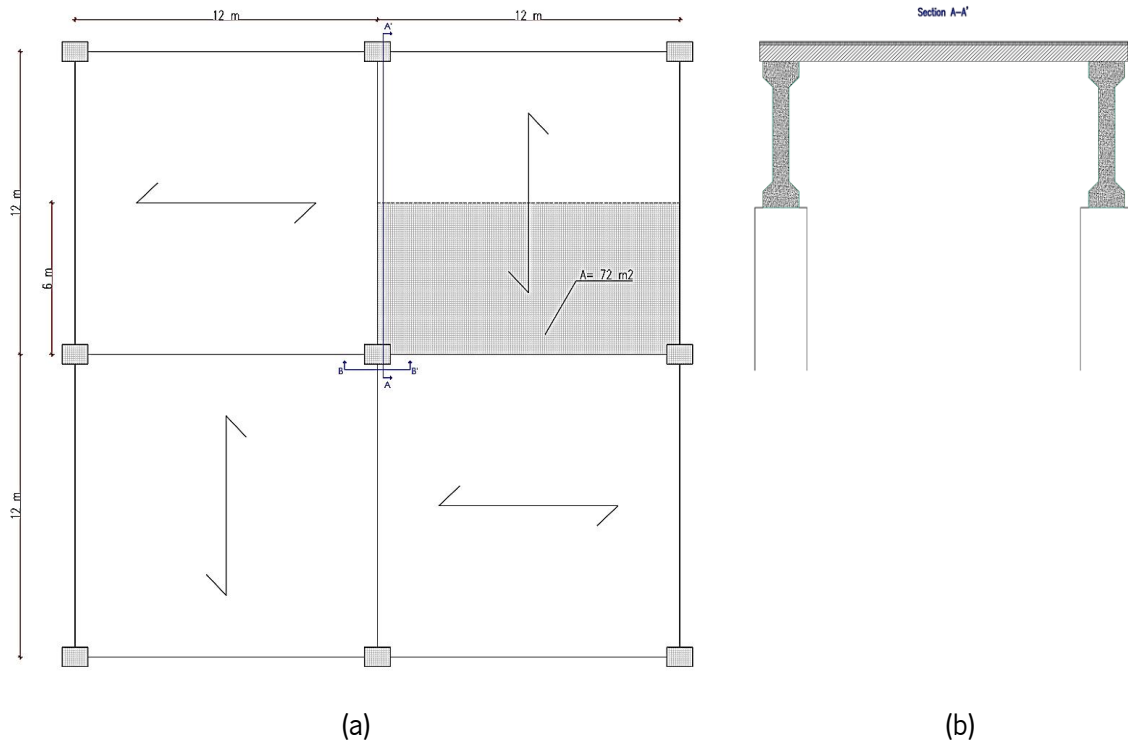


Figure 51 – Hypothetical case study: (a) Structural application of the beam, (b) Section A-A'.

The beam is subjected to different load cases and combinations. For the permanent load was considered the self-weight of the beam, the self-weight of a slab used in office buildings and the slab covering. For the live load was considered the uniformly distributed load for office buildings, see Table 15. Note that the beam was designed according to Eurocode 1, part 1-1 (Actions on structures/General Actions) and Eurocode 0 (Annex A1). Eurocode 1 recommends that uniformly distributed loads for office areas (Category B) range between  $2$  and  $3 \text{ kN/m}^2$ , Figure 52a, and Eurocode 0 (Annex A1) recommends the values of  $\psi$  factors for buildings, Figure 52b. The detailed beam design is given in the Annex B.

Table 15 – Combination of actions used in the beam design.

Combination of actions	Uniformly distributed load (kN/m)		Máx. Bending moment (kN.m)	
	Ultimate Limit States	Serviceability Limit States	Ultimate Limit States	Serviceability Limit States
Characteristic Load Combination	59,44	42,03	1069,92	756,54
Frequent Load Combination	45,94	-	826,92	-
Quasi-permanent Load Combination	40,54	29,43	729,73	529,74

Permanent Loads:  $g_{k,beam}=3,03 \text{ kN/m}$ ;  $g_{k,slab}=18 \text{ kN/m}$ ;  $g_{k,slab.covering}=3 \text{ kN/m}$

Live Loads:  $q_k = 18 \text{ kN/m}$

Table 6.2 - Imposed loads on floors, balconies and stairs in buildings

Categories of loaded areas	$q_k$ [kN/m <sup>2</sup> ]	$Q_k$ [kN]
<b>Category A</b>		
- Floors	1,5 to <u>2,0</u>	<u>2,0</u> to 3,0
- Stairs	<u>2,0</u> to 4,0	<u>2,0</u> to 4,0
- Balconies	<u>2,5</u> to 4,0	<u>2,0</u> to 3,0
<b>Category B</b>	2,0 to <u>3,0</u>	1,5 to <u>4,5</u>
<b>Category C</b>		
- C1	2,0 to <u>3,0</u>	3,0 to <u>4,0</u>
- C2	3,0 to <u>4,0</u>	2,5 to 7,0 ( <u>4,0</u> )
- C3	3,0 to <u>5,0</u>	<u>4,0</u> to 7,0
- C4	4,5 to <u>5,0</u>	3,5 to <u>7,0</u>
- C5	<u>5,0</u> to 7,5	3,5 to <u>4,5</u>
<b>category D</b>		
- D1	<u>4,0</u> to 5,0	3,5 to 7,0 ( <u>4,0</u> )
- D2	4,0 to <u>5,0</u>	3,5 to <u>7,0</u>

(a)

 Table A1.1: (FT) Values of  $\psi$  factors for buildings

Load	$\psi_0$	$\psi_1$	$\psi_2$
Imposed loads in buildings, category (see EN 1991-1-1)			
Category A: areas in residential buildings	0,7	0,5	0,3
Category B: office areas	0,7	0,5	0,3
Category C: congregation areas	0,7	0,7	0,3
Category D: shopping areas	0,7	0,7	0,6
Category E: storage areas	1,0	0,9	0,8
Category F: traffic area, vehicle weight $\leq 30$ kN	0,7	0,7	0,6
Category G: traffic area, $30$ kN < vehicle weight $\leq 160$ kN	0,7	0,5	0,3
Category H: roofs	0	0	0
Snow loads on buildings (see EN 1991-1-3) <sup>*)</sup> , when			
$s_k < 2,75$ kN/m <sup>2</sup>	0,7	0,4	0,2
$s_k \geq 2,75$ kN/m <sup>2</sup>	0,7	0,5	0,2
Ice loads <sup>**)</sup>	0,7	0,3	0
Wind loads on buildings (see EN 1991-1-4)	0,6	0,2	0
Temperature (non-fire) in buildings (see EN 1991-1-5)	0,6	0,5	0

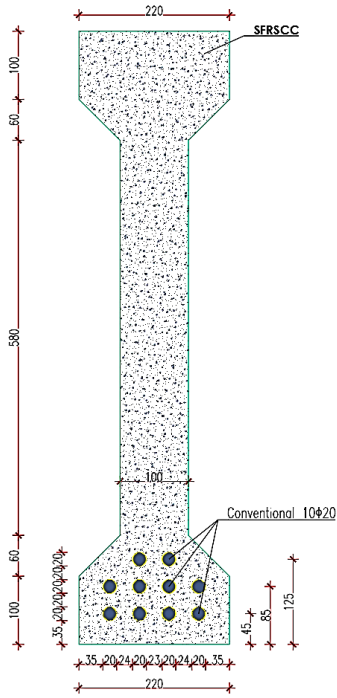
<sup>\*)</sup> Outdoor terraces and balconies  $\psi_0 = 0$  combined with categories A, B, F and G.  
 Note: In case there are different categories of loads in one building, which cannot clearly be separated into different sections, values for  $\psi$  factors giving the most unfavourable effect should be used.  
<sup>\*\*)</sup> Added in the Finnish National Annex

(b)

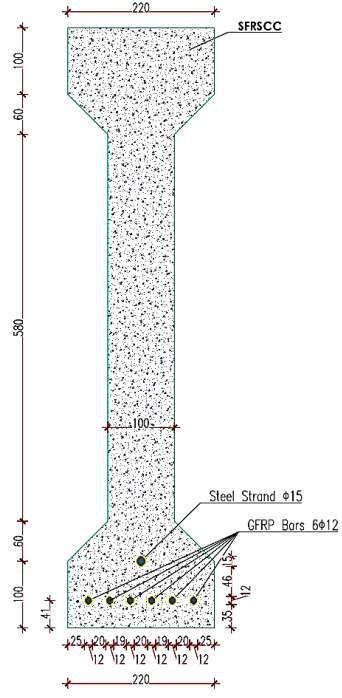
 Figure 52 – Uniformly distributed loads and  $\psi$  factors for office buildings, respectively, according to: (a) Eurocode 1, (b) Eurocode 0.

This section also presents the finite element models used in the numerical simulations carried out in the context of the case study. The description of the FE models includes details of the adopted mesh, boundary conditions, and the respective constitutive laws and parameters that define the models.

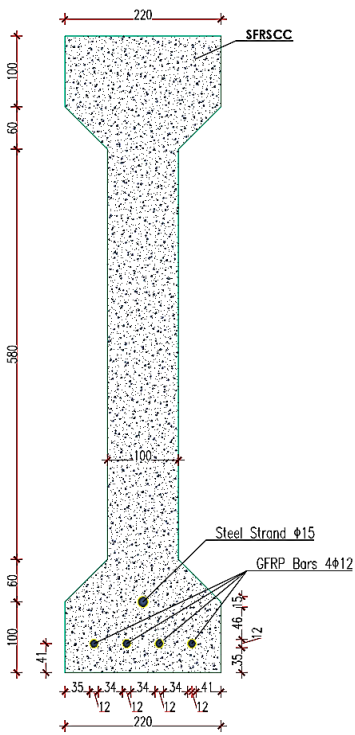
A total of five differently reinforced I-shaped cross-sectional SFRSCC beams were simulated. One beam was longitudinally reinforced with passive conventional steel bars (traditional flexural reinforcement), Figure 53a, two were reinforced with prestressed steel strand and GFRP bars, Figure 53b and Figure 53c, one reinforced with passive conventional steel bars and prestressed GFRP bars, Figure 53d, and another with only prestressed GFRP bars, Figure 53e.



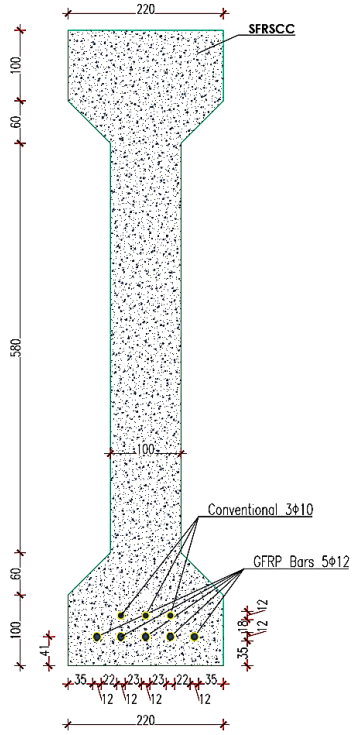
(a)



(b)

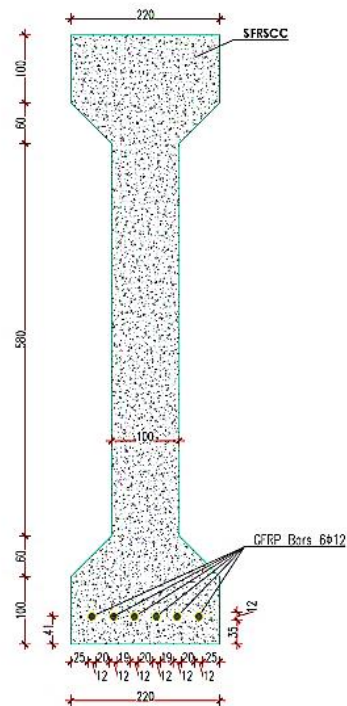


(c)



(d)





(e)

Figure 53 – Numerically simulated beams: (a) A\_10φ20, (b) B1\_6φ12\_φ15, (c) B2\_4φ12\_φ15, (d) B3\_5φ12\_3φ10, (e) C\_6φ12.

The geometry of the finite element mesh used for the beam simulation was the same for all the different reinforced beams. Figure 54 shows an example of the implemented mesh for the beam. Based on the symmetry of the structure, only half of the beam was considered in the simulation.

For the simulation of the steel fibre reinforced self-compacting concrete (SFRSCC) 8-node Serendipity plain stress FE with 2x2 Gauss-Legendre integration scheme was used. The prestressed steel strand and GFRP bars were discretized by 3-node Cable 2D elements with 2 Gauss-Legendre integration points. Additionally, 3-noded Embedded cable 2D elements with 2 points Gauss-Legendre integration scheme were employed for simulating the conventional and passive steel bars. The flexural reinforcement elements were assumed to have a perfect bond with the surrounding concrete elements.

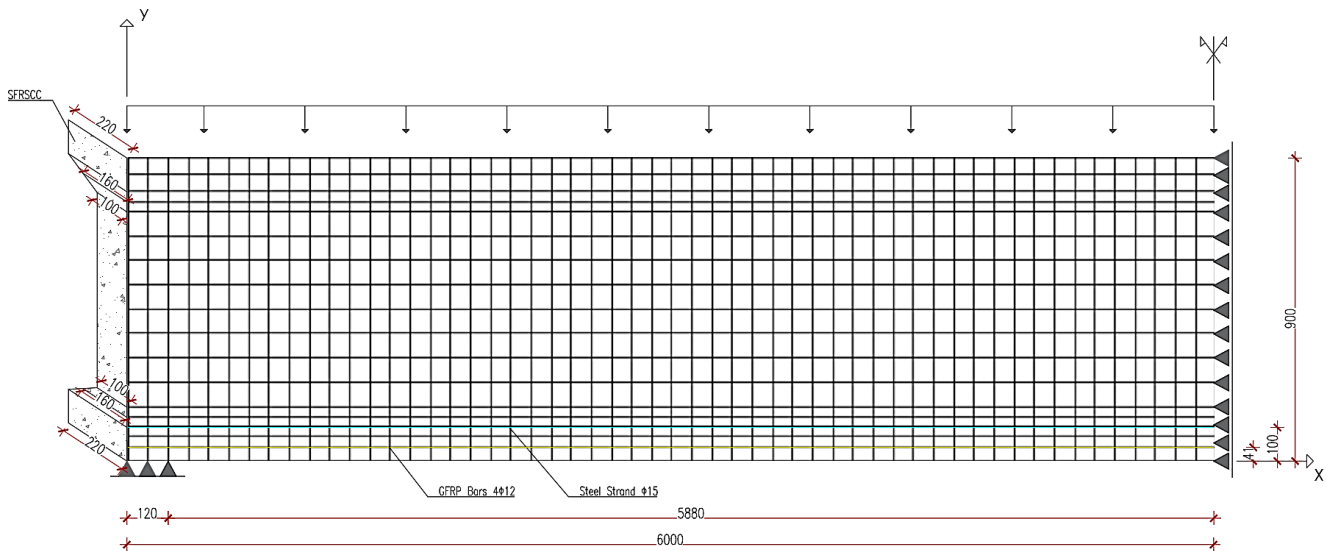


Figure 54 – Geometrical details of the hybrid SFRSCC beam reinforced by prestressed steel strand and GFRP bars (dimensions in mm).

According to the real shape of the developed I beam, Figure 50a, the thickness of the plain stress FE variation was implemented to the nodes at the same horizontal level with respect to its height. For example, 100 mm thickness was assigned to the nodes located at 160 mm from the bottom of the beam up to 740 mm (entire beam web), and 220 mm thickness was assigned to all nodes of the beam flange.

The non-linear material model “NLMM\_104” was used to simulate the behaviour of the SFRSCC and the values assumed for the simulation of this material were derived from the numerical model validation previously presented for shallow beams, Table 12. To simulate the behaviour of the longitudinal reinforcement the “NLMM\_201” constitutive model was used. The parameters used to simulate conventional steel behaviour were the same used in the modelling of the C\_10\_45 shallow beam, presented in Table 13. The values of the constitutive model of the GFRP bars and the steel strand are indicated in Table 7 and Table 16, respectively.

Table 16 – Values of the parameters of the steel strand constitutive model.

Diameter (mm)	$\xi_{sy}$	$\sigma_{sy}(MPa)$	$\xi_{sh}$	$\sigma_{sh}(MPa)$	$\xi_{su}$	$\sigma_{su}(MPa)$	Third branch exponent	Young's modulus (GPa)
15	0,007991	1558,3	0,029	1664,15	0,05	1770	1	195



The steel strand and GFRP bars discretized by Cable 2D finite elements were incorporated with the prestress effect of reinforcements by using a thermal loading condition. In these simulations was adopted a prestress level of 75% of the steel strand yielding stress ( $f_{sy} = 1558.3 \text{ MPa}$ ) and a prestress level of 30% of the GFRP bars ultimate tensile stress ( $f_{fu} = 945.56 \text{ MPa}$ ). The required temperature variation to exhibit the desired amount of pre-strain in the reinforcement was  $-600^\circ\text{C}$  for the steel strand and  $-630^\circ\text{C}$  for the GFRP bars.  $\Delta T$

### 6.2.1. Results and discussion

For the purpose of establishing a comparison between all the I beam studied, the serviceability limit states (deflection limitation, stress limitation and crack control) were calculated according to the recommendations from the Eurocode 2, part 1-1.

In relation to the deflection limit, Eurocode 2, part 1-1, recommends for serviceability limit states a deflection non-superior to  $L/250$ , where  $L$  is the total length of the structure. Therefore, for a loaded length of 12 m, the deflection limit is 48 mm. Figure 55 shows the force-deflection response of the I beam obtained from all the numerical simulations (assuming perfect bond between the reinforcement and the surrounding concrete), where force corresponds to the total uniformly distributed load on the span, and deflection corresponds to the mid-point of the span.

Table 17 presents the respective values of the load-carrying capacity obtained for each beam analysed.

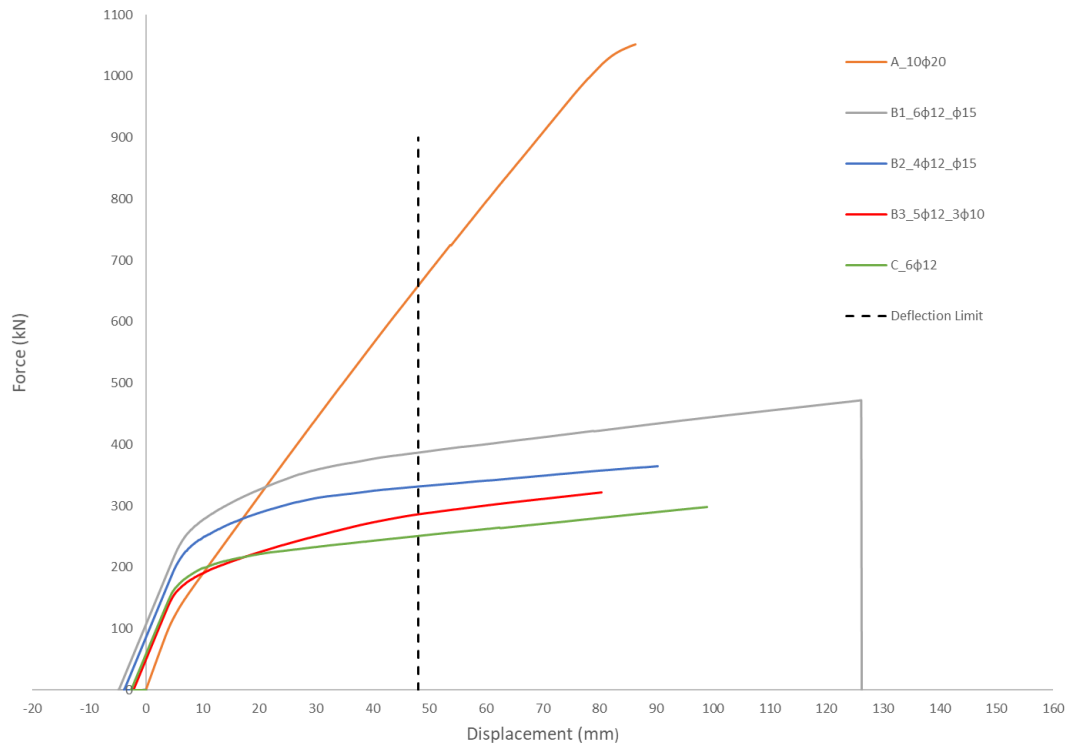


Figure 55 – Force-deflection response of the developed numerical simulations and deflection limitation for serviceability limit states.

In Figure 55, it is evident that there was a substantial increment in the load-carrying capacity when the post cracking strength increases. The conventional steel reinforced beam presented premature concrete crack opening but higher load carrying capacity at serviceability limit states and steel yield initiation compared to all other simulations. The beams with prestressed reinforcement showed ductility performance, which did not happen with the beam with conventional reinforcement.

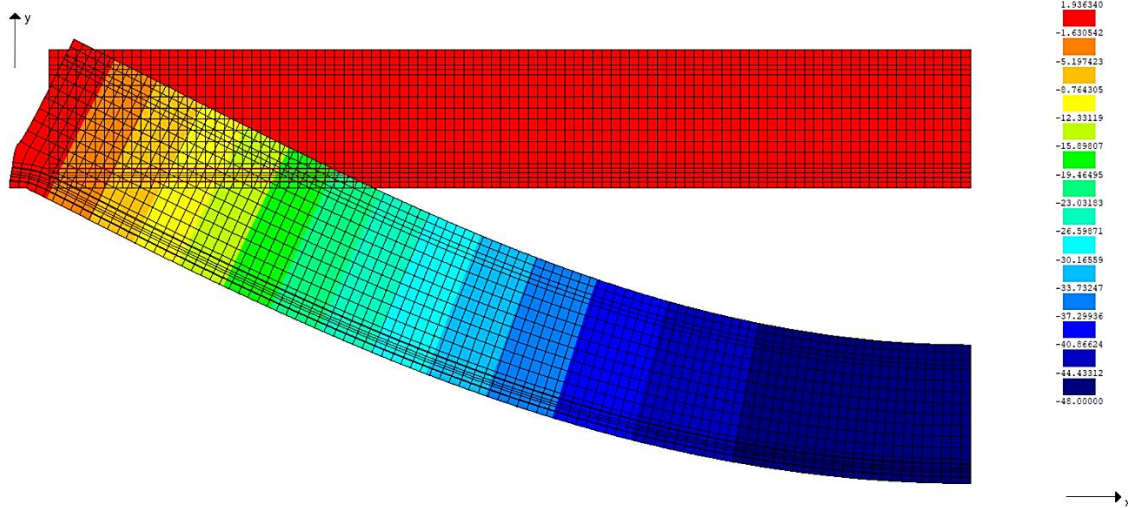
Table 17 – Load carrying capacity at serviceability limit states.

I shaped cross-sectional SFRSCC I beam	Deflection (mm)	Service Load (kN)
A_10φ20		658.87
B1_6φ12_φ15		387.05
B2_4φ12_φ15	48	331.63
B3_5φ12_3φ10		286.33
C_6φ12		250.72

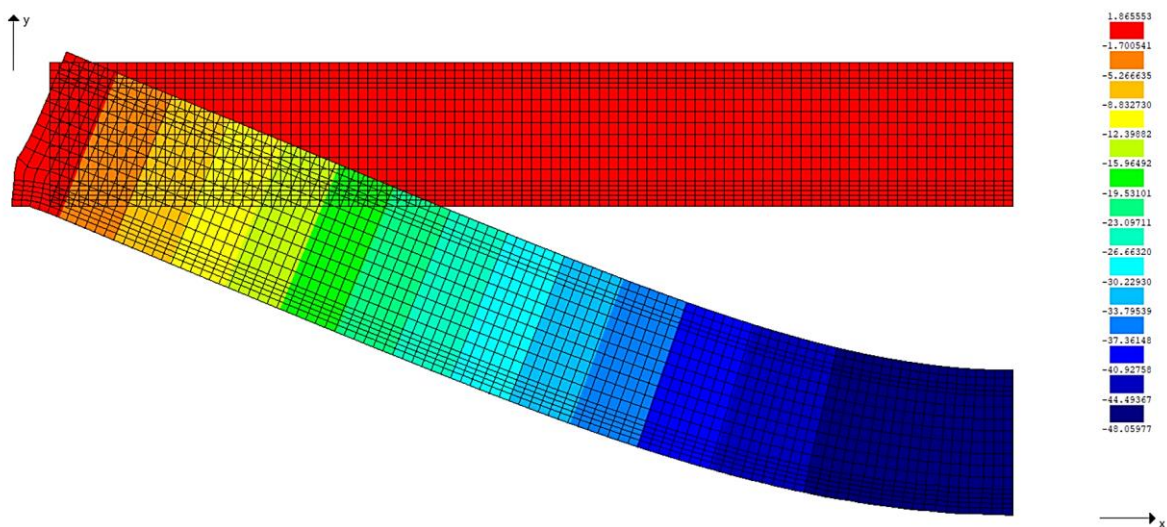
From the analysis of Table 17, is possible to realize that the service load of the beam with traditional reinforcement was 41.3% higher than the best force-deflection response of all other numerically simulated

beams (B1\_6 $\phi$ 12\_ $\phi$ 15). However, the increase in the service load by increasing the prestress level is notable. For example, the service load-carrying capacity of the beam B1\_6 $\phi$ 12\_ $\phi$ 15 was 26% higher than the service load of the beam reinforced with passive conventional steel reinforcement and prestressed GFRP bars (B3\_5 $\phi$ 12\_3 $\phi$ 10).

Hereafter, as a means of comparison, the text will only present the results of the conventional solution (A\_10 $\phi$ 20) and the beam simulation that provided the best results (B1\_6 $\phi$ 12\_ $\phi$ 15). Figure 56 shows the visualization of the deflection at mid-span obtained for the serviceability limit states of those different beam simulations.



(a)



(b)

Figure 56 – Deflection visualization of the numerically simulated beams: (a) A\_10φ20, (b) B1\_6φ12\_φ15 (displacements in mm).

Is important to note that Figure 56 depicts the evolution of the displacements in y (X3) direction. The mid-span deflection of the beams is the deflection limit (48 mm) to which the service load was presented previously.

In relation to the stress limitation, Eurocode 2, part 1-1, suggest that under service load conditions the stress on FRC and steel reinforcements shall be limited in order to reduce the probability of concrete cracking and avoid unacceptable effects on the functionality of the structure. Thus, Eq.(30) shall be used.

$$\sigma_c^k < 0.6 * f_{ck} \quad (30)$$

Where  $\sigma_c^k$  is the compressive stress limitation of concrete in the beam determined for the characteristic load combination, and  $f_{ck}$  is the characteristic compressive strength of the concrete.

As the  $f_{ck}$  is 91.22 MPa, replacing this value in Eq.(30), comes:

$$\sigma_c^k < 0.6 * 91.22 = 54.73 \text{ MPa} \quad (31)$$

For the quasi-permanent combination of actions, Eq.(32) shall be applied.

$$\sigma_c^q < 0.45 * f_{ck} \quad (32)$$

$$\sigma_c^q < 0.45 * 91.22 = 41 \text{ MPa} \quad (33)$$



If Eq.(30) is verified, it indicates that longitudinal cracking of the beam is unlikely to occur. In the other hand, if Eq.(32) is accomplished it represents that creep linearity is ensured, if not, a nonlinear creep should be considered.

To prevent inelastic deformations of the steel longitudinal reinforcements, Eq. (34) shall be used.

$$\sigma_s^k < 0.8 * f_{yk} \quad (34)$$

Where  $\sigma_s^k$  is the steel stress determined for the characteristic load combination of actions.

As the  $f_{yk}$  is 500 MPa, replacing this value in Eq.(34), comes:

$$\sigma_s^k < 0.8 * 500 = 400 \text{ MPa} \quad (35)$$

Under the characteristic combination of actions, the stress in the prestressing reinforcements is controlled by, Eq.(36) and Eq.(37).

$$\sigma_p^k < 0.75 * f_{pk} \quad (36)$$

$$\sigma_p^k < 0.75 * 1770 = 1327.5 \text{ MPa} \quad (37)$$

$$\sigma_f^k < 0.75 * f_{fu} \quad (38)$$

$$\sigma_f^k < 0.75 * 945.56 = 709.17 \text{ MPa} \quad (39)$$

Table 18 presents the stresses in the SFRSCC, steel strand, GFRP bars and conventional steel bars at the critical sections of all the numerically simulated I beams, for the characteristic load combination at the serviceability limit states.

Table 18 – Maximum stresses for serviceability limit states.

I shaped cross-sectional SFRSCC I beam	SFRSCC compressive stress (MPa)	Steel Strand tensile stress (MPa)	GFRP tensile stress (MPa)	Conventional steel tensile stress (MPa)
A_10φ20	40.8	–	–	358.3
B1_6φ12_φ15	31.84	1562	413.7	–
B2_4φ12_φ15	31.42	1560	450.9	–
B3_5φ12_3φ10	27.8	–	403	525
C_6φ12	28.11	–	456.7	–

According to Table 18 the maximum (40.8 MPa) and minimum (27.8 MPa) SFRSCC compressive stress (40.8 MPa) was obtained for the beam reinforced with conventional steel (A\_10φ20) and for the beam with prestressed GFRP bars and passive conventional steel strand (B3\_5φ12\_3φ10), respectively. It is important to note that these compressive stresses occur in the face of the top flange of the beam at the mid-span. Also, it is possible to realize that the analysed sections did not reach the compressive stress limitation for serviceability limit states. For example, the compressive stress obtained for the beam with conventional steel reached only 74.5% of the compressive stress limitation. In comparison, the beam with prestressed GFRP bars and Steel strand (B1\_6φ12\_φ15) reached only 58 % of the maximum compressive stress for serviceability limit states.

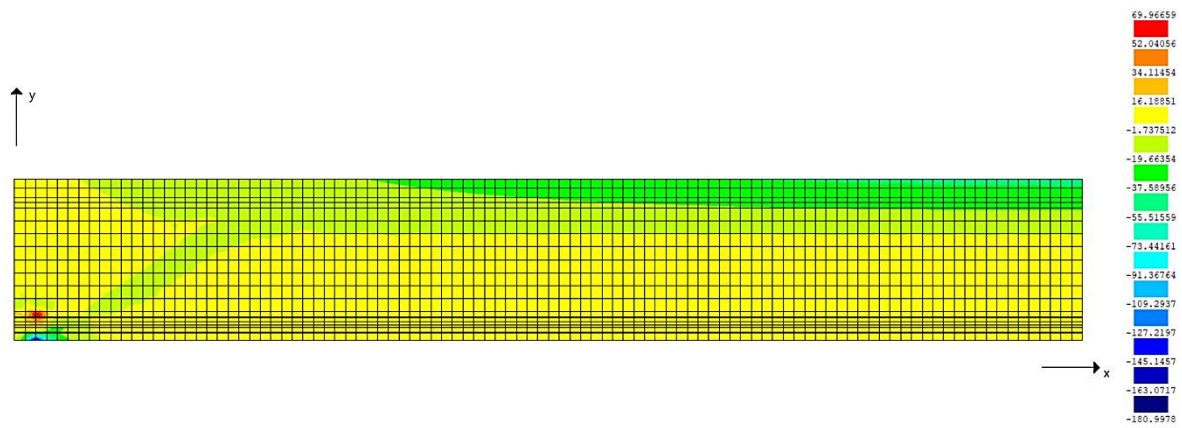
The maximum tensile stress obtained in the GFRP bars (C\_6φ12 beam) is far below the GFRP tensile strength and 35.6 % below the stress limitation for prestressing reinforcements. This situation did not happen to the beam with prestressed GFRP and passive conventional steel bars, as the conventional steel bars ruptured. The stresses in the beam simulation that provided the best results (B1\_6φ12\_φ15) were 41.7% below the maximum stress for this type of prestressing reinforcements, Eq.(38).

In relation to the steel strand tensile stress it is important to mention that in both beams B1\_6φ12\_φ15 and B2\_4φ12\_φ15 the limit concerning the stress for the prestressing reinforcements in Eq.(37) was

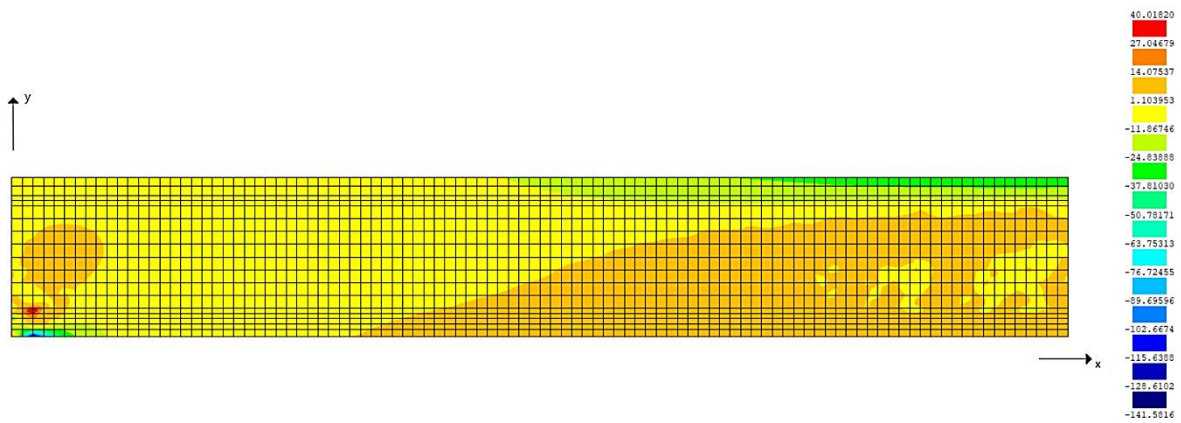


exceeded, but still did not reach the steel strand tensile strength. In this case, the unacceptable level of cracking or deformation of the beam can't be predicted.

Figure 57 depicts the stresses in the SFRSCC in the x-direction obtained for the serviceability limit states. The higher tensile stresses in the SFRSCC occurred in the face of the bottom flange of the beams at mid-span.



(a)



(b)

Figure 57 – Concrete stresses visualization of the numerically simulated beams: (a) A\_10φ20, (b) B1\_6φ12\_φ15.

For the crack control, Eurocode 2 adopts a cracking serviceability criterion in the form of limiting the crack width,  $w_d$ , to a nominal limiting value,  $w_{lim}$ , see Eq.(40). This cracking serviceability criterion should be verified to assure that the requirements concerning functionality, durability and appearance are met.

$$w_d < w_{lim} \quad (40)$$

Where the variable  $w_d$  represents the design value of crack width at the concrete member surface and is determined for the appropriate combination of actions. The nominal crack width limit at the concrete surface,  $w_{lim}$ , must be chosen based on the design situation or specified in the project.

For this specific case study was considered that the exposure to which the beams were subjected was moderate humidity, and according to Eurocode 2, corresponds to the XC3 class designation, Figure 58a. This exposure class recommends a nominal limit value of crack width,  $w_{lim}$ , for serviceability limit states of 0.3 mm, Figure 58b.

**Table 4.1: Exposure classes related to environmental conditions in accordance with EN 206-1**

Class designation	Description of the environment	Informative examples where exposure classes may occur
<b>1 No risk of corrosion or attack</b>		
X0	For concrete without reinforcement or embedded metal: all exposures except where there is freeze/thaw, abrasion or chemical attack For concrete with reinforcement or embedded metal: very dry	Concrete inside buildings with very low air humidity
<b>2 Corrosion induced by carbonation</b>		
XC1	Dry or permanently wet	Concrete inside buildings with low air humidity Concrete permanently submerged in water
XC2	Wet, rarely dry	Concrete surfaces subject to long-term water contact Many foundations
XC3	Moderate humidity	Concrete inside buildings with moderate or high air humidity External concrete sheltered from rain
XC4	Cyclic wet and dry	Concrete surfaces subject to water contact, not within exposure class XC2

(a)

**Table 7.1N Recommended values of  $w_{max}$  (mm)**

Exposure Class	Reinforced members and prestressed members with unbonded tendons	Prestressed members with bonded tendons
	Quasi-permanent load combination	Frequent load combination
X0, XC1	0,4 <sup>1</sup>	0,2
XC2, XC3, XC4	0,3	0,2 <sup>2</sup>
XD1, XD2, XD3, XS1, XS2, XS3		Decompression

**Note 1:** For X0, XC1 exposure classes, crack width has no influence on durability and this limit is set to give generally acceptable appearance. In the absence of appearance conditions this limit may be relaxed.

**Note 2:** For these exposure classes, in addition, decompression should be checked under the quasi-permanent combination of loads.

(b)

Figure 58 – Eurocode 2, part 1-1 design recommendations: (a) exposure classes, (b) recommended values of  $w_{lim}$  for the exposure classes.

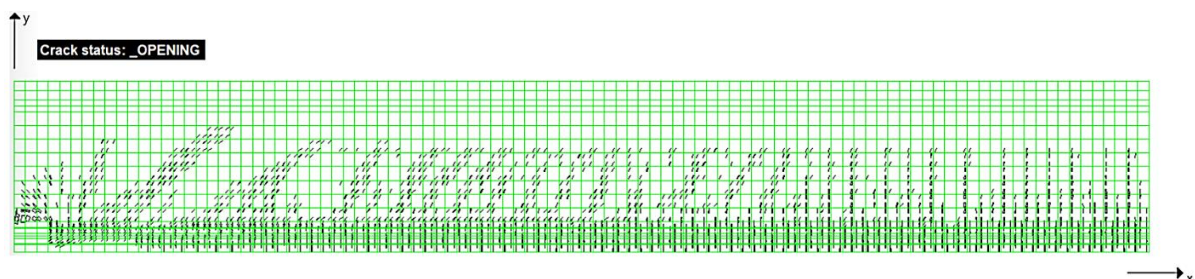
Table 19 summarizes the maximum crack width at the mid-span of the beams for the characteristic combination of actions at the serviceability limit states. The crack width was obtained by multiplying the crack normal strain in the direction of the beam's axis by the crack band width (values from the numerical analysis).

Table 19 – Maximum crack width for serviceability limit states.

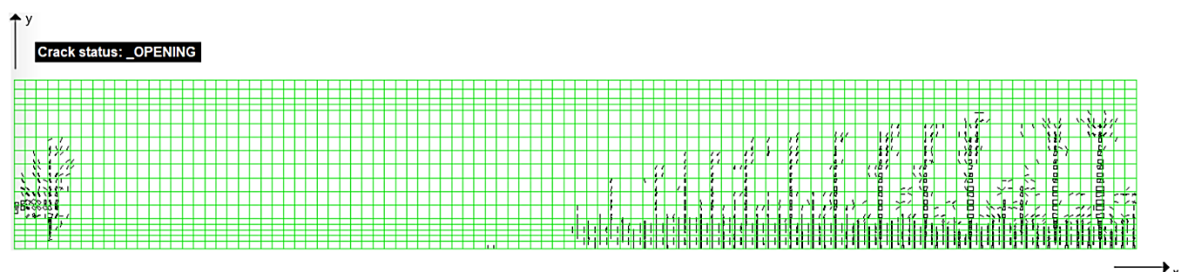
I shaped cross-sectional SFRSCC I beam	Crack width (mm)	Máx. Crack width (mm)
A_10φ20	0.03	
B1_6φ12_φ15	0.055	0.3
B2_4φ12_φ15	0.07	
B3_5φ12_3φ10	0.091	
C_6φ12	0.072	

The maximum crack width (0.091 mm) was obtained in the beam reinforced with prestressed GFRP bars and passive conventional steel bars, whereas the minimum crack width (0.03 mm) was obtained in the beam reinforced with conventional steel bars. However, the nominal limit value of crack width for serviceability limit states was not reached.

Figure 59 displays the crack pattern obtained from the A\_10φ20 beam and the B1\_6φ12\_φ15 beam, where the maximum computed crack width was about 0.03 mm and 0.055 mm in Figure 59a and Figure 59b, respectively, in the mid-span zone of the finite element mesh.



(a)



(b)

Figure 59 – Crack pattern visualization of the numerically simulated beams: (a) A\_10φ20, (b) B1\_6φ12\_φ15.

From Figure 59 is possible to observe some crushing around the support and closely spacing cracks appearing progressively. In the beam reinforced with conventional steel the shear cracks were more pronounced than the flexural cracks. Also, the shear cracks in this beam were starting to being progressively converted in diagonal shear ones, which leded to shear failure cracks propagated along the longitudinal reinforcements in one extremity of the beam and towards the applied load in the other extremity. On the other hand, the hybrid beam presented flexural cracks which probably leded to flexural failure. This better performance behaviour was due to the application of prestress in the reinforcement which increased the bridging effect of a high number of steel fibres across the cracks.

### 6.2.2. Influence of the GFRP-SFRSCC bond conditions on force-deflection response of I-shaped cross-sectional beams

To assess the influence on the bond conditions between the GFRP bars and the SFRSCC in relation to the force *versus* slip response of I beams flexurally reinforced with GFRP bars, a material nonlinear analysis with FEMIX was carried out with the same numerically simulated beam represented in Figure 53d. The difference in this analysis was that passive GFRP bars were used instead of prestressed ones.

The geometry of the finite element mesh used in this numerical simulation is depicted in Figure 60.

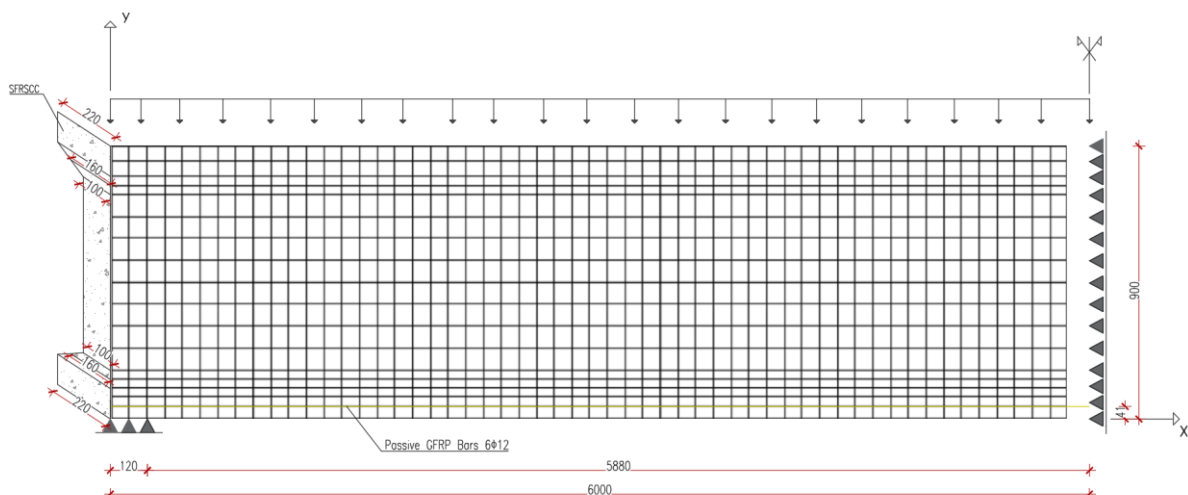


Figure 60 – Geometrical details of the SFRSCC beam reinforced with passive GFRP bars (dimensions in mm).

For the simulation of the SFRSCC 8-node Serendipity plain stress FE with 2x2 Gauss-Legendre integration scheme was used. The GFRP bars were discretized by 3-node Embedded cable 2D elements with 2 points Gauss-Legendre integration scheme. Two simulations were carried out assuming the bond-slip equation (23) with the parameters indicated in Table 8 for the C25LB200 series (SFRSCC cover of 25 mm and 200 mm of bond length) and assuming perfect bond between the GFRP bars and the surrounding concrete. It is of major importance to note that the local bond law used in this simulation was determined for a different GFRP bar diameter ( $\Phi 5$  mm) and concrete cover thickness (25 mm). The adopted diameter in the I beam simulation ( $\Phi 12$  mm) was 2.4 times higher than the adopted for the series local bond law determination and the concrete cover thickness (35 mm) was 1.4 times higher. However, the SFRSCC properties used in the simulations were the same used in the pullout bending tests for the determination of the local bond laws. This difference in the modelling could generate discrepancies in the results. The interface finite elements used to simulate the bond behaviour between the GFRP bars and the surrounding SFRSCC were modelled by 4-nodes-2D-interface elements with 2 Gauss-Legendre integration points.

Figure 61 shows the load *versus* mid-span deflection at the last load combination for both simulations, one allowing the slip between GFRP bars and surrounding SFRSCC and the second assuming perfect bond of the interaction GFRP-SFRSCC.

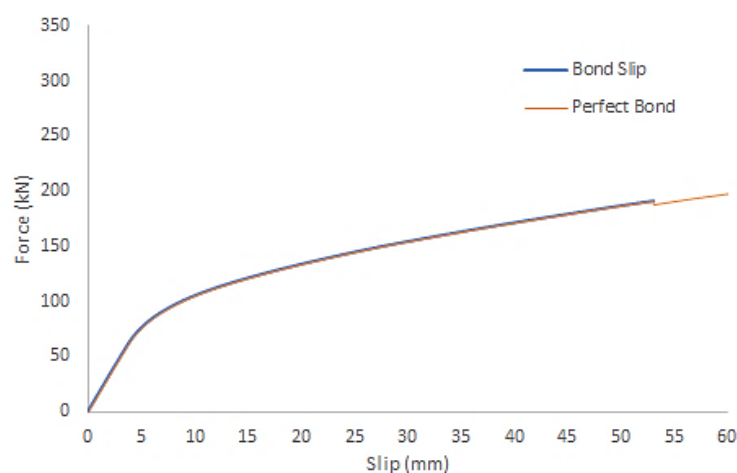


Figure 61 – Load *versus* mid-span deflection assuming bond slip and perfect bond between GFRP bars and surrounding SFRSCC.

As mentioned before, the difference between assuming bond slip and perfect bond in the simulations was minimum and because of that was concluded that the bond conditions in this situation do not have



relevant effect on the load carrying capacity of the simulated beams. Furthermore, the numerical analysis revealed that bond conditions did not affect the maximum crack width and stresses of the beams. This conclusion could be misled because of the bond law assumed in the bond-slip simulation, which could be studied in future works.

# Chapter 7

## 7. Summary and Conclusions

The present dissertation aimed to study a new generation of structural reinforcement systems for concrete structures by using high-performance materials, especially the Steel Fibre Reinforced Self-Compacting Concrete (SFRSCC) and Glass Fibre Reinforced Polymer (GFRP). The advantages of prestressing the GFRP bars and Steel Strand in the design reinforcement of structural elements were also investigated. A major focus of this work was the development, validation, and implementation of constitutive models for the materials using analytical and numerical tools.

In this scope, chapter one was dedicated to the establishment of the dissertation by highlighting the importance and objective of the study.

Chapter two laid the groundwork for some knowledge about the materials behaviour used in the investigation process carried out in this dissertation. One braided composite rod (BCR) that composes the 3D-SRT (3-Dimensional System Reinforcement Textile) was studied in this dissertation, here mentioned as GFRP bar. Besides, some information was retained about the bond behaviour between FRC and FRP bars, the influence of steel fibres in FRC, and the shear capacity of FRC beams. For example, the bond performance influences the load carrying capacity of a reinforced element and the parameters that influence the pullout bending tests are essentially the concrete cover thickness, anchorage length, bar diameter and bar surface treatment.

Chapter three and four was focused on the evaluation of bond behaviour between GFRP bars and SFRSCC. The experimental program showed that the pullout force increases almost linearly with the anchorage length and the values of the average bond stress ( $\bar{\tau}_{max}$ ) decreased with the increase of anchorage length. Furthermore, the experimental program showed that the concrete cover thickness had no influence on the bond relationship. In chapter four was developed an analytical and numerical model with the FBL and FEMIX computer programs, respectively, to determine the bond-slip law for the pullout bending tests. Those approaches were compared and validated with the experimental results and it is important to note that they were capable of simulating with good accuracy the pullout force *versus* loaded end slip for all specimen series tested.



Chapter five was one of the most important chapters of the dissertation because in this chapter was determined the constitutive models of the concrete, conventional steel and GFRP. The validation of the numerical models of shallow beams based on previous experimental work allowed the numerical simulation of bending tests of I beams in chapter six. The use of the software GID in the beams modelling was, with no doubt, very useful because it allowed the creation of the geometry of the numerical model, mesh generation and visualization of the analysis with precision and easiness. The numerical force-deflection results of the shallow beams failing in bending was predicted with reasonable accuracy. In the last part of the chapter the beams were numerically simulated with different longitudinal reinforcement (GFRP and Prestressed steel wires) in order to analyse its performance. It can be said that fibre reinforced beams present higher load carrying capacity and the energy dissipation decreases slowly, and the application of prestress in the beam's reinforcements provide significant increase in the load carrying capacity at serviceability limit states.

In chapter six it was developed a hypothetical case study on using I-shaped-cross-sectional beams with long span in office buildings. The I shaped-cross-section was adopted for the beams in order to optimize their flexural performance. Five differently reinforced beams were numerically simulated. The behaviour of the beams A\_10 $\phi$ 20 and B1\_6 $\phi$ 12\_ $\phi$ 15 deserved major attention because demonstrated better performance and for comparison purposes. The service load of the beam with traditional reinforcement was 41.3% higher than the force-deflection response of the B1\_6 $\phi$ 12\_ $\phi$ 15 beam. The beams with prestressed reinforcement showed ductility performance, which did not happen with the beam with conventional reinforcement. In relation to the serviceability limit states the compressive stress obtained for the beam A\_10 $\phi$ 20 reached 74.5% of the compressive stress limitation whereas the beam B1\_6 $\phi$ 12\_ $\phi$ 15) reached only 58 %. The crack patterns showed potential shear failure of the beam reinforced with conventional steel and potential flexural failure of the beam reinforced with prestressed GFRP bars and steel strand.

The analysis on the influence of the GFRP-SFRSCC bond conditions on force-deflection response of I-shaped cross-sectional beams showed no relationship.



## Bibliography

- [1] T. Valente, "Advanced tools for design and analysis of fiber reinforced concrete structures," 2019.
- [2] J. Ryu, A. Carazo, K. Uchino, and H. Kim, "Magnetolectric properties in piezoelectric and magnetostrictive laminate composites," *Japanese Journal of Applied Physics, Part 1: Regular Papers and Short Notes and Review Papers*, vol. 40, no. 8, pp. 4948-4951, 2001.
- [3] J. Lees, and C. Burgoyne, "Experimental Study of the Influence of Bond on the Flexural Behaviour of Concrete Beams Pre-tensioned with AFRPs," no. February 2017, 1999.
- [4] V. Worner, "Use of Glass Fibre Reinforced Polymer ( GFRP ) reinforcing bars for concrete bridge decks," 2015.
- [5] A. E. Naaman, and H. W. Reinhardt, "Proposed classification of HPFRC composites based on their tensile response," *Materials and Structures*, p. 547–555, 2006.
- [6] H. Mazaheripour, "Structural Behavior of Hybrid GFRP and Steel Reinforced FRC Prestressed Beams," no. December, 2015.
- [7] E. B. Pereira, G. Fischer, and J. A. O. Barros, "Direct assessment of tensile stress-crack opening behavior of Strain Hardening Cementitious Composites (SHCC)," *Cement and Concrete Research*, vol. 42, no. 6, pp. 834-846, 2012.
- [8] J. M. Sena-Cruz, "Strengthening of concrete structures with near-surface mounted CFRP laminate strips," *PhD Thesis*, p. 216, 2005.
- [9] F. Micelli, and A. Nanni, "Durability of FRP rods for concrete structures," *Construction and Building Materials*, vol. 18, no. 7, pp. 491-503, 2004.
- [10] C. Buckner, M. Masuelli *et al.*, "We are IntechOpen , the world ' s leading publisher of Open Access books Built by scientists , for scientists TOP 1 %", *Intech*, 2016.
- [11] T. International, C. Lyon, "USED IN CIVIL ENGINEERING APPLICATIONS," no. i, pp. 1-9, 2005.
- [12] R. Lameiras, J. A. O. Barros, and M. Azenha, "Influence of casting condition on the anisotropy of the fracture properties of Steel Fibre Reinforced Self-Compacting Concrete (SFRSCC)," *Cement and Concrete Composites*, vol. 59, pp. 60-76, 2015.
- [13] FIB, "Model Code 2010 - Vol.1," no. 1, pp. 1-5, 2014.
- [14] J. A. O. Barros, and J. M. Sena-Cruz, "Fracture energy of steel fibre reinforced concrete," *Mech. Compos. Mater. Struct.*, vol. 8, no. 1, pp. 29-45, 2001.
- [15] Y. Perera, R. Muwanwella, P. Fernando *et al.*, Evolution of 3D weaving and 3D woven fabric structures, Springer Singapore, 2021.
- [16] J. HU, "Introduction to three-dimensional fibrous assemblies," in *3-D Fibrous Assemblies*, pp. 1-32, 2008.

- [17] R. Manuel, and E. Figueiro, "INNOVATIVE CONSTRUCTION SYSTEM FOR A NEW GENERATION," 2020.
- [18] E. Sasi, and A. Peled, "Three dimensional (3D) fabrics as reinforcements for cement-based composites," *Composites Part A: Applied Science and Manufacturing*, vol. 74, pp. 153-165, 2015.
- [19] A. Cascardi F. Longo, F. Micelli, and M. Aiello, "Compressive strength of confined column with Fiber Reinforced Mortar (FRM): New design-oriented-models," *Construction and Building Materials*, vol. 156, pp. 387-401, 2017.
- [20] H. Salehian, J. A. O. Barros, and M. Taheri, "Evaluation of the influence of post-cracking response of steel fibre reinforced concrete ( SFRC ) on load carrying capacity of SFRC panels," *Construction and Building Materials*, vol. 73, pp. 289-304, 2014.
- [21] V. M. C. F. Cunha, *Steel fibre Reinforced Self-Compacting Concrete (from Micro-Mechanics to Composite Behaviour)*, p. 365, 2010.
- [22] A. Abrishamba, V. M. C. F. Cunha, and J. A. O. Barros, "The influence of fibre orientation on the post-cracking tensile behaviour of steel fibre reinforced self-compacting concrete," *Fract. Struct. Integr. J.*, vol. Volume 31, no.1, pp. 38–53, 2015.
- [23] L. Ferrara, N. Ozyurt, and M. Di Prisco, "High mechanical performance of fibre reinforced cementitious composites: The role of "casting-flow induced" fibre orientation," *Materials and Structures/Materiaux et Constructions*, vol. 44, no. 1, pp. 109-128, 2011.
- [24] M. Rudzki, M. Bugdol, and T. Ponikiewski, "An image processing approach to determination of steel fibers orientation in reinforced concrete," *Lecture Notes in Computer Science (including subseries Lecture Notes in Artificial Intelligence and Lecture Notes in Bioinformatics)*, vol. 7339 LNBI, no. June, pp. 143-150, 2012.
- [25] J. A. O. Barros, "Comportamento do betão reforçado com fibras," Thesis, 1995.
- [26] Y. Wang, and S. Backer, "Toughness determination for fibre reinforced concrete," *International Journal of Cement Composites and Lightweight Concrete*, vol. 11, no. 1, pp. 11-19, 1989.
- [27] Y. Şahin, and F. Köksal, "The influences of matrix and steel fibre tensile strengths on the fracture energy of high-strength concrete," *Construction and Building Materials*, vol. 25, no. 4, pp. 1801-1806, 2011.
- [28] L. Magistrale, P. Fantilli, "SYSTEMS : EXPERIMENTAL AND NUMERICAL," 2020.
- [29] T. Soetens, "Design models for the shear strength of prestressed precast steel fibre reinforced concrete girders", *V. Constructies*, 2015.
- [30] J. A. O. Barros, and S. J. Foster "An integrated approach for predicting the shear capacity of fibre reinforced concrete beams," *Engineering Structures*, vol. 174, no. May, pp. 346-357, Nov. 2018.
- [31] European Committee for Standardization, Eurocode 2: Design of concrete structures Part 1-1: General rules and rules for buildings, vol. NP EN 1992-1-1. 2010.



- [32] RILEM TC 162-TDF, "Recommendations of RILEM TC 162-TDF: Test and design methods for steel fibre reinforced concrete: bending test," *Mater. Struct.*, vol. 35, no. 253, pp. 579–582, 2002.
- [33] M. Pepe, H. Mazaheripour, J. Barros, J. M. Sena-Cruz, and E. Martinelli, "Numerical calibration of bond law for GFRP bars embedded in steel fibre-reinforced self-compacting concrete," *Compos. Part B Eng.*, vol. 50, pp. 403–412, Jul. 2013.
- [34] J. Barros, V. M. C. F. Cunha, and J. M. Sena-Cruz, "Pullout behavior of steel fibres in self-compacting concrete," *ASCE Materials in Civil Engineering Journal*, pp. 1-9, Jan. 2010.
- [35] A. Ventura-Gouveia, "Constitutive models for the material nonlinear analysis of concrete structures including time dependent effects," PhD Thesis, Department of Civil Engineering, University of Minho, 2011.
- [36] S. Santos, "The bending and shear behaviour of laminar structures of high performance fibre reinforced concrete," *University of Minho Guimaraes*, 2010.
- [37] R. Ribas, "Modelação de vigas de betão armado reforçadas à flexão com laminados de CFRP inseridos," 2016.
- [38] ASTM International, *Standard Test Method for Flexural Performance of Fiber-Reinforced Concrete (Using Beam With Third-Point Loading)*, vol. ASTM C1609. 2012.
- [39] J. A. Barros, L. A. Lourenço, F. Soltanzadeh, and M. Taheri, "Steel-fibre reinforced concrete for elements failing in bending and in shear," *Eur. J. Environ. Civ. Eng.*, vol. 18, no. 1, pp. 33–65, 2014.
- [40] J. M. Sena-Cruz, and J. A. O. Barros, "Bond between near-surface mounted carbon-fibre-reinforced polymer laminate strips and concrete," vol. 8, no. 6, December 2005.

## APPENDIX A

### Numerical modelling using the FEMIX-GID software

To start the simulation of the beam is necessary to introduce the data related to the beams that define its geometry, such as the vertices of the beam and the intersection points between the faces of the beam and the longitudinal reinforcement (command: **Geometry** → **Create** → **Point or Straight line**).

The concrete and steel surfaces were created after the main points of the beam's geometry had been defined, see Figure 62.

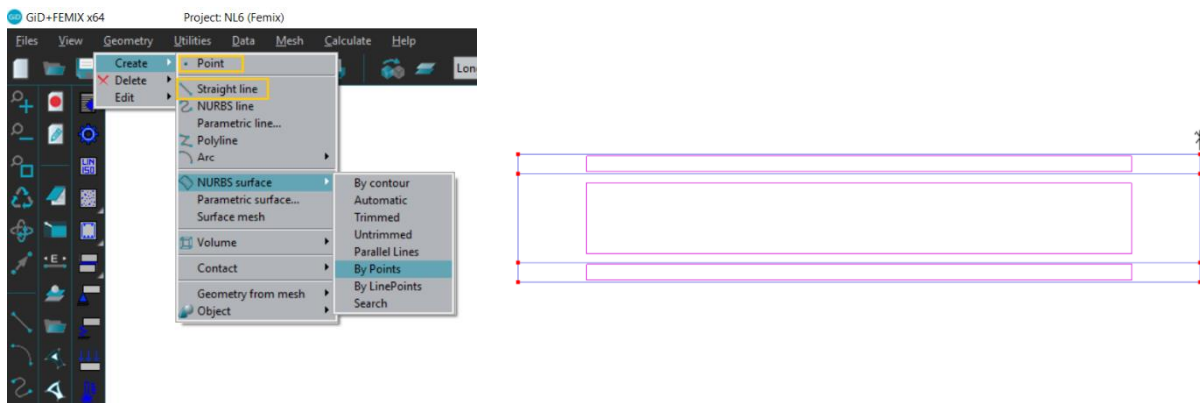


Figure 62 – Creation of points, lines, and surfaces for A\_6\_0 series by using points.

The area that defines the rectangular surface of the concrete was delimited by four points in the extreme vertices of the beam. To identify the top (tensile zone) and bottom (compression zone) longitudinal steel reinforcement was necessary to create two reference lines using two points that allowed the creation of surfaces between the reinforcement and the surrounding concrete. To distinguish and characterize the materials used in the simulations, SCC and Conventional Steel in this example were discretized by layers as well as the top and bottom steel reinforcement (commands: **Layers** → **Create a new layer**; **Select the layer and click with the right button of the mouse** → **Send to** → **Points, Lines or Surfaces**), as shown in Figure 63. A poorly defined geometry of the structure or the information about the intervening materials around it will cause issues when creating the numerical mesh and the future analysis. This first phase is probably the most important for the numerical modelling.

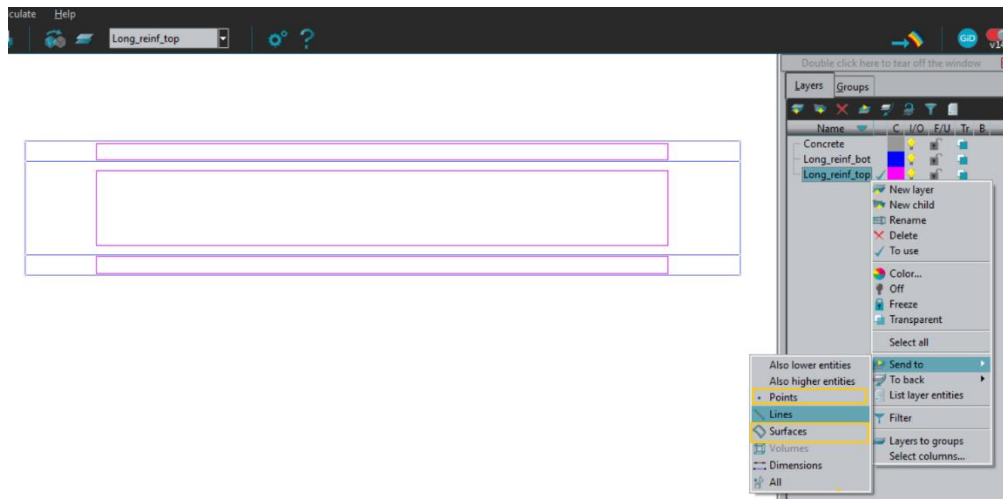


Figure 63 – Creation and association of layers to the materials.

After defining all the geometry of the beam and the layers that characterize each material, the next step was to create the finite element mesh with an intermediate level of refinement that thought to be acceptable.

The concrete used in the beams was simulated by 8-noded Serendipity plane stress finite elements with 3x3 Gauss-Legendre integration scheme, Figure 64, and quadratic 3-noded Embedded cable 2D with two points Gauss-Legendre integration scheme was used to simulate the longitudinal reinforcements. Is important to note that the steel bars were assumed to be perfectly bonded and embedded into the surrounding concrete.

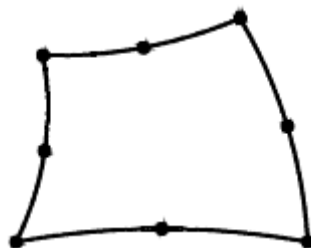


Figure 64 – Serendipity 8-node finite element [8].

This type of elements are associated to the mesh using the quadratic function available in GID as shown in Figure 65, (command: **Mesh** → **Quadratic type** → **Quadratic**). If the user pretends to associate less nodes to the element, the option is to use the Normal function, which is associated with 4-node finite elements (for concrete) and 2-node finite elements (for reinforcement).

The next step for the construction of the mesh is to define the number of finite elements. To introduce the intermediate level of refinement pretended to the mesh, it is necessary to attribute the number of cells and the cell size to create the elements (command: **Mesh** → **Structured** → **Surfaces or Lines** → **Assign number of cells or Assign size**). The function *Assign number of cells* defines the number of cells that the element is pretended to be divided and *Assign size* defines the size of the previous divided cell, in millimetres, Figure 66.

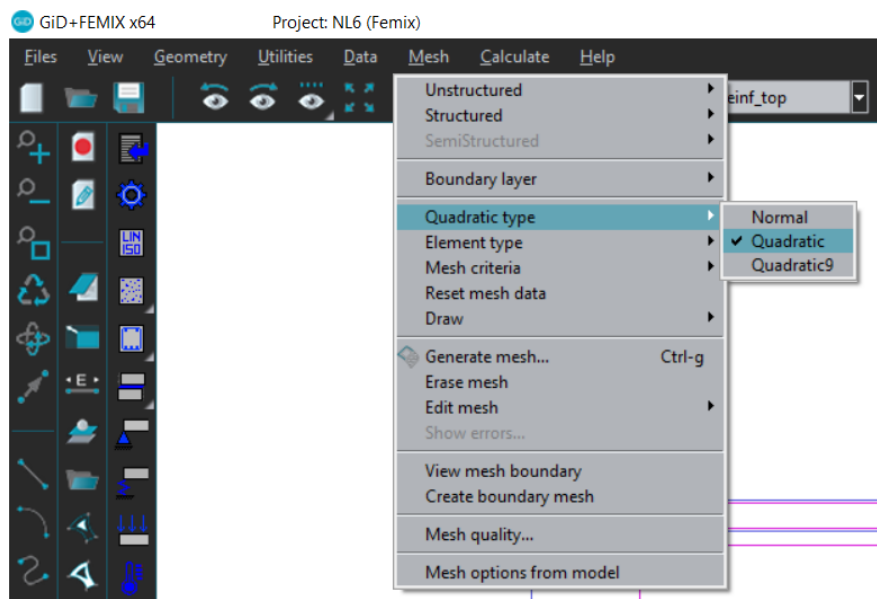


Figure 65 – Finite element number of integration points selection.

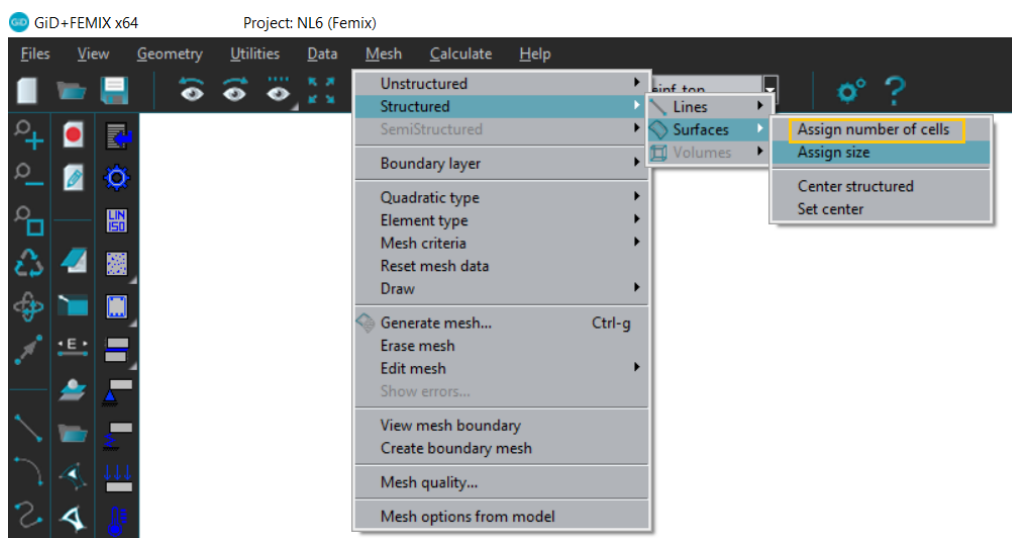


Figure 66 – Attribution of the number of cells and corresponding size to define the finite elements.

For the creation of the mesh and using the *Assign size* function firstly is necessary to select the surface for concrete and the lines for the reinforcement. After that, press ESC and introduce the value for the lateral dimension of a finite element in millimetres. Subsequently press “Assign” and select the element to assign the chosen dimension doing the same process for each surface or line. The process for using the function *Assign number of cells* is similar to the one described previously, except that the imputed values refer to the number of cells that will divide the selected element. In the case of surfaces (Self-compacting concrete in this example) the commands to used are **Mesh** → **Structured** → **Surfaces** → **Assign number of cells** or **Assign size** and for lines (conventional steel reinforcement or GFRP) the commands are **Mesh** → **Structured** → **Lines** → **Assign number of cells** or **Assign size**.

Once the creation of the finite elements is concluded the next step is to generate the mesh (command: **Mesh** → **Generate mesh**). It is of high importance to collapse the mesh after its generation because there is a possible overlap of the nodes of the concrete with the nodes of the reinforcement (command: **Mesh** → **Edit mesh** → **Collapse** → **Mesh**). Figure 67 shows how the commands are introduced in the software for the generation of the mesh and its collapsing.

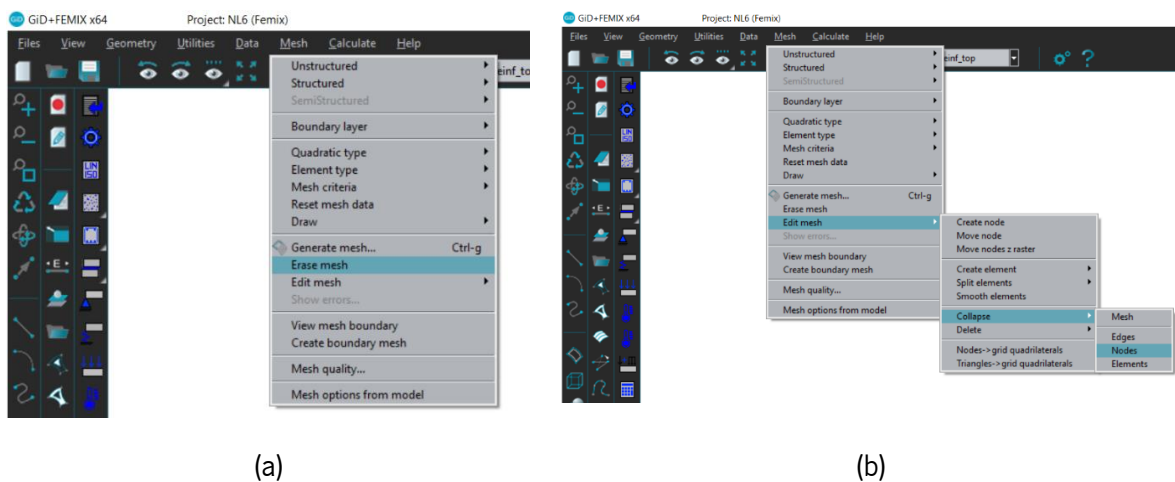


Figure 67 – Creation of the finite element mesh: (a) Generate the mesh, (b) Collapse the nodes of the mesh.

The example of the created finite element mesh for beams reinforced with 6 mm diameter longitudinal steel bars and without steel fibres in the self-compacting concrete (A\_6\_0) is depicted in Figure 68. After the creation of the mesh is necessary to introduce the information concerning the characteristics of the materials, the supports, the prescribed loads/displacements, and existing combinations.

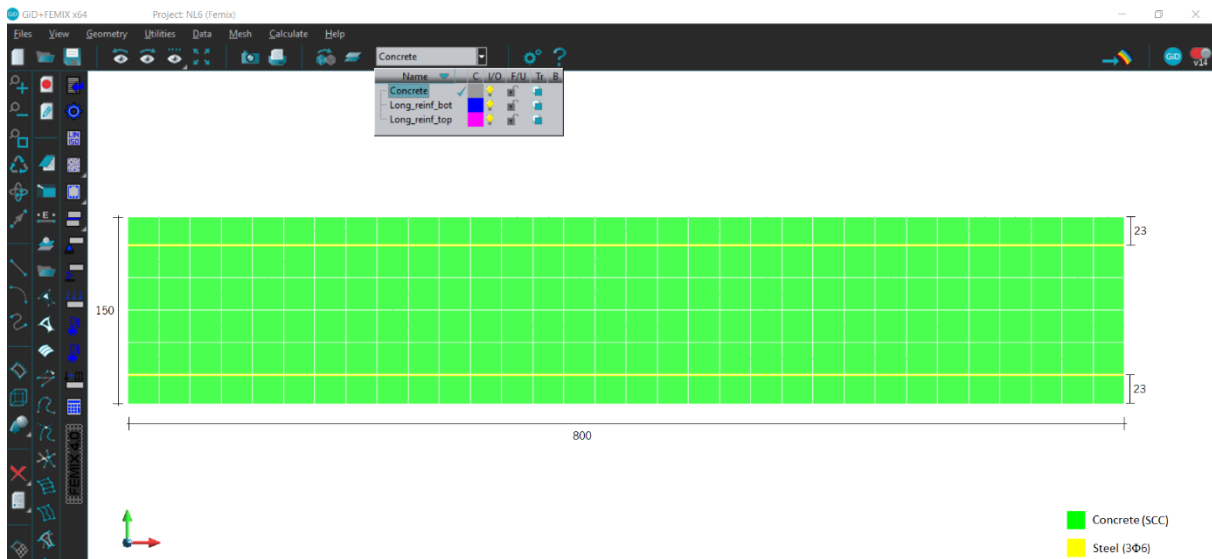


Figure 68 – Finite element mesh used for the simulation of A\_6\_0 series (dimensions in mm).

The numerical analysis is possible due to different structural calculation software available in GID. To choose the software to perform the calculations of the structure that has been modelled the (*Problem type*) must be defined. In the context of the present dissertation, the software chosen was FEMIX (command: **Data** → **Problem type** → **FEMIX**), see Figure 69.

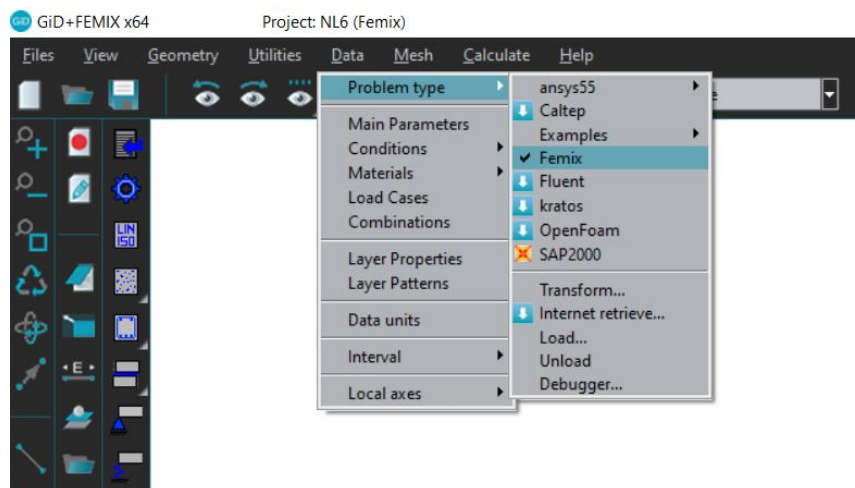


Figure 69 – Calculation software used along with GID.

In relation to the element properties assumed in the simulation of A\_6\_0 series two types of elements were used: Plane stress quad elements for concrete and Embedded cable 2D elements for the reinforcement. It was necessary to introduce the beam thickness (350 mm) to correctly define the plane



stress quad element and the cross-section area of the longitudinal reinforcement (in this simulation the total cross-section area of the top and bottom steel reinforcement was equal:  $84.82 \text{ mm}^2$ ) to define the Embedded cable 2D elements. Figure 70 shows how the different properties were attributed to the elements (command: **Data** → **Conditions** → **Element Properties**). Is of major importance to ensure that all the element properties have been correctly assigned at the end of entering all the values for all the layers (command: **Data** → **Conditions** → **Element Properties** → **Draw** → **Colours**), see Figure 71.

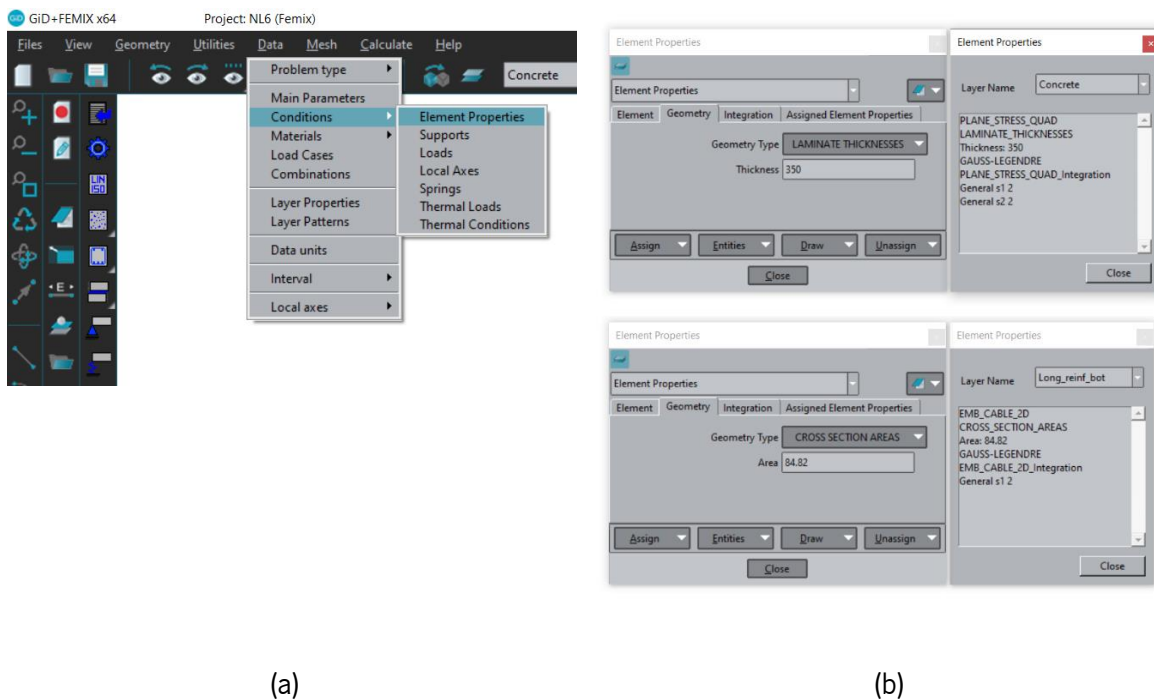


Figure 70 – Introduction of the mesh element properties: (a) Command, (b) Imputed element properties.



Figure 71 – GID graphic visualization of the element properties defined for each layer.

To input the information about the supports used in simulation of the beam bending test is necessary to select the finite element mesh node where the support is placed and define in which direction the movement is restrained (command: **Data** → **Conditions** → **Supports** → **Selection of the node** → **Assign**). In this simulation was considered a roller support at the symmetry axle (restrained in x and z) of the slab strip and a pinned support (restrained in x and y) at 125 mm from the lateral side of the slab, as shown in Figure 72.

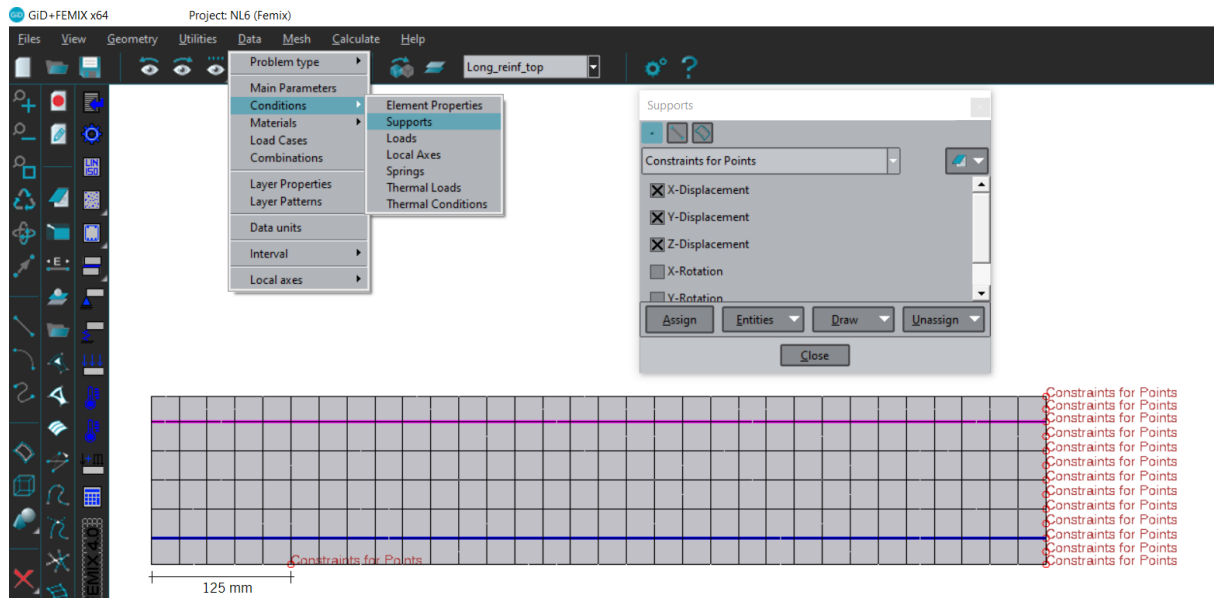


Figure 72 – Supports of the shallow beams.

To assign a load or displacement to a finite element mesh node is necessary to input the values in the desired direction (x,y or z) and select the correct mesh node. The information on how loads or prescribed displacements are introduced to GID is depicted in Figure 73 (command: **Data** → **Conditions** → **Loads** → **Input the value** → **Selection of the node** → **Assign**).

It was also necessary to characterize the concrete and the reinforcement in the tests. To simulate the post-cracking behaviour of the concrete, a quadrilinear tensile-softening diagram available in the software was used and the Fracture Mode I parameters were defined.

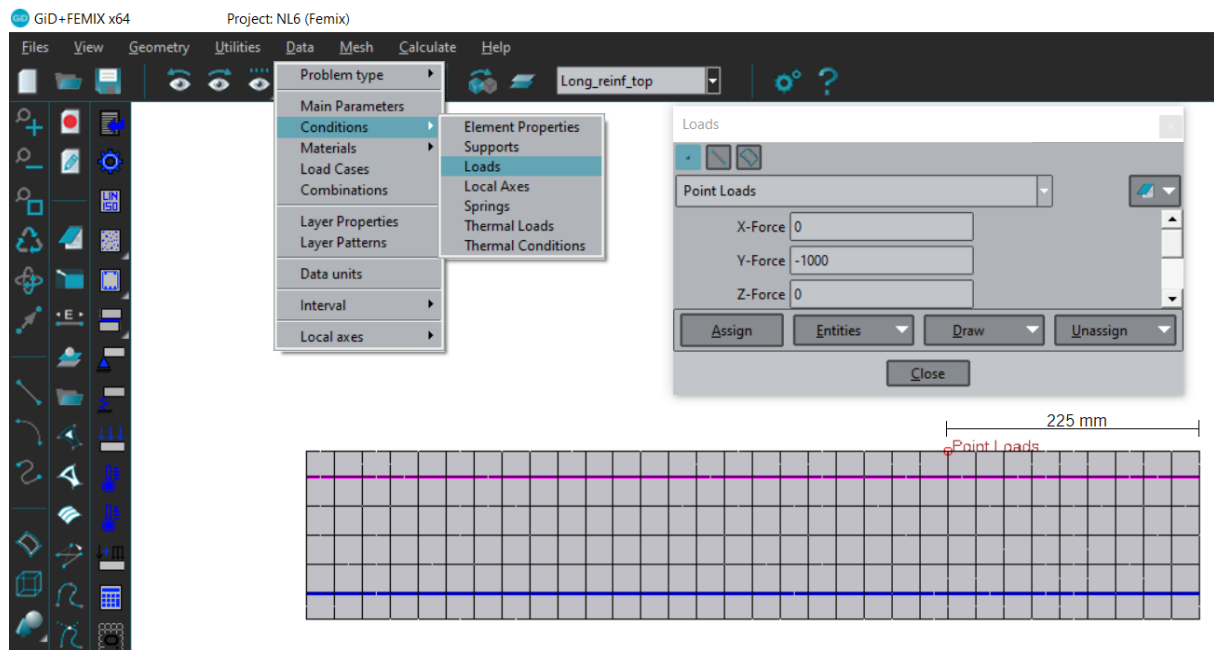


Figure 73 – Loads or prescribed displacements.

The constitutive model used for the simulation of the concrete behaviour was the NLMM104 and Figure 74 shows how this model is chosen in the software (command: **Data** → **Materials** → **Continuous Materials** → **NLMM104 Concrete** → **Input the Generic Properties** → **Input the Fracture Mode I Properties** → **Selection of the material** → **Assign**).

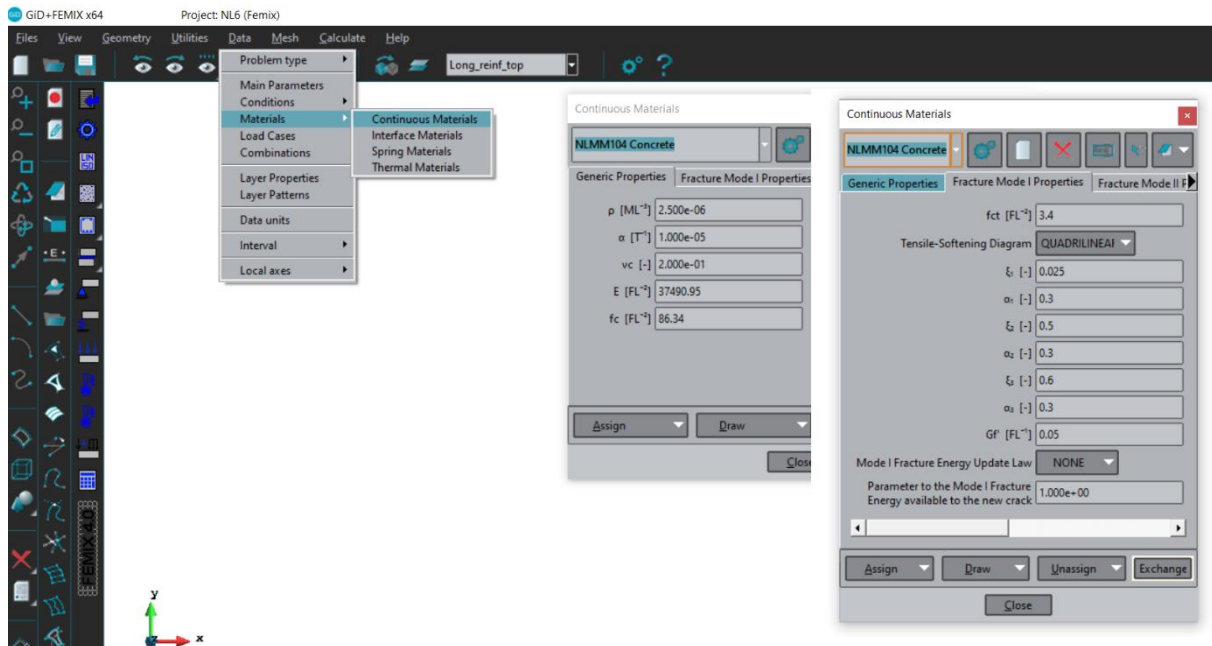


Figure 74 – Concrete properties used in the simulation of the A\_6\_0 shallow beams series.

The constitutive model used for the simulation of the steel behaviour was the NLMM201 and Figure 75 shows how this model is chosen in the software (command: **Data** → **Materials** → **Continuous Materials** → **NLMM201 Steel** → **Input Properties** → **Selection of the material** → **Assign**).

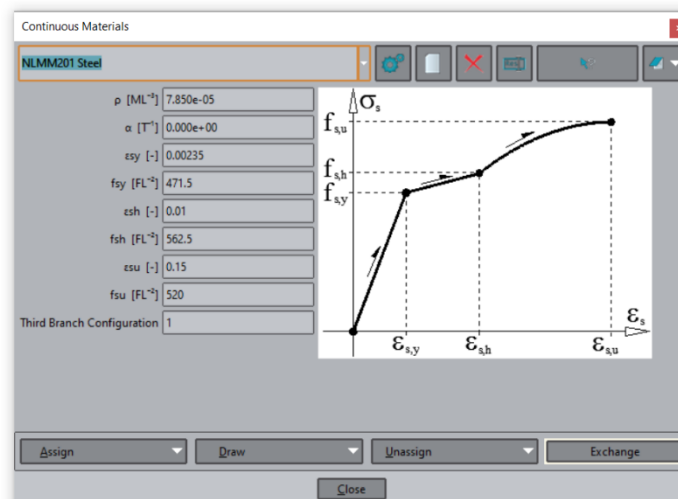


Figure 75 – Steel properties used in the simulation of the A\_6\_0 shallow beams series.

A crucial aspect of a numerical simulation is the verification of the constitutive model used to define the materials (command: **Data** → **Materials** → **Continuous Materials** → **Draw** → **Colours**), as shown in the example depicted in Figure 76.

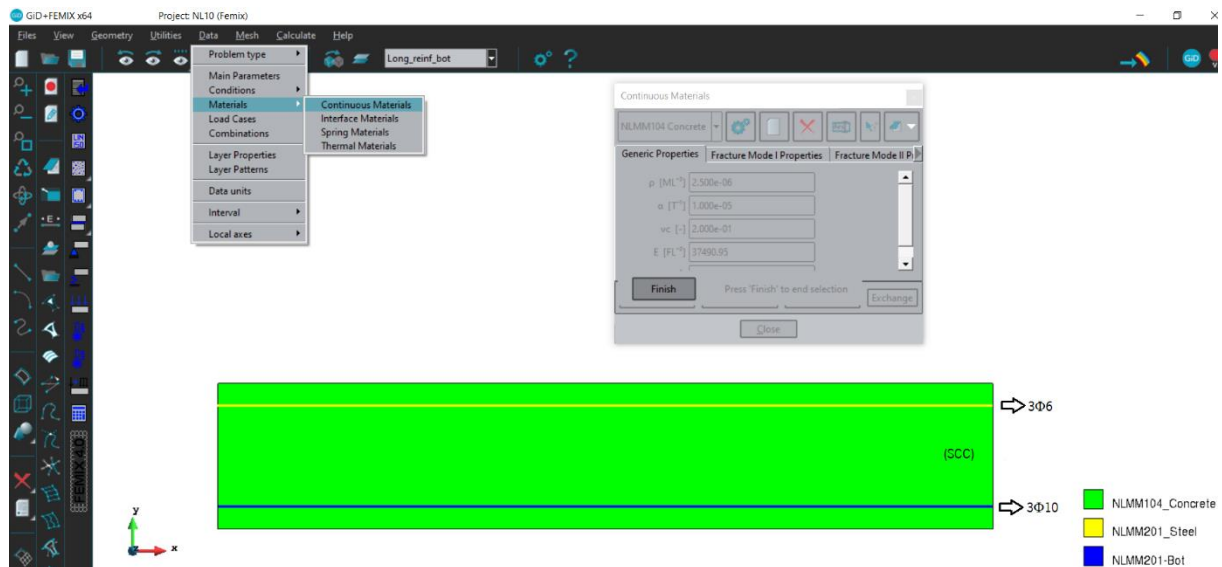


Figure 76 – Example of GID graphic visualization of the assigned materials constitutive models in the C\_10\_0 shallow beams series.

The final step before performing the numerical simulation was the definition of the load cases and the combinations that better suited the experimental program. To introduce the load cases is necessary to define the name of the load to be applied and indicate whether it is intended to apply the self-weight of the structure (command: **Data** → **Load Cases** → **Load Title** → **Accept**). For the introduction of the combinations is necessary to follow the command (**Data** → **Combinations** → **Combination Title** → **Number of Increment un the Combination** → **Number of Load Cases** → **Load Factor** → **Add** → **Accept**), see Figure 77. In all the numerical simulations the load was applied by direct displacement—control at the loaded point (Node number 653, degree of freedom Y) and the Newton-Raphson algorithm was used (command: **Data** → **Main Parameters** → **Nonlinear Analysis** → **Arc Length**), Figure 78.

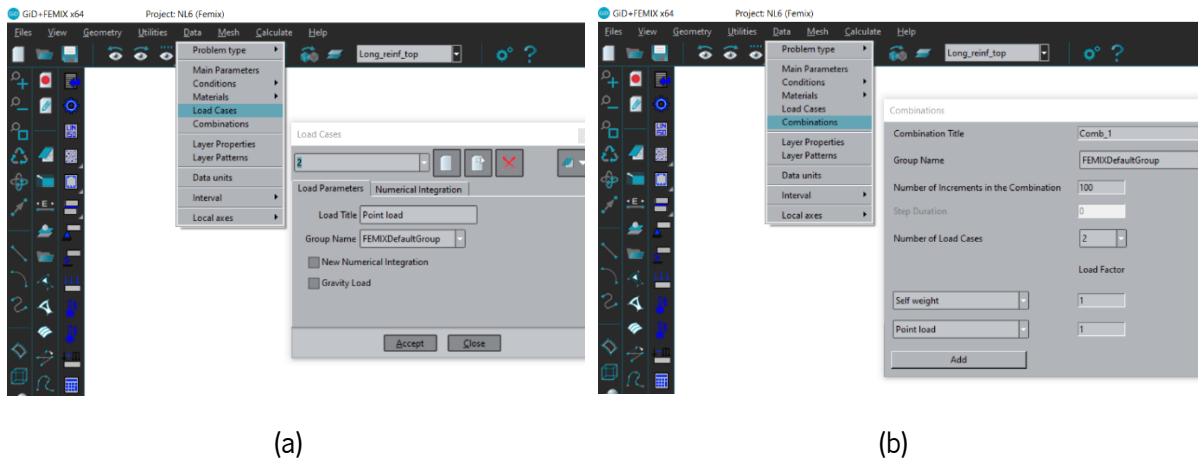


Figure 77 – Introduction of load cases and combinations to the numerical model: (a) Load Cases, (b) Combinations.

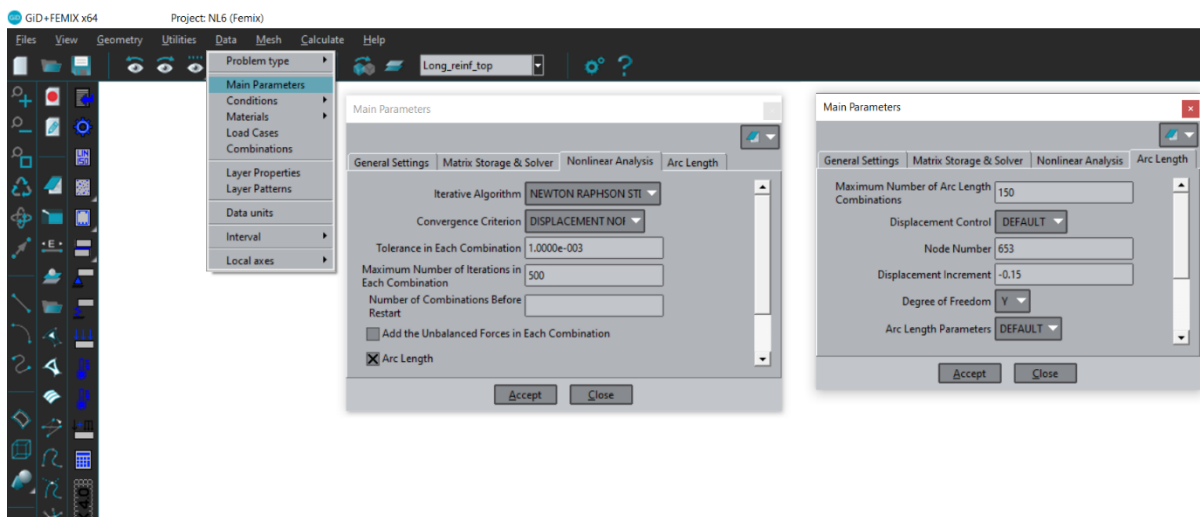


Figure 78 – Introduction of the Newton-Raphson method and Arc-length technique to the numerical model.

After going through all the steps described previously, it is possible to proceed to calculate the structure behaviour using the software FEMIX, Figure 79.

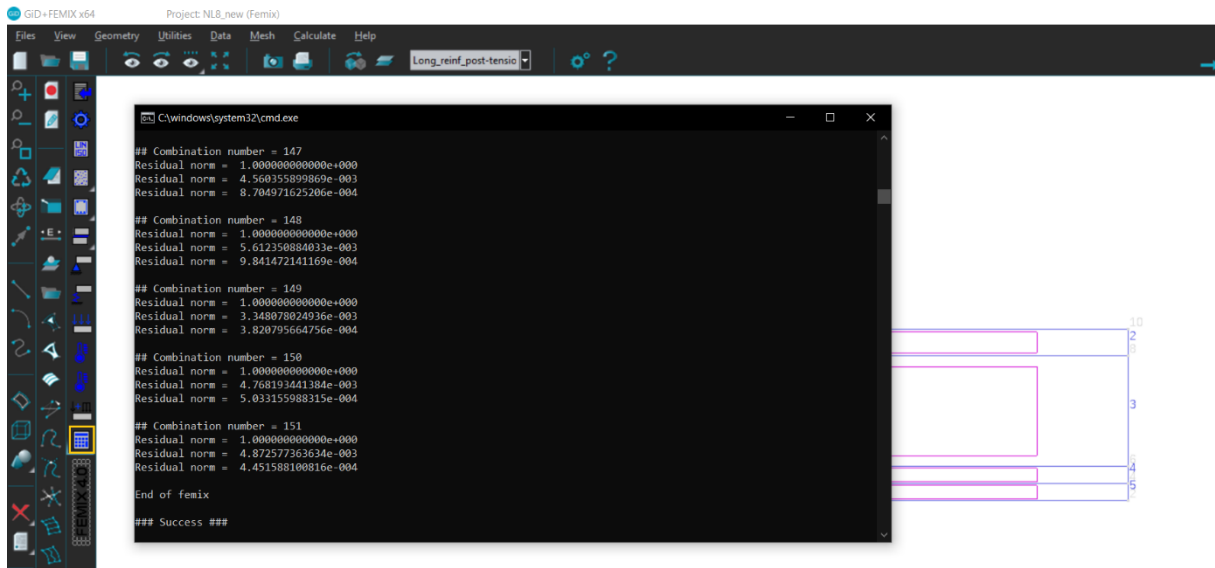


Figure 79 – Numerical model calculation process.

## APPENDIX B

### I-shaped cross-sectional beam design

#### Permanent Loads

I beam deadweight:

$$g_{k,beam} = 25 \text{ kN/m}^3 * A_{beam} = 3.03 \text{ kN/m} \quad (41)$$

Where  $A_{beam} = 0.12 \text{ m}^2$  is the area of the cross section of the studied I beam.

Office slab deadweight:

$$g_{k,slab} = 3 \text{ kN/m}^2 * L_{influence} = 18 \text{ kN/m} \quad (42)$$

Where  $L_{influence} = 6 \text{ m}$  is the loading influence width of the slab supported by the beam.

Slab covering deadweight:

$$g_{k,slabcov.} = 0.5 \text{ kN/m}^2 * L_{influence} = 3 \text{ kN/m} \quad (43)$$

#### Live loads

Office buildings live load:

$$q_k = 3 \text{ kN/m}^2 * L_{influence} = 18 \text{ kN/m} \quad (44)$$

Where  $L_{influence} = 6 \text{ m}$  is the loading influence width of the slab supported by the beam.





## Ultimate Limit States

In relation to the ultimate limit states (ULS) the characteristic load combination is given by Eq.(45).

$$P_{ULS,k} = 1.35 * \Sigma g_k + 1.5 * q_k \quad (45)$$

Then, assuming the previous values, the Eq.(45) leads to the uniformly distributed load in Eq.(46).

$$P_{ULS,k} = 1.35 * (3.03 + 18 + 3) + 1.5 * 18 = 59.44 \text{ kN/m} \quad (46)$$

To determine the maximum acting design bending moment at mid-span for both ultimate and serviceability limit states, Eq.(47) is used.

$$M_{ULS,k} = \frac{P_{ULS,k} * L_{beam}^2}{8} \quad (47)$$

Where  $L_{beam} = 12 \text{ m}$  is the loaded length of the beam.

Resulting a maximum acting design bending moment at mid-span of:

$$M_{ULS,k} = \frac{59.44 * 12^2}{8} = 1069.92 \text{ kN} * \text{m} \quad (48)$$

The frequent load combination is given by Eq.(49).

$$P_{ULS,fr} = 1.35 * \Sigma g_k + 1.5 * \psi_1 * q_k \quad (49)$$

$$P_{ULS,fr} = 1.35 * (3.03 + 18 + 3) + 1.5 * 0.5 * 18 = 45.94 \text{ kN/m} \quad (50)$$

$$M_{ULS,fr} = \frac{45.94 * 12^2}{8} = 826.92 \text{ kN} * \text{m} \quad (51)$$

The quasi-permanent load combination is given by Eq.(52).

$$P_{ULS,q} = 1.35 * \Sigma g_k + 1.5 * \psi_2 * q_k \quad (52)$$

$$P_{ULS,q} = 1.35 * (3.03 + 18 + 3) + 1.5 * 0.3 * 18 = 40.54 \text{ kN/m} \quad (53)$$

$$M_{ULS,q} = \frac{40.54 * 12^2}{8} = 729.73 \text{ kN * m} \quad (54)$$

### Serviceability Limit States

For the serviceability limit states (SLS) the characteristic load combination is given by Eq. (55).

$$P_{SLS,k} = 1.0 * \Sigma g_k + 1.0 * q_k \quad (55)$$

$$P_{SLS,k} = 1.0 * (3.03 + 18 + 3) + 1.0 * 18 = 42.03 \text{ kN/m} \quad (56)$$

$$M_{SLS,k} = \frac{42.03 * 12^2}{8} = 756.54 \text{ kN * m} \quad (57)$$

Finally, the quasi-permanent load combination is given by Eq.(58).

$$P_{SLS,q} = 1.0 * \Sigma g_k + 1.0 * \psi_2 * q_k \quad (58)$$

$$P_{SLS,q} = 1.0 * (3.03 + 18 + 3) + 1.0 * 0.3 * 18 = 29.43 \text{ kN/m} \quad (59)$$

$$M_{SLS,q} = \frac{40.54 * 12^2}{8} = 529.74 \text{ kN * m} \quad (60)$$